Creep and Corrosion Behavior of SiC Nanoparticles Dispersed Squeeze-cast Mg-5.0Al-2.0Ca-0.3Mn Alloy

Dissertation submitted in partial fulfilment

of the requirement of the degree of

Doctor of Philosophy

in

Metallurgical Engineering

by

Purnendu Nasker

(Roll Number: 18141005)

Under the supervision of

Dr. Ashok Kumar Mondal

Department of Metallurgical Engineering,
Indian Institute of Technology (BHU) Varanasi,
Varanasi - 221005, India.

February 2025

CERTIFICATE

It is certified that the work contained in the thesis titled "**Creep and Corrosion Behavior of SiC Nanoparticles Dispersed Squeeze-cast Mg-5.0Al-2.0Ca-0.3Mn Alloy**" by "**Purnendu Nasker**" has been carried out under my supervision and that this work has not been submitted elsewhere for a degree.

It is further certified that the student has fulfilled all the requirements of comprehensive, candidacy, and SOTA for the award of a Ph.D. degree.

Dr. Ashok Kumar Mondal
(Supervisor)
Associate Professor,
Department of Metallurgical Engineering,
Indian Institute of Technology (BHU) Varanasi,
Varanasi - 221005, India.

सह–आचार्य
Associate Professor
धातुकीय अभियांत्रिकी विभाग
Department of Metallurgical Engg.
भारतीय प्रौद्योगिकी संस्थान (काशी हिन्दु विश्वविद्यालय)
Indian Institute of Technology (Banaras Hindu University)
वाराणसी–२२१००५/Varanasi-221005

DECLARATION BY THE CANDIDATE

I, **Purnendu Nasker**, certify that the work embodied in this Ph.D. thesis is my own bonafide work carried out under the supervision of **Dr. Ashok Kumar Mondal** for a period from July 2018 to February 2025, at the Department of Metallurgical Engineering, Indian Institute of Technology (BHU) Varanasi, India. The matter embodied in this Ph.D. thesis has not been submitted for the award of any other degree/diploma. I declare that I have faithfully acknowledged and given credits to the research workers wherever their works have been cited in my work in this thesis. I further declare that I have not willfully copied any other's work, paragraphs, text, data, results, etc., reported in journals, books, magazines, reports, dissertations, thesis, etc., or available at websites and have not included them in this thesis and have not cited as my own work.

Date: February 2025

Place: Varanasi

Purnendu Nasker

Purnendu Nasker

CERTIFICATE BY THE SUPERVISOR

This is to certify that the above statement made by the candidate is correct to the best of my knowledge.

Dr. Ashok Kumar Mondal

(Supervisor)

Associate Professor,

Department of Metallurgical Engineering,

Indian Institute of Technology (BHU) Varanasi,

Varanasi - 221005, India.

सह–आचार्य
Associate Professor
धातुकीय अभियांत्रिकी विभाग
Department of Metallurgical Engg.
भारतीय प्रौद्योगिकी संस्थान (काशी हिन्दू विश्वविद्यालय)
Indian Institute of Technology (Banaras Hindu University)
वाराणसी-२२१००५/Varanasi-221005

Forwarded by:

Santhi Srinivas

Head of the Department,

Department of Metallurgical Engineering,

Indian Institute of Technology (BHU) Varanasi,

Varanasi - 221005, India.

विभागाध्यक्ष/HEAD
धातुकीय अभियांत्रिकी विभाग
Department of Metallurgical Engg.
भारतीय प्रौद्योगिकी संस्थान (काशी हिन्दू विश्वविद्यालय)
Indian Institute of Technology(Banaras Hindu University)
वाराणसी-221005/Varanasi-221005

COPYRIGHT TRANSFER CERTIFICATE

Title of the Thesis: "Creep and Corrosion Behavior of SiC Nanoparticles Dispersed Squeeze-cast Mg-5.0Al-2.0Ca-0.3Mn Alloy"

Name of the Student:

Purnendu Nasker.

Purnendu Nasker

(Roll No.: 18141005)

COPYRIGHT TRANSFER

The undersigned hereby assigns to the Indian Institute of Technology (BHU), Varanasi, all rights under copyright that may exist in and for the above thesis submitted for the award of the Doctor of Philosophy.

Date: February 2025

Place: Varanasi

Purnendu Nasker.

Purnendu Nasker

Note: However, the author may reproduce or authorize others to reproduce material extracted verbatim from the thesis or derivative of the thesis for the author's personal use, provided that the source and the Institute's copyright notice are indicated.

Acknowledgment

I would like to express my heartfelt gratitude to my supervisor, Dr. Ashok Kumar Mondal, for sharing his knowledge and expertise throughout this study. I am fortunate to have learned the fundamentals of Mechanical Metallurgy from him. His profound understanding of the subject and its practical applications has helped me develop an independent approach to grasping these concepts. Dr. Mondal's consistent encouragement to work diligently has incredibly benefited me. I am deeply grateful for his insightful suggestions, delivered in his unique style, which greatly contributed to improving my thesis. I will always admire his exemplary character and organized approach to work. It has been a valuable experience to work under his guidance.

I would like to thank the former Heads, Prof. N. K. Mukhopadhyay and Prof. S. Mohan, as well as the current Head, Prof. N. C. Santhi Srinivas of the Department of Metallurgical Engineering, IIT (BHU) Varanasi, for their kind supports and extending the departmental facilities to carry out the present work. I would also like to thank the RPEC members of my thesis, Prof. Mohd Zaheer Khan Yusufzai and Prof. Kausik Chattopadhyay, for their valuable suggestions during the thesis work. I would also like to extend my gratitude to Prof. Joysurya Basu for providing valuable input on the discussion of the TEM results throughout the thesis work. I am grateful to the other faculty members of the department for fostering such an excellent research environment. I extend my appreciation to the non-teaching staff of the department as well as CIF, IIT (BHU) Varanasi for their assistance in carrying out the experimental and official works.

I would like to thank the Science and Engineering Research Board (SERB), Department of Science and Technology (DST), New Delhi, India, and the Council of Scientific and Industrial Research (CSIR), New Delhi, India, for the financial support to carry out the present work. I also extend my gratitude to the Department of Metallurgical Engineering, PSG College of Technology, the Central Institute Facility, IIT Kanpur, Scanning Electron Microscopy Lab, IIT Kharagpur, Oriental Imaging Microscopy & Texture Lab, IIT Mumbai for extending their SEM, EBSD, and TEM facilities for microstructural characterization.

I thank my past and present labmates for their help and support during the thesis work. I thank Soham, Saptarshi, Saumya, Angkan, Bidipta, Aditi, Satyam, Urvashi, Deepak, Sujeet, Gaurav,

and Shradhha for their cheerful company. I would also like to thank my seniors, Dr. Jichil Majhi, Dr. Sourav Ganguly, Dr. Aman Kumar Lal Das, Dr. Avnish Singh, Dr. Roopchand Tandon, and Dr. Sandeep, for providing valuable inputs on the discussion of the TEM results and other unconditional support during the thesis work.

I express my sincere gratitude and indebtedness to my parents for their blessings, care, and support. I would also like to thank my wife and her parents, brother, and sisters for their constant encouragement and moral support.

Purnendu Nasker

Purnendu Nasker

Contents

List of Figures

List of Tables

List of Abbreviations

BF	:	**B**right **F**ield
CYS	:	**C**ompressive **Y**ield **S**trength
DF	:	**D**ark Fild
FWHM	:	**F**ull **W**idth **H**alf **M**axima
GB	:	**G**rain **B**oundary
GBMS	:	**G**rain **B**oundary **M**isorientation **S**train
GNP	:	**G**raphene **N**ano **P**articles
HAGB	:	**H**igh **A**ngle **G**rain **B**oundary
KAM	:	**K**ernel **A**verage **M**isorientation
LAGB	:	**L**ow **A**ngle **G**rain **B**oundary
NCs	:	**N**anocomposites
OCP	:	**O**pen **C**ircuit **P**otential
SHE	:	**S**train **H**ardening **E**xponent
SHR	:	**S**train **H**ardening **R**ate
TB	:	**T**win **B**oundary
TYS	:	**T**ensile **Y**ield **S**trength
UTS	:	**U**ltimate **T**ensile **S**trength
UCS	:	**U**ltimate **C**ompressive **S**trength
XRD	:	**X**-ray **D**iffraction

List of Symbols

T	:	Absolute temperature
σ	:	Applied stress
K	:	Boltzmann's constant
b	:	Burgers vector
Q	:	Creep activation energy
A	:	Diameter of the indenter
D_0	:	Coefficient of self-diffusion
%El	:	%Elongation
D	:	Grain size
p	:	Inverse grain size exponent
P_m	:	Mean pressure
$\dot{\epsilon}$	:	Steady-state creep rate
G	:	Shear modulus
n	:	Stress exponent
R	:	Universal gas constant
V_{imp}	:	Impression velocity
σ_{imp}	:	Stress in impression creep

Abstract

The influences of the SiC nanoparticles (SiC_{np}) dispersion on the microstructural modification, tensile, compression, creep, and corrosion behavior of the squeeze-cast Mg-5.0Al-2.0Ca-0.3Mn (AXM520) (wt.%) alloy have been investigated. The concentrations of the SiC_{np} are varied from 0.5 to 3.0 (wt.%), and the squeeze-cast nanocomposites (NCs) are abbreviated as NC0.5SiC, NC1.0SiC, NC2.0SiC and NC3.0SiC. A detailed microstructural characterization of the AXM520 alloy and NCs has been carried out. The as-cast microstructures of the AXM520 alloy and NCs consist of a primary solid solution (α-Mg), a eutectic of α-Mg and $(Mg,Al)_2Ca$ (C36) phases, and an Al_8Mn_5 phase. Additionally, the SiC phase is also present in the NCs. The continuous network of the C36 phase is fragmented and becomes discontinuous as the content of the SiC_{np} increases in the NCs.

The ambient temperature tensile and compressive properties of the AXM520 alloy and NCs have been evaluated. All the NCs exhibit superior tensile and compressive properties to the AXM520 alloy. The NC2.0SiC exhibits the best tensile properties among the NCs employed. The YS of the NCs improves with the increase in the SiC_{np} content up to 3.0 (wt.%). The UTS and %El of the NCs increase up to 2.0SiC_{np} (wt.%), and beyond that, the same declines owing to the agglomeration of the nanoparticles. The discontinuous network of the C36 phase in the NCs inhibits crack propagation, leading to their improved %El. All the NCs exhibit a higher strain-hardening exponent (n) and strain-hardening rate (SHR) compared to the AXM520 alloy. The superior 'n' and SHR exhibited by the NCs are attributed to the grain refinement and dislocations generation. The strengthening from CTE mismatch contributes the most to the overall strengthening of the NCs. The 'Zhang and Chen' model is modified by introducing an agglomeration factor, and the predicted YS of the NCs matches pretty well with the experimentally obtained values.

The creep behavior of the AXM520 alloy and NCs has been examined using impression creep tests in the temperature range from 448 K to 523 K and stress range from 390 to 490 MPa. All the NCs reveal improved creep performance compared to the AXM520 alloy. The creep rate of the NCs decreases with the increase in the SiC_{np} content. The NC2.0SiC exhibits an improvement in creep resistance by 73.2% compared to the alloy. However, the creep resistance deteriorates since the amount of the nanoparticles is further increased in the

NC3.0SiC, leading to agglomeration. The stress exponents vary from 5.0 to 6.7, and activation energies vary from 89.8 to 101.8 kJ/mol, implying that the creep in the materials is controlled by the climb of dislocation assisted by the pipe diffusion. The pile-ups of dislocations take place around the C36 phase and near the SiC_{np}. The additional strengthening owing to the presence of the SiC_{np} in the NCs is responsible for their improved creep performance compared to the AXM520 alloy.

The corrosion behavior of the AXM520 alloy and NCs has been investigated in a 3.5 (wt.%) NaCl solution at a pH of 7.0. The corrosion resistance of the NCs measured in the hydrogen evolution test is superior to the AXM520 alloy, and the improvement is 91.1% in the NC3.0SiC. The polarization resistance determined from the EIS increases with the increase in the SiC_{np} content in the NCs. The potentiodynamic polarization scans further confirm the superior corrosion resistance of the NCs to the AXM520 alloy. Among the fabricated NCs, NC3.0SiC exhibits the highest corrosion resistance, and it is 91.3% lower in comparison to the AXM520 alloy. The corrosion products predominantly consist of $Mg(OH)_2$. The addition of SiC_{np} reduces the formation of $Mg(OH)_2$ and increases the content of the $Al(OH)_3$ in the NCs, leading to the higher stability of the corroded film formed on them. The α-Mg phase is severely damaged owing to the galvanic corrosion between the α-Mg and C36 phases. However, the same is reduced due to a decrease in the volta potential between α-Mg and C36 phases in the NCs, resulting in their superior corrosion resistance.

The squeeze-cast AXM520 alloy and NCs are further subjected to age-hardening. The alloy and NCs are homogenized at 773 K and artificially aged at 523 K. The aged alloy is designated as AXM520HT, and the nanocomposites containing 1.0 and 2.0 (wt.%) of SiC_{np} are designated as NC1.0SiCHT and NC2.0SiCHT, respectively. The microstructural evolution and creep characteristics of the squeeze-cast age-hardened alloy and NCs have been investigated. The age-hardened alloy and NCs contain primary α-Mg grains, $(Mg, Al)_2Ca$ (C36), Al_2Ca (C15), and Al_8Mn_5 phases. The SiC phase is additionally identified in the NCs. The NCs reveal superior creep resistance compared to AXM520HT, and it is the best in the NC2.0SiCHT. The creep resistance of the NC2.0SiCHT surpasses AXM520HT by 76%. Dislocation climb, facilitated by pipe diffusion, emerges as the mechanism governing creep deformation in the alloy and NCs. The creep deformation mechanism maps for the Mg-Al-Ca-based alloys and NCs are successfully constructed. The microstructural observation of the creep-tested specimens under the indenter concludes that the C36 phase is utterly broken in the

AXM520HT, whereas the same remains intact in the NC2.0SiCHT. The percentage of twins in the creep-tested specimen of NC2.0SiCHT is lower than in the AXM520HT alloy. Two different types of twins, i.e., extension twin $\{10\bar{1}2\}<10\bar{1}1>$, and double twin $\{10\bar{1}1\}$-$\{10\bar{1}2\}$ are observed in the NCs. The density of the <c> type dislocations is much higher than that of the <a> type dislocations in the NCs. The presence of SiC nanoparticles impedes the dislocation motion. The significant improvement in creep resistance of all the NCs over the AXM520HT alloy is attributed to the age-hardening as well as dispersion strengthening from the presence of the SiC nanoparticles.

To conclude, the tensile, compression, creep, and corrosion behavior of the squeeze-cast NC0.5SiC, NC1.0SiC, NC2.0SiC, and NC3.0SiC are superior to that of the AXM520 alloy. Thus, the use of NCs is beneficial over the AXM520 alloy. Among the as-cast NCs, NC2.0SiC is the best, considering the mechanical properties and corrosion behavior. In addition, the creep behavior of the age-hardened NC1.0SiCHT and NC2.0SiCHT is superior to that of the AXM520HT alloy. Among the aged alloy and NCs, the NC2.0SiCHT is the best considering the creep behavior.

Keywords: Magnesium alloy; Nanocomposite; Squeeze-cast; Microstructure; Creep; Corrosion

Chapter 1

Introduction

1.1 Introduction

The high specific strength and dimensional stability of magnesium (Mg) alloys make them an excellent choice for developing lightweight products for the automotive. It is foreseen that the potential growth of Mg alloys' application is driven by their use in automotive powertrain parts that experience temperatures of 423 to 573 K [1]. The Mg alloys suitable for such an application should exhibit good creep resistance. The magnesium-aluminium alloys are suitable for applications in the interior parts of automobiles that do not involve elevated temperatures. Unfortunately, these alloys did not find applications in the powertrain components since their creep performance above 403 K is not satisfactory [1,2]. The intermetallic phase, namely β-$Mg_{17}Al_{12}$ (M. P. 700 K), in Mg-Al alloys readily softens at above 403 K [1,2]. Hence, the enhancement of the creep performance of the Mg-Al alloy is possible by adding secondary elements which do not constitute the β-$Mg_{17}Al_{12}$ phase. Several studies have been conducted to manufacture Mg-Al alloys having superior creep resistance with the addition of Ca, Sr, and RE [3,4]. Yang et al. [5] concluded that the addition of Al above 1.0 (wt.%) in the Mg-2.85Nd-0.92Gd-0.41Zr-0.29Zn alloy deteriorated its creep property owing to the segregation of the Al_2RE phase. Bai et al. [6] developed a new RE-based alloy, Mg-6.35Y-3.00Zn-0.73Al, that exhibited superior creep properties to the AE44 alloy. Yang et al. [7] reported that the Mg-8.0Al-1.0Nd-1.0Gd alloy in heat-treated conditions exhibited superior creep resistance compared to the as-cast alloy owing to the discontinuous precipitate of the β-$Mg_{17}Al_{12}$ phase. Zhang et al. [8] showed that the addition of 1.0 (wt.%) RE in the Mg-9.0Al-0.3Ca-0.2Mn alloy significantly improved its creep resistance by suppressing the formation of the β-$Mg_{17}Al_{12}$ phase and promoting the formation of thermally stable intermetallic $Mg_{12}RE$ and Al_3RE phases. Thus, the RE-containing Mg alloys are promising for elevated temperature application; unfortunately, these alloys are not economical. On the contrary, Ca is comparatively more economical and less dense (i.e., 1.54 g/cm^3) than the other elements. It also increases the oxidation resistance and improves the creep property of the Mg-Al alloys [9,10]. Chen et al. [11] investigated the creep behavior of the Mg-Al alloys with the addition of Zn, Sn, and Ca. They concluded that among the elements, Ca was more effective in improving its creep resistance. Li et al. [12] observed grain refinement in the Mg-Al alloy with the incorporation of Ca. The incorporation of Ca to Mg-Al encouraged the constitution of Mg_2Ca (C14), Al_2Ca

(C15), and $(Mg,Al)_2Ca$ (C36) intermetallic phases that are thermally stable [13,14]. The work by Ninomiya et al. mentioned that only the Al_2Ca phase exists when the Ca/Al is less than 0.8, while for ratios greater than 0.8, both the Al_2Ca and Mg_2Ca phase exist simultaneously [15]. Suzuki et al. [16] reported that with the decrease in Ca/Al ratio, the dendritic eutectic structure in Mg-Al-Ca (AX) alloy contains more β-$Mg_{17}Al_{12}$ phase. Zhang et al. [17] observed the presence of phase changes in the sequence of Mg_2Ca, $(Mg,Al)_2Ca$, and Al_2Ca when the Ca to Al ratio reduced to 0.4 from 1.0. However, along with microstructure, the creep property of the AX alloys was highly influenced by the Ca/Al ratio. Nakaura et al. [18] observed that the minimum creep rate of the AX alloys decreased as the Ca/Al ratio increased to 0.3. The AXJ alloys with (Ca+Sr)/Al ratios of 0.40 and 0.33 were better for creep over the alloy containing (Ca+Sr)/Al ratio of 0.4 [19]. The enhanced creep resistance of the AJC511 (0.40) and AJC611 (0.33) alloys was accredited to the higher thermal stability of the Al_2Ca phase (M. P. 1352 K) present in these alloys than the Mg_2Ca (M. P. 988 K) phase present in the AJC411 (0.5) alloy. Itoh et al. examined the influence of Ca in Mg-Al-Mn (AM) alloy, and they observed the positive dependency of creep rate on Ca content [20]. Terada et al. [21] showed that the AX alloy with 1.72 (wt.%) Ca (Ca/Al=0.34) was better for creep resistance than the alloys containing lower wt.% of Ca. Thus, a summary of the literature review on the creep behavior concludes that Mg-Al-Ca alloys containing Ca/Al of 0.4 exhibited the best creep resistance. Accordingly, the Mg-5.0Al-2.0Ca alloy satisfying Ca/Al = 0.4 was considered for the present investigation.

In addition, the incorporation of Mn significantly improved the creep performance of Mg alloys [22-25]. Homma et al. [22] concluded that the minimum creep rate of AX22 alloy is decreased by one-tenth due to the addition of 0.3 (wt.%) Mn. Samimi et al. [23] assessed creep resistance of 0.3, 0.5, and 0.8 (wt.%) Mn added Mg-5.0Al-1.5Ca alloy. They identified that the creep property of the alloy increased up to 0.5 (wt.%) Mn, while further Mn incorporation deteriorated the creep property. Zhu et al. [24] confirmed that the creep performance of Mg-Al-RE alloy does not change significantly beyond 0.3 (wt.%) Mn. Lamm et al. [25] observed that 0.3 (wt.%) Mn addition stabilized the Ca clusters in Mg-Al-Ca-Mn (AXM) alloys, enhancing their creep resistance. Celikin et al. [26] reported improved creep performance of Mg-1.5 (wt.%) Mn alloy compared to pure Mg, resulting from the dynamic precipitation of α-Mn during creep. Thus, Mg-5.0Al-2.0Ca alloy with 0.3Mn addition (wt.%), i.e., Mg-5.0Al-2.0Ca-0.3Mn (AXM520) alloy, is expected to exhibit good creep resistance.

However, the application of AXM520 alloy might be restricted to 473 K. Ferkel and Mordike [27] reported that the dispersion of 3.0 vol.% SiC nanoparticles improved the creep response of pure Mg. The improved creep property of AS41 with 2.0 and 5.0 (wt.%) Al_2O_3 nanoparticles was reported by Kumar and Chaudhuri [28]. Katsarou et al. too reported a positive effect of 1.0 (wt.%) AIN addition on the creep response of Electron21 alloy [29]. Ganguly and Mondal [30] reported the dual advantage of alloying and SiC nanoparticles dispersion on the creep behavior of AZ91 alloy. Yang et al. [31,32] showed that better dispersion and increased amount of AIN and/or Al nanoparticles additions provided better creep response in Electron21 alloy. In a similar work, Zhou et al. [33] showed that the addition of 1.0 (wt.%) SiC nanoparticles addition decreased the creep rate of AS91 alloy by one order. Ganguly et al. [34] showed that the impression creep response of AZ91+0.6Sb was improved after the addition of 2.0SiC (wt.%). Thus, the dispersion of ceramic nanoparticles will bring plausible alteration in the microstructure and improve the creep resistance of the AXM520 alloy further, which might make it suitable for application beyond 473 K. Accordingly, the microstructural modification and creep behavior of Mg-5.0Al-2.0Ca-0.3Mn (AXM520) alloy with SiC nanoparticles (SiC_{np}) dispersion have been investigated.

The Mg-Al-Ca-Mn (AXM) alloy exhibits unsatisfactory ambient temperature strength, restricting its widespread application. Further, the tensile properties of the as-cast AXM-based alloys deteriorated, and the nature of failure became more brittle as the value of Ca/Al in the alloy increased [35]. The Ca-rich secondary phase acted as a crack initiation point leading to fracture. However, adding nanoparticles to pure Mg and Mg-based alloys significantly improved their tensile and compressive properties [36], which is beneficial. Therefore, an attempt has been made to improve the ambient temperature strength along with the ductility of the squeeze-cast AXM520 alloy with the addition of SiC_{np}. Thus, the ambient temperature tensile and compressive properties of the squeeze-cast AXM520 alloy and its nanocomposites are also investigated.

The high corrosion rates of Mg alloys limit their potential for widespread applications. The presence of the secondary phase β-$Mg_{17}Al_{12}$ influenced the galvanic corrosion of the Mg-Al-based alloys and deteriorated their corrosion resistance [37,38]. The Mg alloys reinforced with microparticles exhibited more detrimental corrosion properties than the parent unreinforced alloy [39-41]. On the contrary, recent studies suggested that adding nanoparticles might significantly protect the Mg-based alloys from corrosion [42-45]. The presence of Ca and Mn

is expected to improve the corrosion behavior of the Mg-Al-based alloys [46,47]. However, the influence of the SiC_{np} addition on the corrosion response of the AXM520 alloy is unclear. Thus, the ambient temperature corrosion behavior of the newly developed squeeze-cast AXM520 alloy and its nanocomposites is also investigated.

Several studies were conducted on the creep characteristics of dispersion-strengthened pure Mg and Mg alloys [48]. The summary of the literature review concludes that the dispersion of nanoparticles in Mg alloys imparts significant enhancement in creep properties. Further, age-hardening improves the strength of Mg alloys [49]. Unfortunately, to the best of the authors' knowledge, the creep behavior of age-hardened and dispersion-strengthened Mg alloys has not been explored yet. Therefore, the microstructural alteration and creep characteristics of the squeeze-cast age-hardened AXM520 alloy with SiC nanoparticles additions are also investigated. A correlation of the creep responses of age-hardened AXM520 alloy and its nanocomposites with their initial and creep-deformed microstructures has also been established. For the first time, deformation mechanism maps for Mg-Al-Ca alloys and their nanocomposites are constructed.

Thus, the present thesis aims to explore the microstructural alteration, creep characteristics, and corrosion behavior of the squeeze-cast AXM520 alloy with SiC nanoparticles additions. The microstructural alteration and creep characteristics of the squeeze-cast age-hardened AXM520 alloy with SiC nanoparticles additions are also explored. A correlation of the creep responses of age-hardened AXM520 alloy and its nanocomposites with their initial and creep-deformed microstructures has also been established.

1.2 Objective of the present thesis

The objectives of the present thesis are to investigate the microstructure, creep characteristics, and corrosion behavior of the squeeze-cast AXM520 alloy with SiC nanoparticles additions. Further, the microstructural alteration and creep characteristics of the squeeze-cast age-hardened AXM520 alloy with SiC nanoparticles additions are also explored. The salient objectives of the present thesis are as follows.

1. The fabrication of the AXM520 alloy and its nanocomposites (NCs) with SiC nanoparticles additions by squeeze-casting.

2. A detailed microstructural characterization of the fabricated AXM520 alloy and its nanocomposites.
3. The evaluation of the ambient temperature tensile and compressive properties of the AXM520 alloy and its nanocomposites.
4. The evaluation of the creep behavior of the squeeze-cast AXM520 alloy and its nanocomposites.
5. The evaluation of the corrosion behavior of the AXM520 and its nanocomposites.
6. To explore the microstructural alteration and creep characteristics of the squeeze-cast age-hardened AXM520 alloy and its nanocomposites.

1.3 Organization of the thesis

The present thesis consists of nine chapters, and the content of each chapter is as follows.

- **Chapter 1** consists of a brief introduction to the present investigation, discusses the objective of the present thesis, and provides the organization of the thesis.
- **Chapter 2** discusses the detailed literature review relevant to the present work and summarises the motivation for the current research.
- **Chapter 3** describes the details of the materials and experimental procedure followed.
- **Chapter 4** provides the detailed microstructural characterization of the squeeze-cast AXM520 alloy and its nanocomposites.
- **Chapter 5** investigated the tensile and compressive behavior of the AXM520 alloy and its nanocomposites. Additionally, the strengthening mechanisms involved in the nanocomposites are addressed.
- **Chapter 6** evaluates the creep response of the squeeze-cast AXM520 alloy and its nanocomposites.
- **Chapter 7** explored the corrosion response of the squeeze-cast AXM520 alloy and its nanocomposites.
- **Chapter 8** discusses the microstructure and creep response of the squeeze-cast aged-hardened AXM520 alloy and its nanocomposites.
- **Chapter 9** summarizes the major conclusions drawn from the present investigation and discusses the scope for future work.

The references cited in the entire thesis are enlisted in the reference section.

Chapter 2

Literature Review

This chapter provides a brief overview of the literature related to the present investigation. A brief introduction to Mg and its alloys is provided at the beginning of this chapter. Then, the theories of creep, tensile, compression, and corrosion were presented. A detailed review of the current research on the creep, tensile, compression, and corrosion behavior of Mg and Mg alloy-based nanocomposites has been introduced next to the respective theory. Finally, the motivation behind the present work, as concluded from the literature review, is provided at the end of this chapter.

2.1 Designation of magnesium (Mg) alloys

The nomenclature of magnesium (Mg) alloys adheres to a standardized alpha-numeric system, wherein each alloy designation consists of alphabetical prefixes denoting major alloying constituents, followed by numerical suffixes indicating their respective weight percentages. The Al and Zn alloyed Mg alloys are designated as the AZ series. Depending on the contents of Al and Zn (wt.%), the AZ alloys are expressed as AZ91, AZ61, and AZ31, where the Al content is 9.0, 6.0, and 3.0 (wt.%), respectively, and the Zn content is 1.0 (wt.%) for each alloy. The Al and Mn alloyed Mg alloys are known as the AM series. In this series, the popular alloys are AM50 and AM60, where the Al content is 5.0 and 6.0 (wt.%), respectively, and the Mn content is less than 0.5 (wt.%) in both alloys. Thus, a zero is used for the element if its content is ≤0.5 (wt.%) in the alloy. The Mg-Al-Ca-based alloys are designated as AX series. In the present thesis, a Mg alloy consisting of 5.0Al, 2.0Ca, and 0.3Mn (wt.%) is fabricated. Therefore, according to the standard notation, the alloy is designated as AXM520. The standard alphabetic symbols used for the various alloying elements in Mg are shown in Table 2.1 [50].

2.2 Role of selected alloying elements in Mg alloys

Aluminium (Al): Al is one of the common alloying elements added to pure Mg. Al addition enhances the room temperature strength of pure Mg by solid solution strengthening. The hardness of pure Mg also increases owing to the addition of Al. The alloying of Al also improves the castability of pure Mg [50].

Table 2.1 Abbreviations used for the alloying elements added to Mg [50].

Element	Symbol	Element	Symbol	Element	Symbol
Aluminium	A	Lithium	L	Tin	T
Bismuth	B	Manganese	M	Yttrium	W
Copper	C	Nickel	N	Calcium	X
Cadmium	D	Lead	P	Antimony	Y
Rare Earths	E	Silver	Q	Zinc	Z
Iron	F	Chromium	R		
Strontium	J	Silicon	S		

Calcium (Ca): The addition of Ca significantly improves the creep and corrosion resistance of pure Mg. Adding Ca also enhances the oxidation resistance of Mg melt during casting [51,52].

Manganese (Mn): Mn improves the corrosion resistance of Mg alloys by eliminating Fe impurities present in the Mg alloys. However, the limited solid solubility of Mn in Mg limits its concentration in Mg [50].

2.3 Mg-Al-Ca alloys

The Mg-Al-Ca (AX) alloys are known for their superior creep and corrosion resistance among the Mg-Al-based alloys. The Ca/Al ratio plays a crucial role in the microstructural, mechanical, and corrosion behavior of the AX alloys. Linag et al. [53] mentioned that the formation of the β-$Mg_{17}Al_{12}$ phase was suppressed when Ca content was above 1.0 (wt.%) in the AM50 alloy. The Ca/Al ratio strongly governs the formation of the Ca-rich intermetallic phases in the AX alloys. The presence of the β-$Mg_{17}Al_{12}$ phase was reported when the Ca content was lower than 0.8 (wt.%) in the AM50 alloy. In addition to the β-$Mg_{17}Al_{12}$ phase, the Al_2Ca phase was detected in several AX-based alloys. Suzuki et al. [54] studied the solidification pathways of the AX alloys and mentioned that the formation of the Al_2Ca phase took place by a solid-state diffusion of the $(Mg,Al)_2Ca$ phase. The Ca addition influences the formation of three Ca-rich intermetallics having AB_2 stoichiometry which is known as the Laves phase. These

intermetallics are Mg_2Ca (HCP, Pearson symbol hP12, space group P63/mmc (194) and Strukturbericht notation $MgZn_2$ (C14)), $(Mg,Al)_2Ca$ (Double hexagonal crystal structure, Pearson symbol hP24, space group P63/mmc (194) and Strukturbericht notation $MgNi_2$ (C36)), and Al_2Ca (Cubic crystal structure, Pearson symbol cF24, space group $Fd\bar{3}m$ (227), and Strukturbericht notation $MgCu_2$ (C15)). The schematics of the various laves phases form in the Mg-Al-Ca alloys is shown in Figure 2.1 [55].

The C14 phase is more brittle than the C36 and C15 phases. The AX alloys undergo failure in a more brittle manner as the concentration of C14 phase increased in it [56]. The Mg-based micropillar studies of the laves phases showed that the co-deformation of the C36 phase with the α-Mg phase was noticeable rather than the C15 phase [57]. However, both these phases exhibited remarkable strengthening effects on the α-Mg phase and improved the strength of the alloy. The formation sequence of the laves phases strongly depends on the Ca content and Ca/Al ratio in the AX alloys. Zubair et al. [58] concluded that the C36 phase in the AX alloy remains stable up to 773 K. Among the laves phases form in the AX alloys, the C15 phase has the highest thermal stability owing to its higher melting point (1352 K). Therefore, the presence of the C36 and C15 phases in the AX alloys strongly influences their high-temperature properties. As the concentration of Ca decreases in AX alloys, the phases appear in the sequence of Mg_2Ca, $(Mg,Al)_2Ca$, Al_2Ca, and β-$Mg_{17}Al_{12}$. The increased concentration of Ca greatly improves the morphology of the precipitate phase, as shown in Figure 2.2 [59]. The magnified micrographs exhibit that the interlamellar spacing between the secondary phase decreases as the Al/Ca ratio increases in the AXM alloy. This also improved the strength of the alloy. However, the increased (wt.%) of Ca deteriorates the ductility of the AX alloys, which is attributed to the mechanical property mismatch between the α-Mg and laves phases [35]. The laves phases are thermally stable, resulting in superior creep resistance of the AXM alloys. In heat-treated AX alloys, the C36 phase transforms into the C15 phase by a solid-state diffusion process, which helps to improve the creep resistance of the AX alloys [54,60]. The C15 phase exhibits needle-like morphology following heat-treatment of AX-based alloys, as shown in Figure 2.3 [60]. Later studies identified them as semi-coherent precipitates of the C15 phase or G.P zones [61]. The alloying of Mn to AX alloys forms the Al_8Mn_5 phase. Mn segregates around the C15 G.P. zones and stabilizes them at high temperature. Thus, adding Mn improves the creep resistance of Mg-Al alloys [22]. However, Mn content should not exceed 0.5 (wt.%), which deteriorates the creep property of the alloy owing to increased

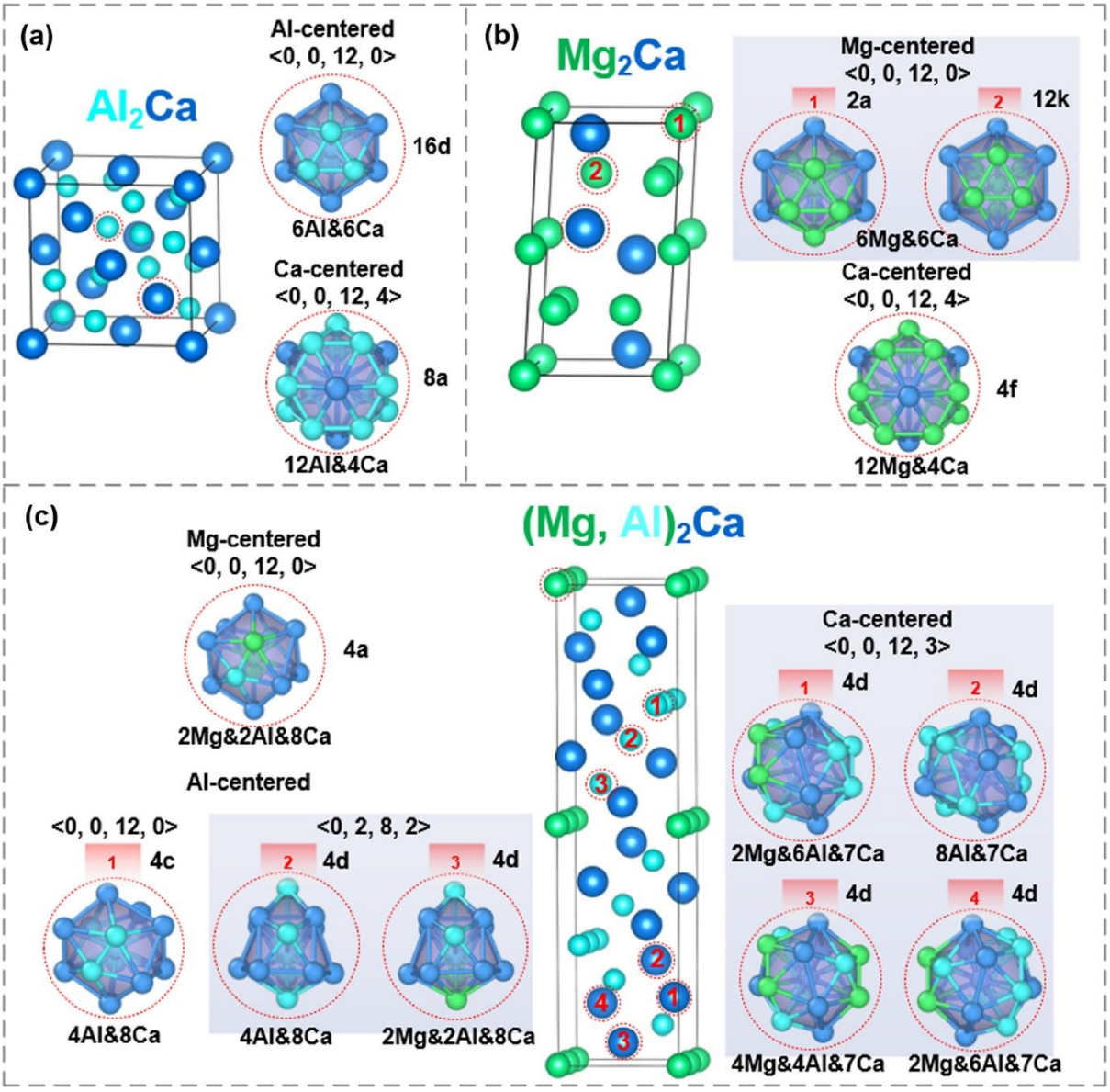

Figure 2.1 Illustration of coordination polyhedras centered by atoms at non-equivalent occupation sites in crystalline phases, including (a) C15-Al_2Ca, (b) C14-Mg_2Ca, and (c) C36-$(Mg,Al)_2Ca$. The number and type of constituent atoms in each coordination polyhedras are also shown. Wyckoff positions are shown with polyhedra. The light green, cyan, and blue spheres stand for Mg, Al, and Ca atoms, respectively [55]

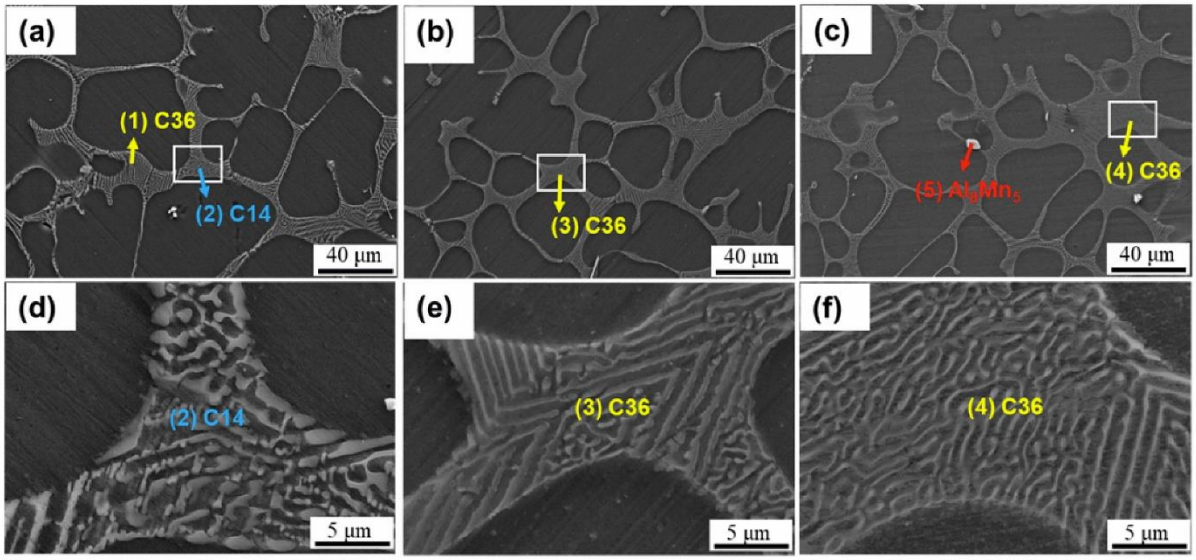

Figure 2.2 SEM micrographs of the as-cast Mg-Al-Ca-Mn alloys: (a, d) AXM530; (b, e) AXM630; (c, f) AXM730 [59].

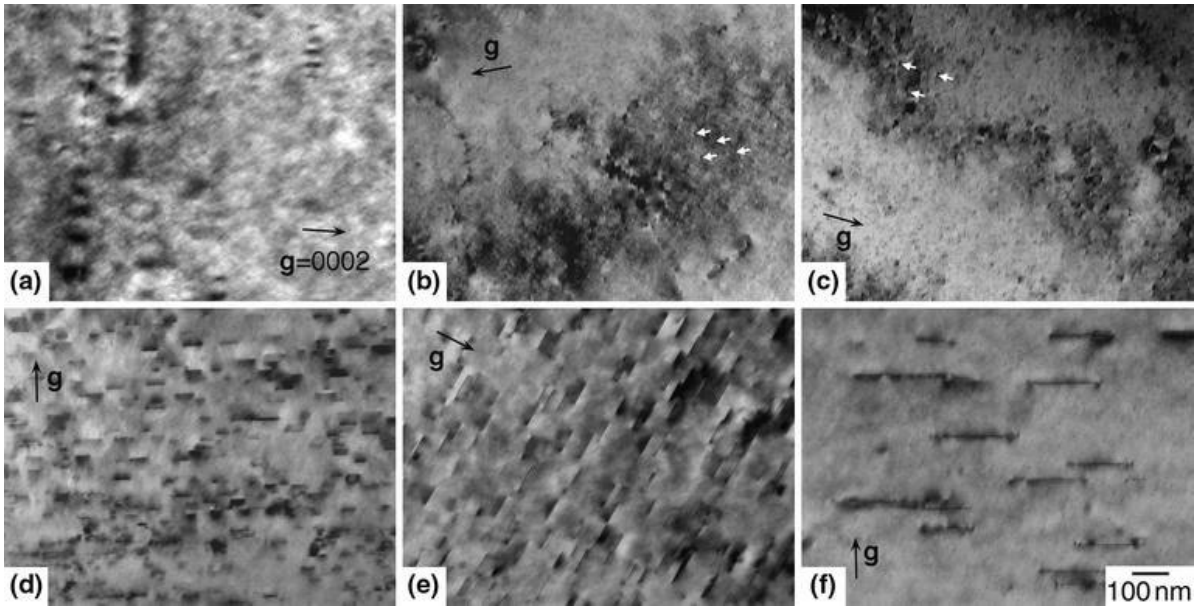

Figure 2.3 Precipitation of Al_2Ca phase in the die-cast AXJ530 alloy aged at 573 K. TEM bright-field images of the specimens aged for (a)10 s, (b) 30 s, (c) 100 s, (d) 600 s, (e) 3.6 ks and (f) 36 ks. These images were taken with B = $11\bar{2}0$ α, and **g**= 0002α. Precipitates are marked with arrows in (b) and (c) [60].

stacking fault energy. Zuo et al. [62] observed the Al_2Ca phase with Al_8Mn_5 precipitates following solutionizing and artificial aging of AXM alloy at 773 and 473 K, respectively.

2.4 Creep

Creep is a time-dependent plastic deformation of a material that is subjected to constant stress and temperature. The flow stress of a material is a function of stress and temperature. Therefore, if the test or application temperature is above absolute zero, a material undergoes deformation by the influence of both stress and temperature. However, when the test temperature is close to absolute zero, for a given stress, the deformation rate will be significantly lower because of the lower contribution from the thermal component. Thermal energy alone cannot move long segments of dislocation owing to its random nature, which can only vibrate local atoms. Thus, a small dislocation segment undergoes a climb operation using thermal energy to overcome the barrier experienced during dislocation motion. Figure 2.4(a) exhibits a schematic of the energy states of such a dislocation segment, which needs an activation energy of q to overcome the energy state 'B' while moving from 'A' to 'C' or vice-versa [63].

In order to understand the creep behavior of the material in a conventional creep test, the material is loaded uniaxially at constant stress and temperature. The strain plot of the test material as a function of time is then recorded, as shown in Figure 2.4(b). The strain rate (creep rate) plot as a function of total strain corresponding to Figure 2.4(b) is shown in Figure 2.4(c) [64]. Figure 2.4(b and c) exhibits three distinct regions of creep curve. The primary stage, or strain hardening stage, is where the strain hardening rate dominates the recovery stage, resulting in a fall in strain rate with time. In the secondary stage, the recovery rate balances the strain hardening rate, and a steady-state strain rate is attained. The steady-state creep rate has significant importance in engineering applications. The designed component should elapse the entire service period in the secondary region, allowing smooth functioning of the component.

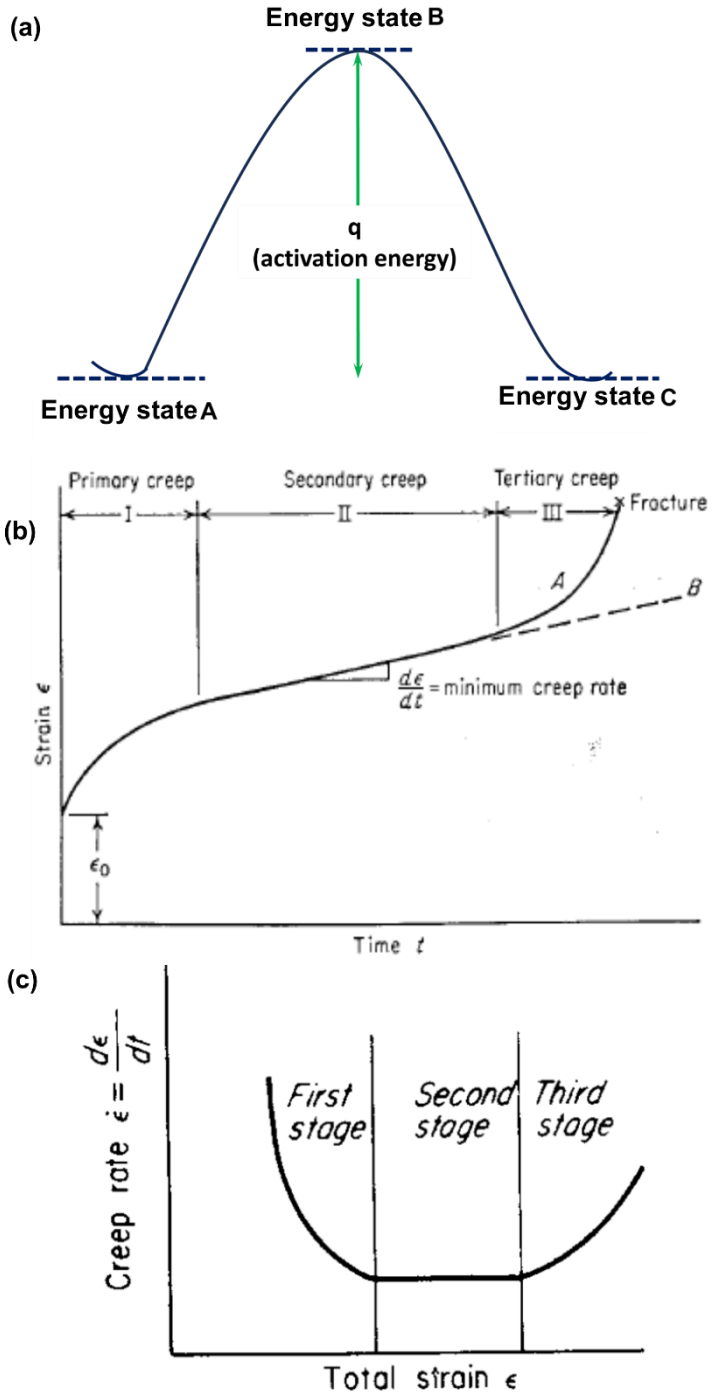

Figure 2.4 (a) Energy states of a dislocation motion while encountering an energy barrier, which interrupts its motion [63]; (b) a typical tensile creep curve showing different stages of creep; and (c) strain rate in creep test as a function of total strain [64].

2.4.1 Classification of creep mechanisms

The creep mechanism involved during the steady-state deformation of a material is predicted from the exponents of the Mukherjee-Bird-Dorn equation associated with the steady-state creep rate. The steady-state creep rate equation is expressed as follows [65]:

$$\dot{\varepsilon}_s = \frac{ADGb}{KT}\left(\frac{b}{d}\right)^p \left(\frac{\sigma}{G}\right)^n \qquad \text{Equation 2.1}$$

In Eq. 2.1 $\dot{\varepsilon}_s$ is the steady-state creep rate (s^{-1}), A is the material constant, b is the Burgers vector (Å), d is the grain size (μm), p is the inverse grain size exponent, n is the stress exponent, G is the shear modulus (MPa), k is the Boltzmann constant (= 1.38×10^{-23} m^2 kg s^{-2} K^{-1}), T is the absolute temperature (K), D is the diffusivity of the material, σ is the applied stress (MPa), and R is the universal gas constant (= 8.314 J/mol^{-1} K^{-1}).

2.4.1.1 Diffusion creep (p = 2 to 3, n = 1)

Diffusion-based creep plays a significant role when the test temperature is high, and the applied stress is significantly low $\left(< \frac{\sigma}{G} = 10^{-4}\right)$. The mechanism is governed by the diffusional flow of the vacancies and interstitials under the influence of applied stress. Depending on the vacancy flow path, the diffusion creep is further categorized as Nabarro-Herring creep (p = 2) and Coble creep (p = 3). In Nabarro-Herring creep, the diffusion flow of vacancies takes place from grain boundaries (GB) experiencing tensile stress to the GBs experiencing compressive stress (atoms flow in opposite directions) through the grain interior. Thus, the elongation of the grain took place, as shown in Figure 2.5(a). In the case of Coble creep, the vacancy diffusion occurs along the GBs, as displayed in Figure 2.5(b) [64].

2.4.1.2 Grain boundary sliding (p = 2 to 3, n = 2)

Grain boundary sliding has a limited contribution to steady-state creep deformation. However, this mechanism becomes dominant when the diffusional flow rate of the vacancies is high. To accommodate grain contiguity, GB sliding occurs during the creep deformation. In this process, GB slides relative to each other along the direction of GB, as shown in Figure 2.5(c). However, the process is not continuous and inhomogeneous, which leads to wavy GB [63].

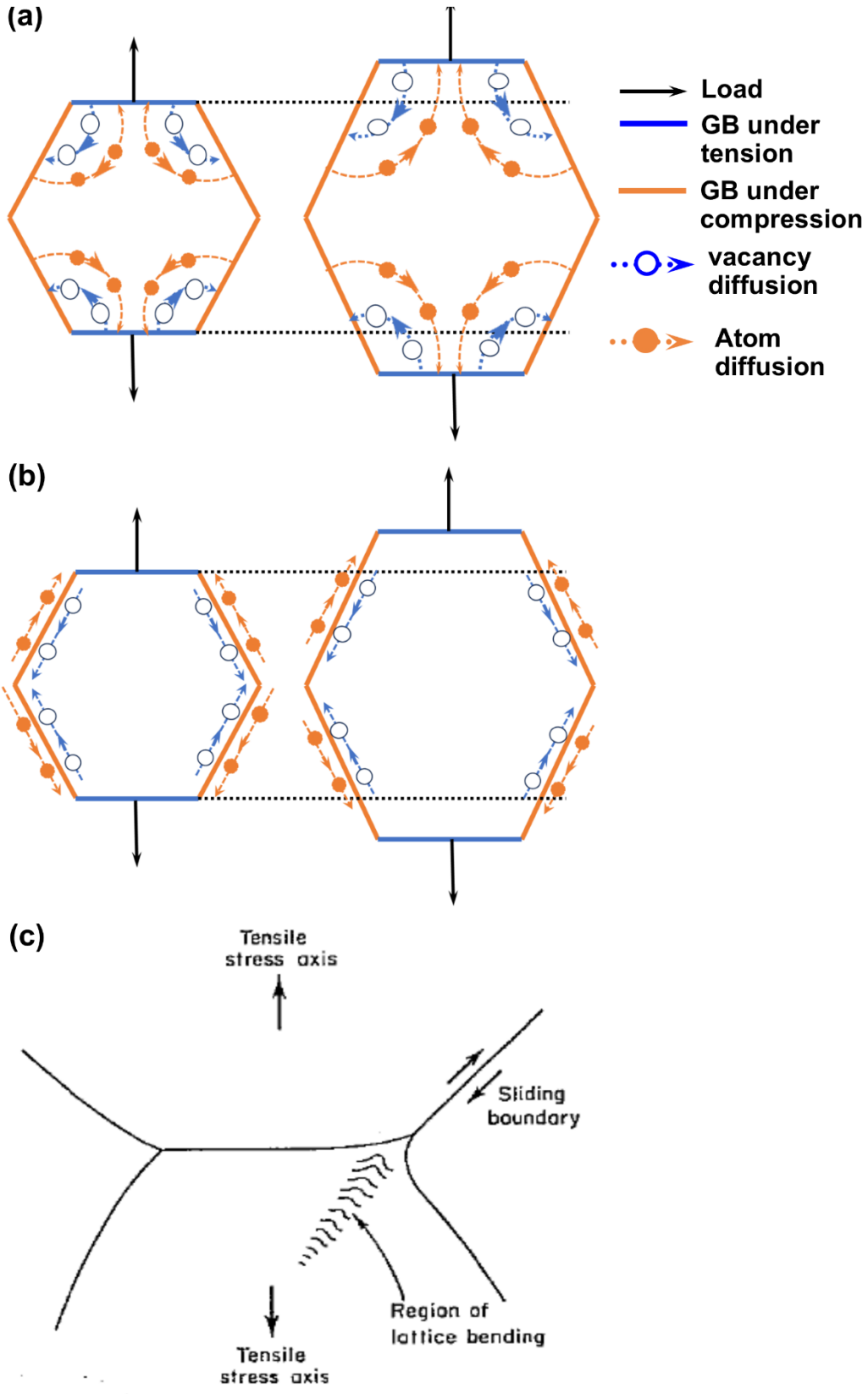

Figure 2.5 Vacancy and atom diffusion direction during (a) Nabarro-Herring, (b) Coble creep; and (c) Grain boundary sliding to accommodate the applied strain at high temperature. [63]

2.4.1.3 Dislocation creep (p = 0, n = 3 to 7)

Dislocation creep occurs by the movement of a dislocation aided by the vacancy diffusion process. The dislocation movement is achieved by glide and climb of the dislocation segment. If obstacles interrupt the dislocation glide, dislocation climbs take place to overcome the obstacle's strain field, as shown in Figure 2.6(a). Therefore, in dislocation creep, the steady-state creep rate is determined by the rate of dislocation climb. The rate of dislocation climb strongly depends on the test temperature that controls the diffusion rate of vacancies. The nature of the vacancy diffusion process can be further divided into two categories, i.e., pipe diffusion and lattice diffusion. The vacancy diffusion took place along the core of the dislocation in pipe diffusion, whereas the vacancy diffusion occurs in the entire lattice for the lattice diffusion process [64].

2.4.2 Impression creep

Impression creep is a variation of indentation creep where the indenter is a flat-bottom cylindrical punch instead of a conical-shaped indenter [66]. Thus, for an applied load, the stress is constant during the entire duration of the experiment. In this case, a flat-headed cylindrical punch is pressed against the sample surface at a constant stress and temperature. Thereafter, the penetration depth is recorded as a function of time by employing an LVDT assembly, as shown in Figure 2.6(b). The depth vs. time plot in impression creep exhibits only two stages of the creep curve, i.e., the primary and secondary stages. Unlike conventional creep, the tertiary stage is not observed in the impression creep owing to the compressive nature of the applied load. The absence of a tertiary creep stage indicates more stable deformation, making the test ideal for characterizing the creep behavior of materials. This method effectively evaluates the steady-state creep rate and creep mechanism from a small quantity test sample, making it a valuable technique for the creep behavior of materials.

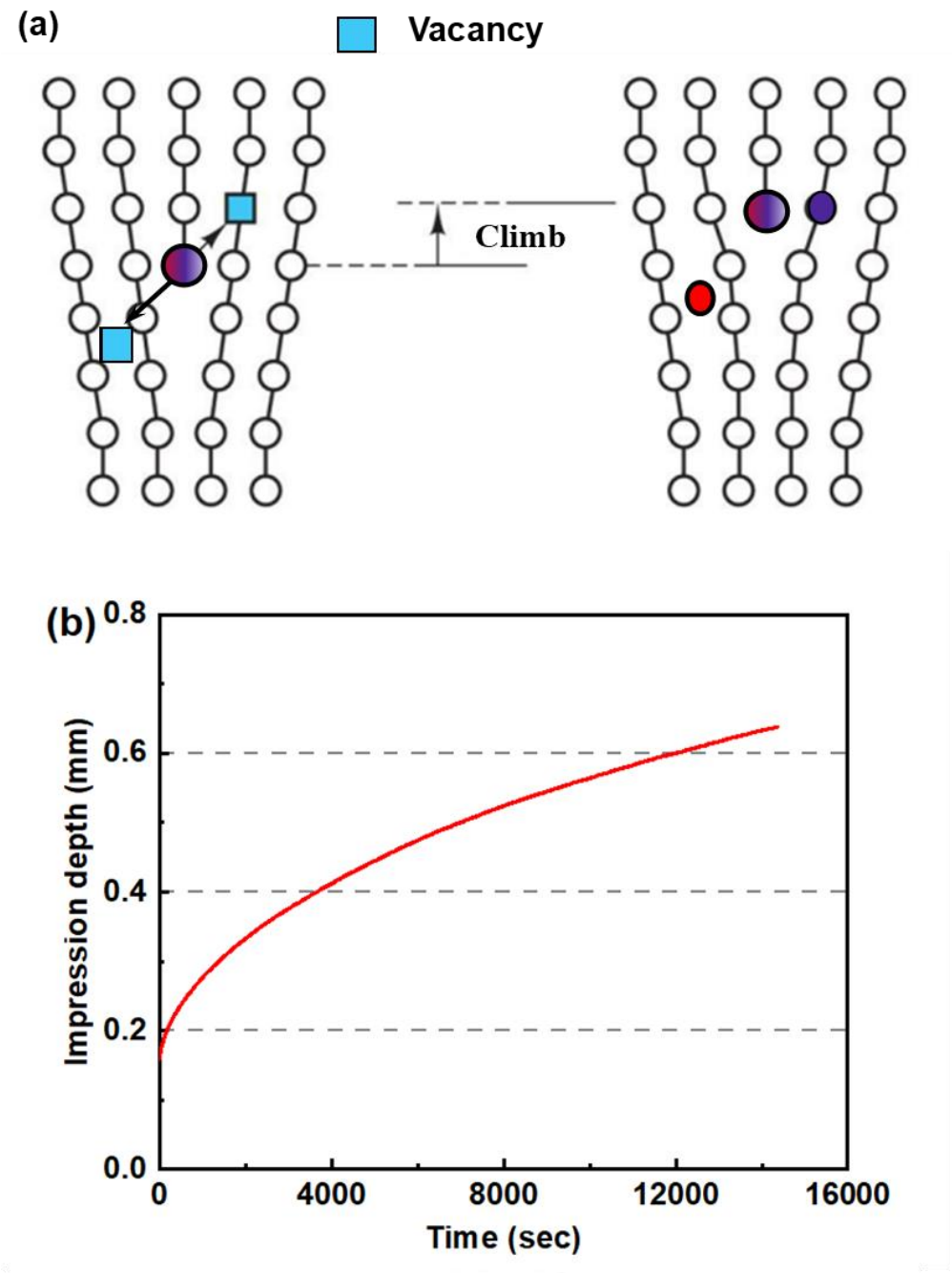

Figure 2.6 (a) A schematic exhibiting dislocation climb assisted by vacancy diffusion, and (b) a typical impression creep curve.

2.4.3 Creep behavior of pure Mg- and Mg alloy-based nanocomposites

Ferkel and Mordike [27] fabricated the Mg-SiC nanocomposite by powder metallurgy technique. They mixed 3.0 (wt.%) of 30 nm SiC powder with 40 μm Mg powder in a ball mill and then performed the hot extrusion to obtain the final nanocomposite. They reported improved creep resistance of the nanocomposite by two order compared to pure Mg. They concluded that the presence of SiC nanoparticles at the grain boundaries strongly opposed the dislocation motion and improved the creep resistance of the nanocomposites. Kastouru et al. [29] investigated the time-dependent plastic deformation of Electron21 alloy and 1.0 (wt.%) AlN reinforced Electron21. The composite was produced by stir casting. The compression creep tests of the composite were performed at 240 °C and at the stress levels of 80, 140, and 200 MPa. The AIN-reinforced Electron21 NC in their study exhibited superior creep resistance under the tested stress and temperature ranges. The calculated stress exponent (n) value of the nanocomposite was 3.3, which indicates the creep deformation mechanism was dislocation climb and glide. Kumar and Chaudhari [28] explored the creep response of the Al_2O_3-reinforced AS41 nanocomposites. The nanocomposites were made by stir casting and ultrasonic processing of the mixture of AS41 melt and 50 nm Al_2O_3 nanoparticles. The creep tests were conducted in the temperature range of 175 to 200 °C and stress range of 109.2 to 140.4 MPa. They found that the additions of 2.0 and 5.0 (wt.%) Al_2O_3 nanoparticles to AS41 improved its creep resistance. The n value was in the range of 3.0 to 6.5, indicating the governing creep mechanism was dislocation creep. The calculated activation energies for the alloy and NCs were 66.17 and 83.77 kJ/mol, indicating that the dislocation creep aided by pipe diffusion was the creep mechanism. Yang et al. [31] examined the creep response of the Electron21 alloy after reinforcing it with 0.5 and 1.0 (wt.%) AlN/Al nanoparticles. The nanoparticles were dispersed in the Electron21 melt using a high-shearing dispersion technique. The alloy and NCs were compression creep tested under the stresses of 70 and 140 MPa at 240 °C. They observed that the NCs with 0.5 (wt.%) reinforcement exhibited the lowest steady-state creep rate among the materials tested. Ganguly et al. [34] performed a creep study on the 0.6 (wt.%) Sb alloyed AZ91 alloy and its nanocomposite with 2.0 (wt.%) of 50 nm SiC nanoparticles (SiC_{np}) fabricated by the squeeze-casting process. They observed that the addition of Sb and SiC nanoparticles decreased the β-$Mg_{17}Al_{12}$ phase formation in the AZ91 alloy. They concluded that the nanocomposite's superior creep performance over the monolithic alloy was from the Orowan strengthening provided by the SiC nanoparticles. In another work, Ganguly and Mondal [30] investigated the influence of 50 nm SiC particles

additions on the creep performance of 2.0 (wt.%) Ca and 0.3 (wt.%) Sb alloyed AZ91 alloy. Microstructural and phase analysis of the alloy and NCs exhibited that the addition of SiC_{np} decreased the formation of the β-$Mg_{17}Al_{12}$ phase and increased the volume fraction of the Al_2Ca phase. The presence of the thermally stable Al_2Ca phase and SiC_{np} significantly enhanced the creep responses of the NCs. They showed that the 2.0 (wt.%) SiC nanoparticles reinforcement significantly decreased the minimum creep rate of the AZ91-2.0Ca-0.3Sb alloy under all the tested conditions. Further, they concluded that the governing creep mechanism was dislocation climb assisted by pipe diffusion. Zhou et al. [33] studied the creep behavior of Mg-9.0Al-1.0Si alloy and its nanocomposite reinforced with 60 nm SiC nanoparticles, while the test temperature and stress were varied from 448 to 498 K and 70 to 90 MPa, respectively. They observed that the addition of nanoparticles improved the creep resistance of the alloy by one order, and the creep life of the NC increased by 34.9%. They concluded that the alloy and nanocomposite deformed under the influence of dislocation creep governed by pipe diffusion. They also concluded that the nanoparticles provided additional strengthening to the alloy, which improved the creep resistance of the NCs. Ganguly et al. [67] reported the effect of 2.0 (wt.%) graphene nanoparticles (GNP) additions on the creep performance of the Mg-9.0Al-1.0Zn alloy. The alloy and GNP-reinforced composites were made using a squeeze casting setup. They observed that the addition of GNP reduced the β-$Mg_{17}Al_{12}$ phase formation, contributing to the nanocomposites' superior creep resistance. Thus, the summary of the literature review concludes that the dispersion of nanoparticles in Mg alloys significantly improved creep resistance.

2.5 Tensile and compression properties

Uniaxial tensile and compression tests are the basic tests used to measure the mechanical behavior of newly developed alloys and composites. A typical engineering stress-strain curve of a material is shown in Figure 2.7 [64]. The stress-strain plot consists of two distinct regions, i.e., elastic and plastic regions. The linear part of the curve represents the elastic region where Hooke's law is valid. The point beyond which the stress-strain curve no longer follows Hooke's law is known as the elastic limit of the material. The stress corresponding to the 0.2% offset strain is known as the yield strength (YS). The maximum stress value in the engineering stress-strain curve is known as the ultimate tensile strength (UTS) or ultimate compressive strength (UCS), depending on the loading mode. In a tensile test at UTS, the necking or localized deformation of the material starts due to an increase in stress, followed by a decrease in the

instantaneous cross-sectional area that dominates over the load-carrying capacity of the material due to strain hardening. The micro-voids and pores combine to form cracks and cause the necking of a material, leading to its failure. However, in the compression test, the micro-voids and pores close up. During compressive loading, the part of the grain rotates in the preferred direction to accommodate the given strain, which is known as deformation bands. These deformation bands further extend across the multiple grains and form shear bands that contribute to the failure of the material in compression [64].

2.5.1 Tensile and compression behavior of Mg- and Mg alloy-based nanocomposites

The effects of additions of different types of nanoparticles, i.e., Al_2O_3, ZnO, TiC, SiC, and so on, in monolithic Mg as well as Mg alloys were investigated by several researchers. Ferkel and Mordike observed that the addition of 3.0 (wt.%) SiC_{np} improved the YS and UTS of pure Mg [27]. However, the segregation of the nanoparticles at the grain boundaries resulted in the poor ductility of the Mg-SiC_{np} composites in their study. Hassan and Gupta [68] fabricated the Mg-Al_2O_3 nanocomposite (50 nm) using the disintegrated melt deposition technique. They observed an improved tensile strength with ductility of the Mg-Al_2O_3 nanocomposite produced by powder metallurgy. The Young's modulus, YS, UTS, and % El of the NCs improved by 23.1, 80.4, 42.2, and 89.2%, respectively. They concluded that the activation of non-basal slip systems in the presence of NPs improved the ductility of the NCs. They further mentioned that the grain refinement owing to the heterogeneous nucleation in the presence of NPs was beneficial. The addition of NPs changed the fracture mode of pure Mg from brittle fracture to a mixed mode of fracture. Hassan and Gupta, in another study, reported improved hardness, 0.2% YS, UTS, and ductility of pure Mg by incorporating 1.1 (vol.%) of Al_2O_3, Y_2O_3, and ZrO_2 nanoparticles [69]. They also observed that among the added NPs, the Al_2O_3 was effective in improving the tensile strength of pure Mg. The YS and UTS were improved by 46.9 and 29.5%, respectively. They concluded that the better interfacial bonding between the Al_2O_3 and Mg matrix was the reason for the enhanced tensile strength of the Mg-Al_2O_3 NCs. Interestingly, they found that the addition of ZrO_2 NPs was more effective in improving the elongation of the Mg matrix. They also investigated the effect of different sizes of Al_2O_3 particles on the mechanical properties of pure Mg [70]. The composites were manufactured by adding 50 nm, 0.3 μm, and 1μm Al_2O_3 particles in Mg melt. They observed that the addition of 50 nm particles to pure Mg improved its elongation by 89.0%. They concluded that adding nano Al_2O_3 particles

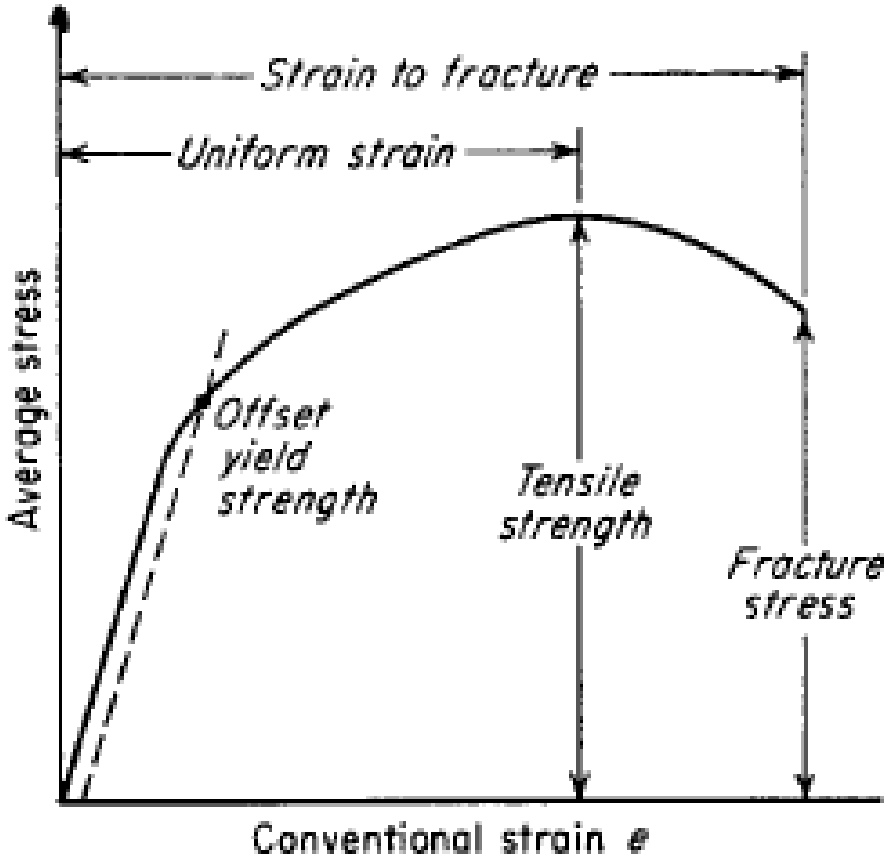

Figure 2.7 A typical engineering stress-strain curve exhibiting 0.2% yield strength, ultimate tensile strength, and fracture strength [64].

improved the ductility of pure Mg, owing to better grain refinement and distribution of the reinforcement phase. Goh et al. [71] fabricated the NCs by dispersing 0.5, 1.0, and 2.0 (vol.%) Y_2O_3 nanoparticles in pure Mg. They reported that the addition of the 2.0 (vol.%) Y_2O_3 improved the YS and UTS of pure Mg by 28.5 and 18.2%, respectively, whereas the elongation was reduced by only 1.0%. The improved strength of the NCs was attributed to the grain refinement of the NCs owing to heterogeneous nucleation during solidification. They further mentioned that the lower activity of the non-basal slip system was responsible for the low ductility of the NCs. Nguyen and Gupta [72] fabricated the AZ31B-Al_2O_3 NCs by mixing 0.66, 1.11, and 1.50 (vol.%) of 50 nm-Al_2O_3 with the AZ31B alloy. They observed the enhancement of the CYS by 32.0% and UCS by 10.0% of the AZ31B alloy due to the addition of 1.5 (vol.%) Al_2O_3 nanoparticles. Hui et al. [73] stated that the incorporation of 0.5 (wt.%) SiC_{np} in the AZ91 alloy improved the YS, UTS, and %El by 19.0, 24.0, and 83.0%, respectively. The enhancement of the mechanical property was attributed to the grain refinement of the NCs. Paramsothy et al. [74] showed that the dispersion of Al_2O_3 nanoparticles in the AZ alloy enhanced ambient temperature tensile properties as well as compressive properties of the alloy. The fractographic analysis of the alloy and NCs reveals that both materials experienced mixed fracture modes. However, the dimple-like feature was more prominent in the factograph of NCs, contributing to the enhanced ductility of the NCs compared to the alloys. Sankaranarayanan et al. [75] fabricated two separate composites of Mg-Ti and Mg-Cu by mixing 5.6 and 3.0 (wt.%) of 140 µm Ti and 50 nm Cu particles. They concluded that the addition of nanosized particles was more effective than micron-sized particles in enhancing the mechanical behavior of pure Mg. The formation of Mg-Cu intermetallic and the distribution of Cu particles along the grain boundaries of pure Mg were responsible for the improved mechanical properties of the NCs. In a different work, Sankaranarayanan et al. reported that the incorporation of 0.16, 0.48, and 0.8 (vol.%) of 90 nm ZnO particles also improved the ambient temperature tensile and compressive properties of pure Mg [76]. The additions of ZnO increased the dislocation activity at the prismatic plane, which helped to improve the mechanical properties of the alloy. Furthermore, they mentioned that the dislocations were successfully pinned by the ZnO nanoparticles, which enhanced the strength of the composites. Khosroshahi et al. [77] investigated the effect of TiO_2, SiC, and Al_2O_3 nanoparticles on the mechanical properties of AZ80 Mg alloy. Among the NCs, the SiC-reinforced AZ80 composite exhibited superior YS and ductility, owing to a better distribution of SiC nanoparticles. Meenashisundaram et al. too observed the enhancement of ambient temperature tensile and compressive properties of monolithic Mg after adding 2.0 (wt.%) TiO_2 nanoparticles [78]. The

nanocomposite containing 2.5 (wt.%) of nanoparticles exhibited enhanced YS and UTS by 37.0 and 9.0%, respectively, in their study. Katsarou et al. [29] reported the enhancement of ambient temperature CYS of the AIN-dispersed Elktron21 nanocomposite. Chen et al. [79] studied the dynamic compressive loading response of the Mg-4.0Zn-3.0Gd-1.0Ca alloy containing 2.0 (wt.%) ZnO nanoparticles. They concluded that the nanoparticles hindered the growth of twins at grain boundaries, resulting in enhanced YS of the nanocomposites. Parande et al. [80] too observed the enhanced ambient temperature tensile properties of pure Mg by the dispersion of nano-NiTi (Nitinol). Furthermore, Ganguly et al. [81] also reported the enhancement of ductility and tensile properties of the AZ91-Ca-Sb alloy by adding 0.5, 1.0, and 2.0 (wt.%) SiC_{np}. Chen et al. [82] investigated the effect of different sizes of SiC on the mechanical properties of Mg-2.0Zn-0.1Y alloy. They reported that the nanosized SiC particles greatly enhanced the strength and ductility of the alloy.

2.6 Corrosion

Corrosion is a reaction that occurs with a material and its surrounding environment, resulting in the deterioration of the material [83]. All environments are mildly or aggressively corrosive to all kinds of metals. In real life, all the mediums, for example, water, air, moisture, gas, steam, alkaline, acidic etc., tend to corrode the material. The corrosive nature of the inorganic materials is higher compared to the organic materials. Apart from this, catastrophic environments involving high temperature and pressure also significantly influence the material's corrosion behavior [83]. Therefore, in the course of selecting the structural material, it is essential to consider the corrosion behavior of the material in the targeted environment. Depending on the nature of the corrosive medium, corrosion can be classified as (a) wet corrosion and (b) dry corrosion.

The corrosion that takes place in the presence of a liquid environment is known as wet corrosion. The structural materials that undergo marine transport services are often exposed to Cl-rich water, which leads to severe corrosion of those components under wet conditions. Dry corrosion occurs in the absence of a liquid medium. In these cases, gases act as a corrosive medium. In various high-temperature reactors, the flue gases can impart dry corrosion on the structural material.

Magnesium (Mg) is known to have poor corrosion resistance among structural materials. Mg corrosion becomes significant when it contains specific elemental impurities like iron, nickel, cobalt, and copper. They act as cathodes and lead to the degradation of Mg. Mg becomes vulnerable to corrosion when exposed to species like Cl^-. The electromotive force series shows that the -2.37 V is the standard electrode potential of Mg in interaction with a solution containing Mg^{2+}. The value is the lowest among the metals used for the structural components, leading to its significant corrosion of the Mg. Therefore, Mg and Mg-based alloys are affected by several corrosion mechanisms, which are discussed in the following section [84].

2.6.1 Galvanic corrosion

Galvanic corrosion is usually identified by the severely corroded localized regions that are close to the cathode. The cathode can be a separate metal in close contact with Mg or a secondary phase in the Mg-based alloys [84]. In the internal case, the secondary intermetallic phase, like β-$Mg_{17}Al_{12}$, severely damages the α-Mg phase, causing it to defoliate from the alloy. The rate of galvanic corrosion is affected by several key factors, namely potential difference, separation distance, and contact area between cathode and anode.

2.6.2 Pitting corrosion

Pitting corrosion results from the extremely localized corrosion attack, leading to pit formation on the metals. The diameter and depth of the pits may vary significantly, indicating inhomogeneity of the reaction process. The pit formation might lead to catastrophic failure of the component in service. The pitting corrosion's undetectability makes it a more dangerous form of corrosion for structural materials. Further, the lab experiments are unable to detect this kind of corrosion [83].

2.6.3 Intergranular corrosion

Intergranular corrosion takes place along the grain boundaries of an alloy. However, the intergranular corrosion of Mg-based alloy is not significant owing to the comparably more cathodic intermetallic phase formation than the α-Mg phase. Therefore, the corrosion in Mg alloys is unable to penetrate inside the crystal through the grain boundaries [83].

2.6.4 Stress corrosion cracking

The combined effect of tensile stress and corrosion leads to the accelerated growth of the crack tip, which leads to premature failure of the component under the same stress imparted. This

type of fracture can be transgranular and intergranular in nature. According to various studies, stress corrosion cracks lead to intergranular fractures of Mg-Al-based alloys due to the interconnected secondary phase network. The formation of MgH_2 also leads to the hydrogen embrittlement of these alloys [64,83].

2.6.5 Corrosion at elevated temperature

The oxidation rate of the Mg alloy changes proportionally with the increase in temperature. The formation of the MgO layer on the surface of the Mg alloy took place. The unstable layer of MgO deteriorates quickly, compromising the alloy's integrity. It is observed that the high-temperature oxidation rate of Mg increases as the concentration of Al, Zn alloying increases in Mg. However, several studies indicate that adding Ce, Ca, and La improves the oxidation behavior of Mg alloy more than pure Mg [83].

2.6.6 Corrosion behavior of Mg- and Mg alloy-based nanocomposites

Mg alloys reinforced with microparticles exhibited more detrimental corrosion properties than the parent alloy. Tiwari et al. [85] showed that adding 25 μm SiC particles in pure Mg significantly reduced the corrosion resistance of the micro-particle reinforced composites. The addition of micro-SiC in Mg introduced additional defects in the corrosion film owing to matrix-SiC discontinuity, which resulted in the poor corrosion resistance of the composites. Turan et al. [39] reported that adding carbonaceous particles deteriorated the corrosion properties of the AZ91 alloy. The strong galvanic corrosion between carbonaceous particles and α-Mg was responsible for the poor corrosion resistance of the composites. Zhang et al. [40] too published a similar report of micro-SiC addition in the AZ91 alloy, while corrosion was tested in a 3.5 (wt.%) of NaCl solution. They mentioned that the refinement and preferential recrystallization of the β-$Mg_{17}Al_{12}$ phase around the micro-SiC particles resulted in higher galvanic corrosion of the AZ91-SiC composites. Mondal et al. [41] compared the corrosion resistance of the AE42 alloy and its hybrid composites and reported an adverse effect of the reinforcement phases on its corrosion response. They, too, mentioned that the irregular corrosion film formation on the surface of the composites was inefficient in providing adequate corrosion protection. However, recent studies suggested that adding nanoparticles might significantly protect the Mg-based alloys from corrosion [42,43]. Ganguly et al. [44] studied the impact of SiC_{np} addition on the corrosion behavior of AZ91-2.0Ca-0.3Sb alloy and reported a decreased corrosion rate of the nanocomposites compared to the squeeze-cast alloy. They

observed that the decreased volta potential between α-Mg and β-$Mg_{17}Al_{12}$ phases was responsible for the improved corrosion resistance of the NCs. However, the factors responsible for the decrease in the volta potential were not explained. Esmaeilzadeh et al. [45] explored the corrosion performance of micro and nano-sized ZnO-reinforced WE43 alloy. The improved corrosion resistance of WE43-based nanocomposites was attributed to the grain refinement and redistribution of secondary phases achieved from the ZnO nanoparticles addition. The above review concludes that the microparticles reinforcement deteriorated the corrosion resistance of the Mg alloys, whereas, the nanoparticle dispersion improved the corrosion resistance of the Mg alloys. However, the mechanism of improvement in corrosion resistance following the nanoparticle additions in the Mg alloys, as well as the effects of volume fractions of nanoparticles on corrosion behavior, is not yet fully understood.

2.7 Motivation for the thesis

The Mg-Al-based alloys are known for their high specific strength. However, their application is restricted to ambient temperature owing to their poor high-temperature properties and corrosion behavior. The RE, Sr, and Ca alloyed Mg-Al-based alloys can be used up to 473 K. Ca is a cheaper and easily available alternative to RE elements among the mentioned elements. The newly developed Mg-Al-Ca-Mn alloy has the potential to serve at 473 K. However, automotive powertrain components demand applications beyond 473 K. The dispersion of nanoparticles in pure Mg and Mg alloys imparts significant enhancement in creep properties. Considering this, the SiC_{np}-dispersed Mg-5.0Al-2.0Ca-0.3Mn (wt.%) (AXM520) alloy and nanocomposites (NCs) are developed in the present thesis. The effects of SiC_{np}-dispersion on the microstructure, tensile, compression, creep, and corrosion behavior of these NCs are studied. Further, age-hardening improves the strength of Mg alloys. Unfortunately, to the best of the authors' knowledge, the creep behavior of age-hardened and dispersion-strengthened Mg alloys has not been explored yet. Therefore, the microstructural alteration and creep charectaristics of the squeeze-cast age-hardened AXM520 alloy with SiC nanoparticles additions are also investigated.

Chapter 3

Experimental Procedure

The details of the fabrication process of the Mg-5.0Al-2.0Ca-0.3Mn (wt.%) (AXM520) alloy and nanocomposites are discussed in this chapter. In addition, the details of the experimental setups and relevant equations used to produce the experimental data and their methods of analysis are discussed.

3.1 Fabrication of alloy and nanocomposites

The AXM520 (Mg-5.0Al-2.0Ca-0.3Mn (wt.%)) alloy was manufactured from pure Mg (~99.9%) as well as Mg-30.0Ca (wt.%) and Al-10.0Mn (wt.%) master alloys (Oswal Minerals Limited, India). The AXM520 alloy-based nanocomposites (NCs) were produced by adding 0.5, 1.0, 2.0, and 3.0 (wt.%) SiC_{np} (average diameter 60 nm, Ultra Nanotech, India). The targeted and achieved compositions of the AXM520 alloy and NCs with their designations are summarised in Table 3.1.

Table 3.1 The sample designations and compositions of the alloy and nanocomposites.

Sample designation	Measured composition (wt.%)							Nanoparticles content (wt.%)
	Al	Ca	Mn	Fe	Ni	Cu	Mg	
AXM520	4.95	2.01	0.28	0.004	0.001	0.002	Balance	0
NC0.5SiC	5.01	1.99	0.27	0.006	0.001	0.001	Balance	0.5% SiC
NC1.0SiC	4.97	2.02	0.30	0.003	0.001	0.001	Balance	1.0% SiC
NC2.0SiC	5.03	1.97	0.28	0.005	0.002	0.003	Balance	2.0% SiC
NC3.0SiC	5.02	2.01	0.29	0.006	0.001	0.002	Balance	3.0% SiC

The alloy and NCs were prepared utilizing a squeeze-cast setup with a bottom pouring facility (Swamequip, India). In the beginning, the furnace of the casting setup was allowed to attain a temperature of 1023 K by resistance heating. After attaining the temperature, the Mg ingots were placed inside the graphite crucible located inside the furnace. Once the Mg ingots were melted, the calculated amounts of the preheated (473 K) Mg-Ca, Al-Mn master alloys, and

SiC_{np} were added to the Mg-melt. A mixture of the Ar and SF_6 gases in the ratio 99.5:0.5 (vol.%) was passed to the melt to prevent oxidation. The melt was stirred at 300 rpm for 5 min once the melt temperature reached 1023 K. The stirring process ensured the mixing of the added alloying elements and SiC_{np} with molten Mg. The liquid mixture was then allowed to settle at 1023 K for 1 min. The melt from the crucible was passed into a mild steel mould heated to 523 K. A vertically installed hydraulic ram squeezed the melt into the mould at 200 MPa. The melt solidified in about 60 s under 200 MPa. The final shape of the cast ingot was cylindrical, with a radius of 25 mm and 200 mm long. The compositions of all the materials were determined by an ICP-MS (Agilent Technologies, 7900).

3.2 Microstructural characterization of alloy and nanocomposites

3.2.1 X-ray Diffraction (XRD)

The phases present in the samples were investigated using XRD (PANalytical) employing CuK_α radiation (scan speed: 2 °/min). The X-ray diffraction data was then recorded in the 2θ range of 20 to 90 °.

3.2.2 Optical Microscopy (OM) and Scanning Electron Microscopy (SEM)

The microstructures of the as-cast alloy and NCs were studied using Optical Microscopy (OM) (LEICA DM2500M) and Field Emission Scanning Electron Microscopy (Carl Zeiss, Supra 40) furnished with an Energy-Dispersive X-ray Spectroscopy (EDS)(Oxford Instruments). The alloy and NCs were subjected to standard metallographic techniques. The samples were ground using 400, 800, 1000, 2000, and 2500 grit emery papers, followed by polishing with 1.5 and 0.5 μm diamond paste. The specimens were etched using a solution of 5 g picric acid, 100 ml ethanol, 20 ml H_2O, and 10 ml acetic acid. The Image-J software was employed on the SEM micrographs to estimate the fraction of the phases present.

3.2.3 Fractal analysis

The connectivity of the phase was assessed with the help of fractal analysis using SEM images. The SEM micrographs were converted into binary images, and then they were examined by an 'Image analysis algorithm'. The algorithm identified the largest connected mass (D_{max}) present in the image. Thereafter, the algorithm reconstructed the largest connected mass separately. The reconstructed image was then used to calculate the fractal dimension (D_f) using the pixel

counting method [35]. The total number of boxes required to cover the D_{max} was expressed as a function of edge length x (N(x)) as per Eq. 3.1.

$$N(x) = x^{-D_f} \quad \text{Equation 3.1}$$

3.2.4 Transmission Electron Microscopy (TEM) analysis

The Transmission Electron Microscopy (TEM) (FEI, Tecnai G2 20 TWIN) analysis was performed by taking a 3 mm disc from the as-cast ingot. Initially, the foils were mechanically thinned to 1 mm and then ion-milled (Gatan, Duo Mill 600) to make them electron-transparent.

3.3 Mechanical characterization of alloy and nanocomposites

3.3.1 Tensile and compressive tests

The tension and compression tests were conducted on the AXM520 alloy and NCs at ambient temperature under uniaxial loading. The specimens for both tests were prepared according to the ASTM-E8 and ASTM-E9 standards, respectively. The cast ingot was cut into small pieces and machined to the standard dimensions. A 50 kN Universal Testing Machine (UTM) (BISS, Electra 50) was employed to perform the tensile and compression tests. All the tests were performed using a constant strain rate, i.e., 8.334×10^{-5} s^{-1}. Three tests were performed at each parameter to evaluate the tensile and compressive properties.

3.3.2 Impression creep tests

The impression creep tests were carried out with a lever-based impression creep tester (SPRANK/3123/03/21, SPRANKTRONICS, India). The lever has an arm ratio of 1:10. One end of the lever was attached to a specimen holder, and the other end of the lever was connected to a loading cage. The indenter with the specimen holder was placed inside an electric resistance furnace. After that, the furnace was heated to a targeted temperature, and the entire arrangement inside the furnace was held at the temperature for 1 h to ensure thermal equilibrium. Then, the indentation process was started. A flat-end cylindrical tungsten carbide indenter of 1.0 mm diameter was employed for indentation. The specimens of 10×10×10 mm^3 were used in the creep tests. The surfaces of the samples were cleaned using 1000 and 2000-grade emery papers before conducting the creep tests. The indentation depth was acquired using a sensor as a function of time. The selected ranges of temperature and stress for the impression creep tests were 390 to 490 MPa and 448 to 523 K, respectively.

3.3.3 Post-creep microstructural study

The microstructural changes and materials flow below the indentation of crept samples of the AXM520 alloy, and NCs were further examined. The indentations were bisected to obtain the flow patterns, as shown in Figure 3.1, and observed under SEM after standard polishing. The samples for Electron Backscatter Diffraction (EBSD) observation were electropolished (Lectropol-5, Struers) using a solution of 30% nitric acid and 70% methanol for 15 s with a voltage of 12 V. The EBSD data were acquired using an FE-SEM with a scanning step size of 1.5 µm.

3.4 Corrosion tests of alloy and nanocomposites

3.4.1 Hydrogen evolution and immersion tests

For hydrogen evolution tests, the samples of the AXM520 alloy and NCs were polished with 400, 800, 1000, 1500, and 2000 grades of emery papers, followed by cloth polishing using 1.0 and 0.5 µm diamond pastes. The samples were then exposed to a 3.5 (wt.%) aqueous NaCl solution at a pH of 7.0. An area of 15×15 mm^2 of the respective specimen was exposed to the solution for 60 h at 25 ± 2 ºC. The evolved hydrogen was collected using the water displacement technique in a measuring cylinder. Three samples of each variant were tested under identical conditions to check the reproducibility of the tests. The corrosion rates (mm/yr) of the alloy and NCs were calculated from the hydrogen evolution rate (ΔV_H) (ml/cm^2) for the exposed duration (t) (h) using the density (ρ) (1.74 g/cm^3) as per the following equation [44].

$$\text{Corrosion rate (mm/yr)} = \frac{94.608 \times \Delta V_H}{\rho \times t} \qquad \text{Equation 3.2}$$

The values of weight loss of the AXM520 alloy and NCs specimens (area 15×15 mm^2) were also recorded after immersion in NaCl solution for 60 h. The corrosion rates of the alloy and NCs were calculated using the following equation:

$$\text{Corrosion rate (mm/yr)} = \frac{87600 \times \Delta w}{\rho \times A \times \text{t}} \qquad \text{Equation 3.3}$$

where A (cm^2) is the exposed area of the specimen, and Δw is the weight loss (in g) measured after the removal of the corrosion products.

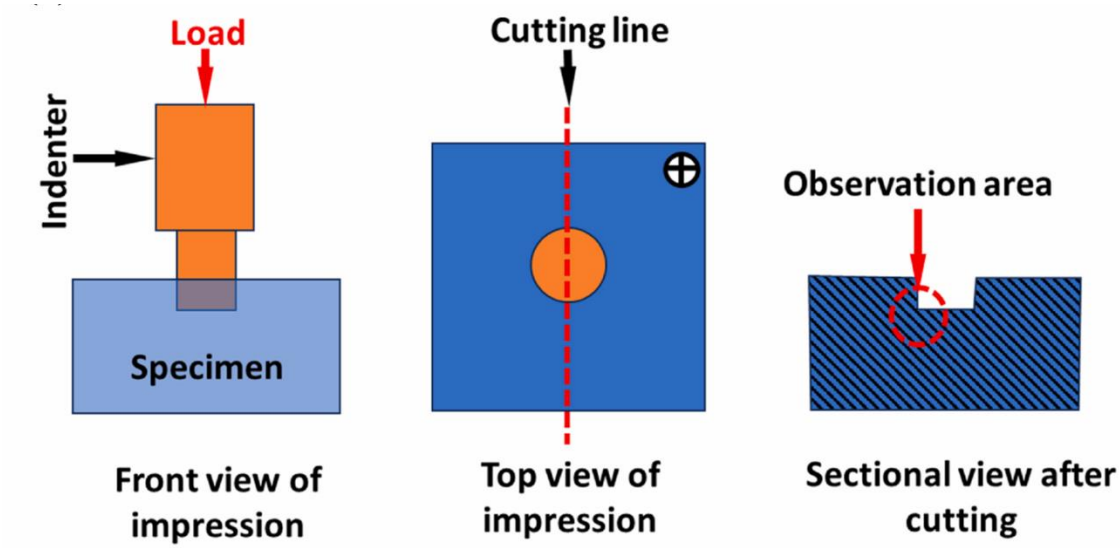

Figure 3.1 Schematic portraying the region of microstructural analysis below indentation after creep test.

3.4.2 Electrochemical corrosion tests

The electrochemical corrosion tests of the alloy and NCs were performed by employing an electrochemical workstation (Corrtest, CS350). The tests were done using a conventional three-electrode system. The alloy and NCs were used as a working electrode. A platinum net and Ag/AgCl with 3 mol KCl solution were used as a counter electrode and reference electrode, respectively. The entire enclosure was then filled with 3.5 (wt.%) aqueous NaCl solution, and a 10 cm^2 sample area was exposed to the solution. After that, the alloy and NCs' open circuit potential (OCP) was measured for 3600 s to ensure the stable E_{OCP} before conducting other electrochemical corrosion tests. Then, the electrochemical impedance spectroscopy (EIS) was performed, followed by a potentiodynamic polarization test. The EIS of each sample was measured from 100 kHz to 0.01 Hz, with ± 10 mV with respect to OCP. The potentiodynamic polarization test was conducted at OCP - 300 to OCP + 400 mV and the potential was varied at 0.01 mV/s.

3.4.3 Measurement of volta potential

The volta potential difference between the primary α-Mg and secondary $(Mg,Al)_2Ca$ (C36) phases of AXM520 and NC3.0SiC was measured using a Scanning Kelvin Probe Force Microscopy (SKPFM) (NT-MDT Service and Logistics Ltd., NTEGRA Prima). Before the experiment, the samples were polished, as mentioned earlier, and then cleaned using ethanol. The measurement was performed in a controlled atmosphere of 25 ± 2 ºC. A Pt-coated Si tip with 20 ± 10 nm was employed to map the surface profile and potential difference. The surface profile was measured using the tapping mode, while the potential signal was measured by raising the cantilever at a height of 50 nm.

3.4.4 Analysis of corrosion products

The morphology of the corroded film deposited on the alloy and NCs was captured by an SEM (Carl Zeiss Microscopy Ltd., EVO-Scanning Electron Microscopy MA15/18) with an EDS facility (Oxford Instruments Nanoanalysis, 51N1000 - EDS System). The corroded film's XRD diffraction pattern was recorded using Cu-K_α radiation (PANalytical) with a scanning speed of 5 º/min. Further, the corroded film's Fourier Transform Infrared Spectroscopy (FTIR) (Thermo Electron Scientific Instruments LLC, Nicolet iS5) was recorded in attenuated total reflectance mode. The FTIR spectra were recorded in the range of 550 to 4000 cm^{-1}. The corrosion product's X-ray photoelectron spectroscopy (XPS) (Thermo Fisher Scientific, K-Alpha) was

also performed using an Al-K_α X-ray source. The 3D profilometry and SEM observation of the corroded surfaces were performed after removing the corrosion products using a 100 ml aqueous solution of 20 and 10 g of CrO_3 and $AgNO_3$, respectively.

3.5 Heat treatment of alloy and nanocomposites

The samples of 10×10×10 mm^3 were cut from the cast ingot. The specified samples were then homogenized in a tube furnace at a temperature of 773 K for 8 hr in Ar atmosphere and, subsequently, water quenched. The homogenized samples were artificially aged in a muffle furnace at a temperature of 523 K.

3.6 Designations of aged alloy and nanocomposites

The alloy is designated as AXM520HT, and the nanocomposites containing 1.0 and 2.0 (wt.%) of SiC_{np} are designated as NC1.0SiCHT and NC2.0SiCHT, respectively.

3.7 Hardness measurement

The aged samples were then taken out from the muffle furnace at a regular intervals of 30 min to measure their hardness using a Vickers hardness tester (Vertex Engineers & Associates, HV-50A). The applied load and dual time were 1 kgf and 10 sec, respectively.

Chapter 4
Microstructural Characterization

This chapter illustrates the detailed microstructural characterization of the Mg-5.0Al-2.0Ca-0.3Mn (wt.%) (AXM520) alloy and nanocomposites. The microstructural characterization was carried out using X-ray Diffraction (XRD), Optical Microscopy (OM), Scanning Electron Microscopy (SEM), and Transmission Electron Microscopy (TEM). The XRD detected the various phases present in the microstructure of the alloy and nanocomposites. The representative micrographs for all the alloys were taken using OM and SEM. The composition of the phases was analyzed by the Energy-Dispersive X-ray Spectroscopy (EDS) attached to the SEM and TEM. The major outcomes of the present chapter are summarised at the end.

4.1 X-ray diffraction analysis

The ambient temperature solid solubilities of Ca and Mn in Mg are negligible. Therefore, the formation of Ca- and Mn-rich intermetallic phases in the AXM520 alloy is expected. Figure 4.1(a to c) presents the X-ray diffraction patterns obtained from the alloy and nanocomposites (NCs). Analysis of the XRD patterns confirmed the existence of the Mg solid solution (i.e., α-Mg) and $(Mg,Al)_2Ca$ (C36) (M. P. 988 K) phases in the alloy and NCs. The magnified view of the XRD patterns of the AXM520 alloy and NC3.0SiC (representative picture of the NCs) in the 2θ range from 30 to 50 are presented in Figure 4.1(b). The XRD peaks obtained from the C36 phase are shown. Thus, the intensity of the XRD pattern for the C36 phase is reasonably prominent, and it is as per the pattern reported by Zubair et al. [58] for the same phase. The Al_8Mn_5 phase was also observed in the AXM520 alloy and NC3.0SiC. As expected, the presence of the SiC phase was confirmed in the XRD pattern of the NC3.0SiC. The β-$Mg_{17}Al_{12}$ (A12) (M. P. 733 K) phase was suppressed in the alloy and NCs employed in the current investigation, and the suppression was attributed to the chosen Ca/Al ratio of 0.40. Similar results were also observed by other researchers [13,14]. Ninomiya et al. [15] concluded that the occurrence of the Al_2Ca (C15) phase (M. P. 1352 K) suppressed β phase in the Mg-Al-Ca alloy containing a ratio of Ca to Al of 0.11. They also observed that further incorporation of

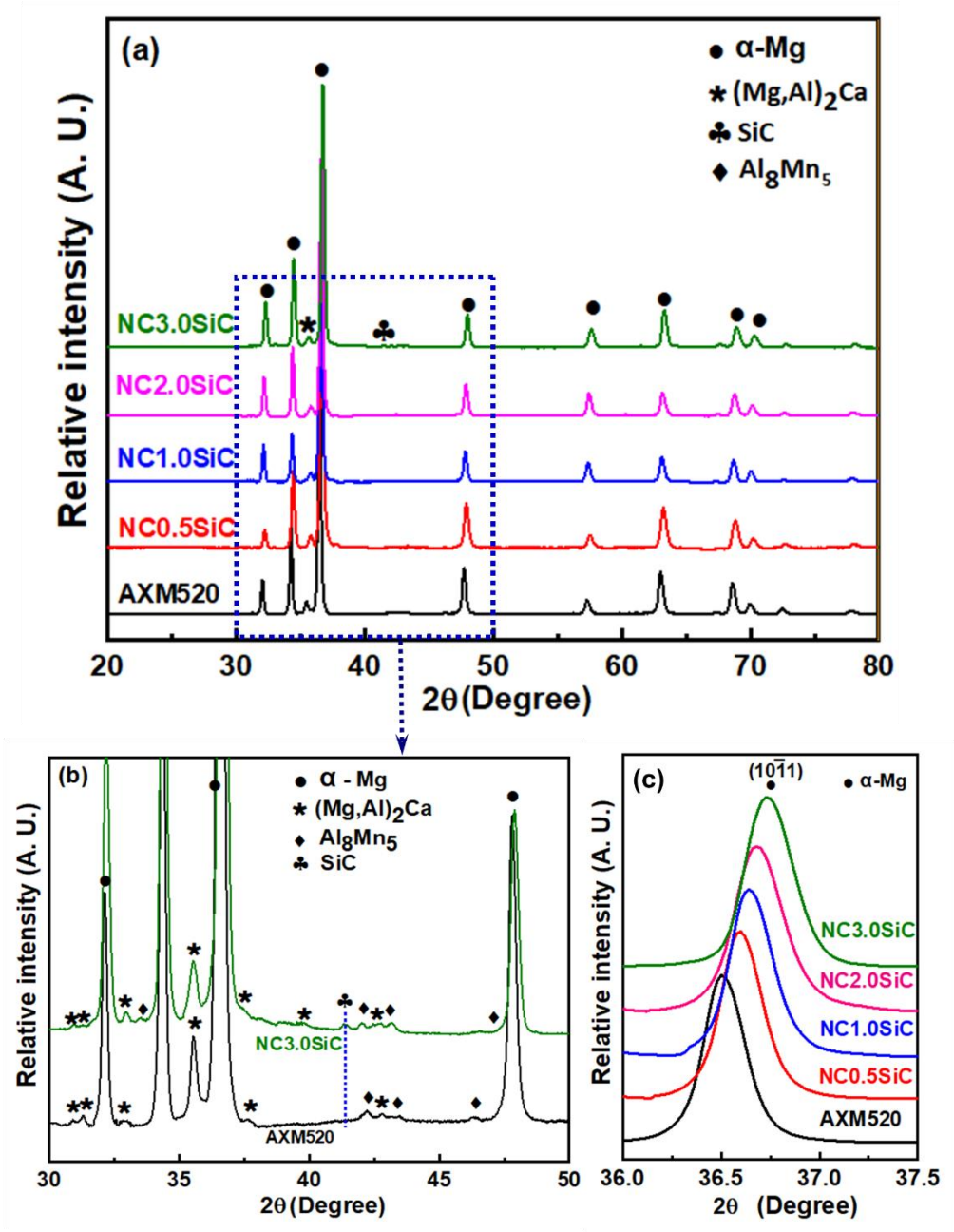

Figure 4.1 (a) XRD patterns obtained from the as-cast AXM520 alloy and all the nanocomposites; (b) magnified view of the XRD patterns obtained from the AXM520 alloy and NC3.0SiC in the 2θ range from 30 to 50 °; and (c) magnified view of the 2θ range from 36.0 to 37.5 ° confirming the shift of the high-intensity peak of the α-Mg phase.

Ca (Ca/Al ≥ 0.83) in the Mg-Al-based alloys encouraged the formation of the Mg_2Ca (C14) (M. P. 988 K) phase along with the Al_2Ca (C15) phase. Table 4.1 summarises the phases previously reported [56,59,86-89] in the Mg-Al-Ca-Mn alloys with a Ca/Al fraction close to that of the present investigation, i.e., Ca/Al = 0.40. The presence of the $(Mg,Al)_2Ca$ (C36) phase is evident in all the alloys. The presence of the Al_8Mn_5 phase in the Mg-Al-Ca-Mn alloys was reported by other researchers as well [59,88]. No peaks corresponding to alumosilicate and Mg_2Si were detected in the XRD patterns, confirming the absence of reaction products. The enlarged view of the $(10\bar{1}1)$ peaks corresponds to the α-Mg phase present in the alloy, and NCs are shown in Figure 4.1(c). It is evident that the high-intensity peak of the α-Mg phase shifted towards the right of the XRD patterns as the concentration of the SiC_{np} increased in the AXM520 alloy. The presence of SiC_{np} hinders solid rejection during solidification of the NCs by encapsulating the solid phase [90,91]. In the present investigation, Al rejection from the α-Mg phase nuclei was hindered owing to the presence of the SiC_{np}, which resulted in the enrichment of the α-Mg phase. The atomic radii of Mg and Al are 150 and 125 pm, respectively [92]. Therefore, the lattice contraction of the α-Mg phase took place, which contributed to the right shift of the $(10\bar{1}1)$ peak.

Table 4.1 Summary of the phases formed in the Mg-Al-Ca-Mn alloys reported in the literature.

Alloy	Composition (wt.%)				Phases present in as-cast condition	Ref.
	Al	Ca	Mn	Ca/Al		
AXM5203	4.50	1.90	0.27	0.42	α-Mg, C36	[86]
AXM523	5.11	2.33	0.33	0.44	α-Mg, C15, C36	[87]
AXM520	5.00	2.00	0.40	0.40	α-Mg, C36, Al_8Mn_5	[88]
AXM63011	6.10	3.20	0.11	0.52	α-Mg, C36, C14	[89]
AXM6305	6.00	3.20	0.46	0.52		
AXM4204	4.00	2.00	0.40	0.50	α-Mg, C36	[56]
AXM7303	6.90	3.30	0.30	0.47	α-Mg, C36, Al_8Mn_5	[59]

4.2 Optical and SEM micrographs

Figure 4.2(a to e) displays the optical images of the alloy and NCs with the corresponding grain size distribution. The continuous network of the dark $(Mg,Al)_2Ca$ (C36) phase was distributed along the interdendritic regions in the AXM520 alloy. The grain size of all the NCs was smaller

compared to the AXM520 allo, as estimated by the linear intercept method, summarized in Table 4.2. The grain size of the NCs reduced as the concentration of the SiC_{np} increased in the AXM520 alloy, and the same decreased by 36.8% in the NC3.0SiC. The grain refinement in the NCs was owing to the heterogeneous nucleation of α-Mg on the nanoparticles during solidification. The phenomenon of grain refinement in Mg alloy following the nanoparticle additions was reported previously as well [30].

Table 4.2 The calculated grain size, volume fraction, and fractal dimension of the C36 phase in the alloy and nanocomposites.

Alloy/ Nanocomposite	Grain size (µm)	Volume fraction of C36 phase (%)	Fractal dimension (D_f) of C36 phase
AXM520	52.5±12.1	17.41	1.58
NC0.5SiC	48.1±10.1	15.35	1.38
NC1.0SiC	43.2±11.1	13.82	1.29
NC2.0SiC	37.9±6.2	12.02	1.12
NC3.0SiC	33.2±6.3	11.51	1.10

The SEM image of the alloy is provided in Figure 4.3(a), and its enlarged view is displayed in Figure 4.3(b). Three different contrasts were observed in the micrograph. The dark grey and grey contrasts were identified as the α-Mg and C36 phases, respectively, and the bright spots correspond to the Al_8Mn_5 phase. The X-ray elemental mapping for Mg, Al, Ca, and Mn obtained from Figure 4.3(b) is displayed in Figure 4.3(c). The existence of Mg, Mg-Al-Ca, and Al-Mn-rich phases was confirmed in the micrograph of the AXM520 alloy. Another magnified view of the AXM520 alloy is presented in Figure 4.3(d), and the elemental analyses were performed in it. The EDS spectra from inside the grain (Spot 1) demonstrated the composition of Mg-2.6Al-0.3Ca (at.%), confirming α-Mg. The EDS spectra obtained from the lamellar phase (Spot 2) display the presence of Mg-28.5Al-14.9Ca (at.%), confirming the C36 phase. Li et al. [56] too reported a similar composition of C36 phase in the AXM alloy. Further, EDS spectra taken from the blocky phase (Spot 3) were identified as the Al_8Mn_5 phase with the composition of Mg-47.6Al-43.3Mn (at.%). A similar composition of the Al_8Mn_5 phase in the AXM alloys was stated by other researchers as well [59,88].

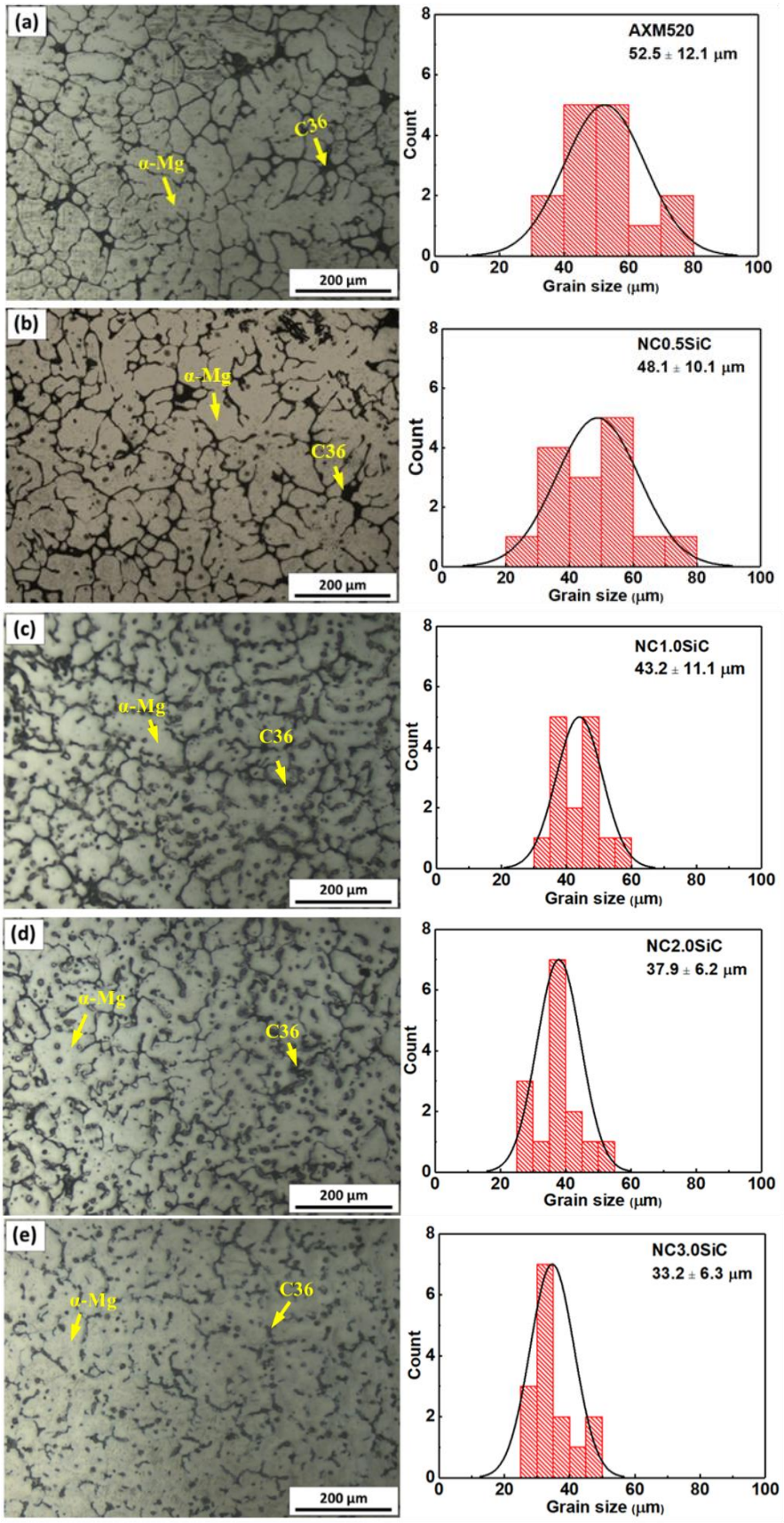

Figure 4.2 Optical micrographs with the corresponding grain size distribution of the (a) AXM520 alloy, (b) NC0.5SiC, (c) NC1.0SiC, (d) NC2.0SiC, and (e) NC3.0SiC nanocomposites.

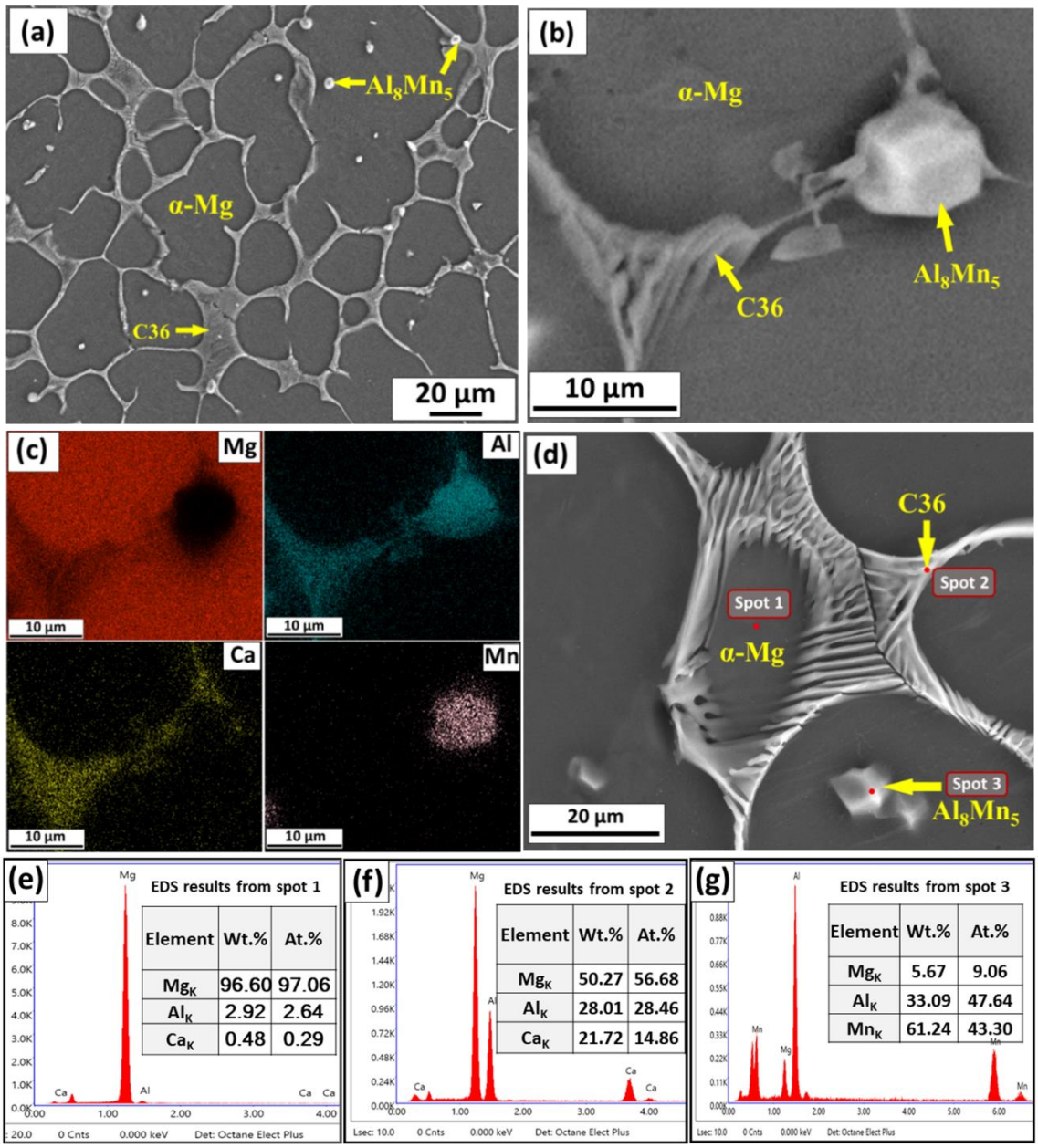

Figure 4.3 (a) SEM micrograph of as-cast AXM520 alloy; (b) a magnified view of 'a'; (c) X-ray elemental mapping of Mg, Al, Ca and Mn corresponding to 'b'; (d) another magnified view of 'a' indicating the regions of EDS analysis; EDS spectra taken from (e) spot 1 confirming α-Mg phase, (f) spot 2 confirming C36 phase, and (g) spot 3 confirming Al_8Mn_5 phase.

Figure 4.4(a to d) reveals the SEM micrographs of the NCs. The as-cast microstructures of all the NCs too consist of α-Mg phase, a eutectic of α-Mg and $(Mg,Al)_2Ca$ (C36) phases and a Al_8Mn_5 phase. Additionally, the SiC phase is also present in the NCs. The continuous network of the C36 phase in the NCs is fragmented and becomes discontinuous as the concentration of the SiC_{np} increases in the NCs. The amount of the C36 phase decreased with an increase in the concentration of the SiC_{np} in the NCs. The presence of the SiC_{np} in the matrix dissolved a fraction of the C36 phase and broke down its continuous network. The reason behind the reduction of the C36 phase has been discussed in section 4.3. A similar observation was also made by Huang et al. [93]. The β-$Mg_{17}Al_{12}$ phase in their investigation dissolved in α-Mg with increased concentration of the dispersed SiC and Al_2O_3 phases. Moheimani et al. [94] also observed that incorporating the AIN nanoparticles in EV31 alloy reduced the amount of secondary Mg_3RE in the nanocomposite. Ganguly and Mondal [30] also concluded that the extent of β-$Mg_{17}Al_{12}$ phase diminished with increase in SiC nanoparticles concentration in the AZ91-Ca-Sb-alloy-based nanocomposites.

4.3 Fractal analysis of SEM micrographs

The fractal analyses were carried out to study the connectivity of the C36 phase of the as-cast alloy and NCs. The microstructures of the AXM520, NC0.5SiC, and NC3.0SiC at a fixed magnification are presented in Figure 4.5(a to c). The maximum connectivity of the C36 phase was in the AXM520 alloy. The connectivity of the C36 phase decreased as the concentration of the nanoparticles increased in the NCs. Furthermore, the network of the C36 phase surrounding the α-Mg phase disappeared gradually with the increase in the SiC_{np} content, and it was the lowest in the NC3.0SiC, as shown in Figure 4.5(c). For better clarity, the connectivity of the secondary phase network was further quantified in terms of fractal dimension (D_f) and was plotted in Figure 4.5(d to f). The results show that the slopes of the curves decreased as the concentration of the nanoparticles increased in the NCs. The slope was the maximum (i.e., 1.58) corresponding to AXM520 alloy, and the same was the minimum (i.e., 1.10) in NC3.0SiC. The estimated content of the C36 phase in both the alloy and NCs, and corresponding fractal dimensions are presented in Table 4.2. For a well-developed secondary phase network, the value of D_f should be two, whereas it is one for the fragmented network [35]. Based on the values of D_f presented in Table 4.2, it is evident that the connectivity of the grain boundary phase decreased as the concentration of the SiC_{np} increased in the NCs.

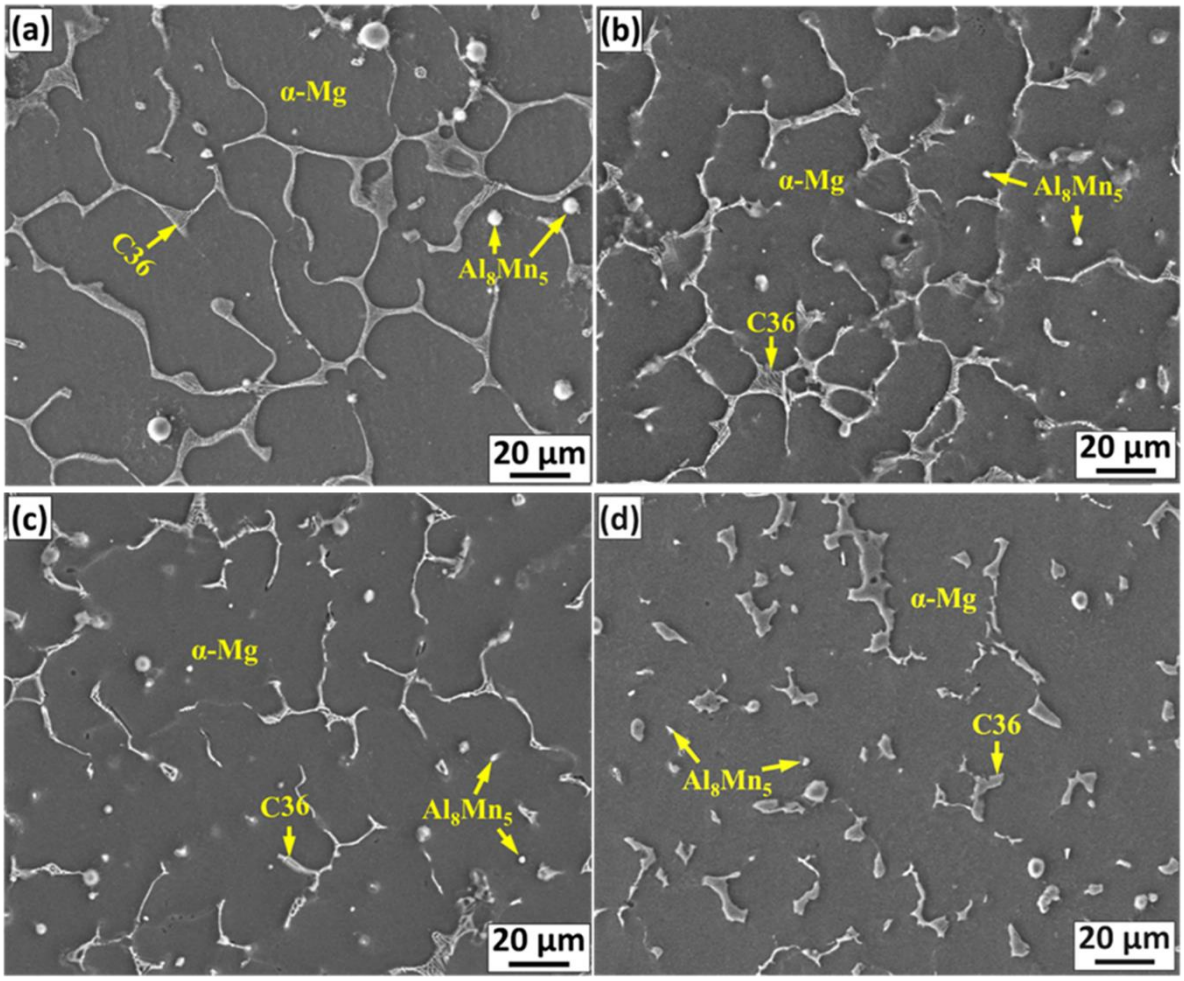

Figure 4.4 SEM micrographs of the as-cast (a) NC0.5SiC, (b) NC1.0SiC, (c) NC2.0SiC, and (d) NC3.0SiC nanocomposites.

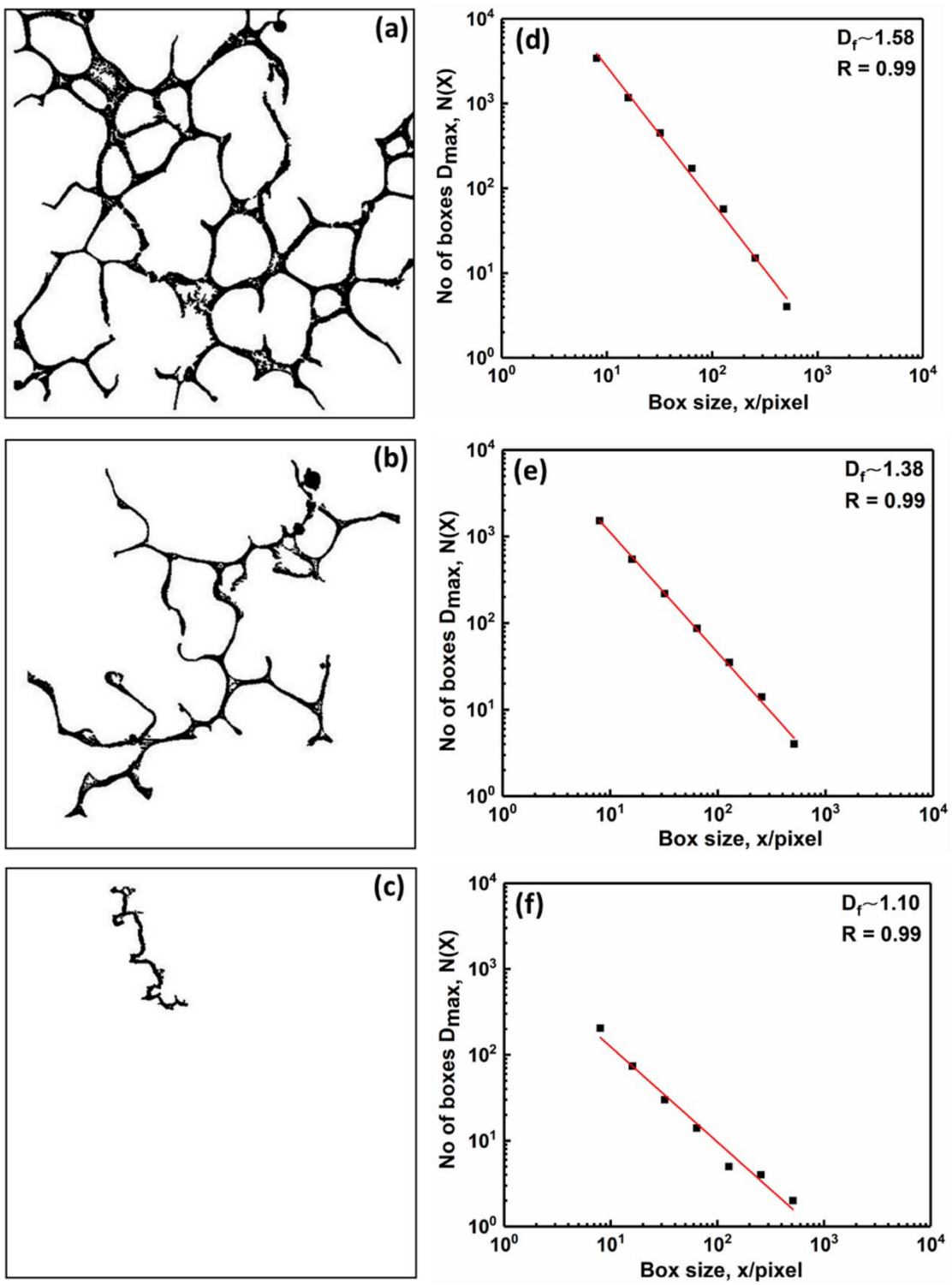

Figure 4.5 Fractal analyses of the (a) AXM520, (b) NC0.5SiC, and (c) NC3.0SiC exhibiting the maximum connected C36 phase extracted from the respective binary SEM images; and (d) to (f) exhibit the fractal dimension (D_f) plots obtained from the respective images fractal dimension (D_f) plots obtained from the respective images from 'a' to 'c'.

During solidification, the alloying elements Al and Ca were directed towards the boundaries between the solid and liquid phases, and accordingly, the secondary phase formation took place along the grain boundaries of the alloy [56]. Suzuki et al. [16] reported that the liquid (L) → α-Mg + $(Mg,Al)_2Ca$ (C36) reaction took place at 807 K and a Ca/Al fraction of 0.52. They also mentioned that for the Ca/Al fraction beyond 0.52, the eutectic reaction: liquid (L) → α-Mg + Mg_2Ca (C14) + C36 took place. The Ca/Al fraction in the present investigation is restricted below 0.50, and accordingly, the formation of the C14 was not observed in the AXM520 alloy. The role of the nanoparticles during solidification, i.e., the occurrence of the α-Mg as well as secondary C36 phases in the AXM520 alloy, can be understood from the reported literature on the nanocomposites. Xu et al. [95] in their work revealed that the nanoparticles were engulfed by the growing dendrites or pushed towards the liquid phase during solidification. Chen et al. [90] showed that the nanoparticles acted as a physical barrier during the growth of the solid phase. Wang et al. [91] showed that the presence of nanoparticles during solidification greatly impeded the solute rejection from the solid phase. Guo et al. [96] too showed that as the local concentration of nanoparticles increased in the liquid melt, the diffusion of the major solute particles were hindered during solidification. They also mentioned that the viscosity of the liquid melt increased in the presence of nanoparticles, resulting in a decrease in the solute diffusion process. Thus, during the solidification of the NCs in the present investigation, one or more phenomena might have occurred, resulting in the morphological change and reduction in the fraction of the secondary C36 phase in the NCs. However, it is impossible to identify and isolate the individual mechanism responsible for the decrease of amount of the C36 phase. This requires a comprehensive examination of the solidification characteristics of the alloy and NCs, which is not within the scope of the current study.

4.4 TEM analysis

Figure 4.6(a) shows the TEM bright-field (BF) image of the intermetallic phase in the AXM520 alloy. The image taken from the eutectic region exhibits the presence of the alternate layers of the α-Mg phase with bright contrast and an unknown phase with dark contrast. The eutectic was distributed across several microns along the width. The SAED pattern acquired from the dark portion of the eutectic shown in Figure 4.6(b) confirms the $(Mg,Al)_2Ca$ phase with a double hexagonal crystallographic structure (C36). Thus, the microstructure of the AXM520 alloy comprises α-Mg grains as well as the eutectic of α-Mg and $(Mg,Al)_2Ca$ (C36) phases

along grain boundaries and triple points. The careful analysis of the SAED pattern confirms the following orientation relationships between α-Mg and C36 phases.

$$(0001)_{\alpha\text{-Mg}} \,||\, (0001)_{C36}\ ,\ [10\bar{1}0]_{\alpha\text{-Mg}} \,||\, [11\bar{2}0]_{C36}$$

A similar orientation relationship was reported by Luo et al. in their work on Mg-5Al-3Ca alloy [97]. The lattice parameters of the α-Mg and C36 phases were also calculated from the SAED pattern. The lattice parameter value for α-Mg was approximately a = 3.19 Å and c = 5.23 Å, and the same for the C36 phase was a = 5.92 Å and c = 9.87 Å. Figure 4.6(c) shows the BF micrograph acquired from the intermetallic phase observed in the NC3.0SiC, and the analysis of its SAED pattern in Figure 4.6(d) confirms existence of C36 phase in the α-Mg matrix of the NCs as well. The precipitate has an irregular shape with an average width of 1.58±0.6 µm. The BF image and its SAED pattern taken from the matrix of the NC2.0SiC shown in Figure 4.6(e and f), exhibits an almost homogeneous distribution of SiC_{np} in α-Mg matrix. Figure 4.6(g) reveals the agglomeration of the nanoparticles in the matrix of the NC3.0SiC. The corresponding SAED pattern shown in Figure 4.6(h) with ring-like appearance confirms the presence of the SiC phase, and the dot pattern was from the primary Mg phase. The high-resolution (HR)-TEM image of the SiC_{np} present in the α-Mg phase is shown in Figure 4.7(a). The First Fourier Transformation (FFT) of Figure 4.7(a) confirms that the observed fringes correspond to the (002) plane of the SiC phase, is shown in Figure 4.7(b). The SiC_{np} present in the grain interior resulted from the engulfment of the SiC_{np} phase by the solid-liquid interface during the solidification of the melt. Figure 4.7(c and d) exhibits a TEM-BF micrograph of the grain boundary region, and the corresponding SAED with ring pattern. The analysis of the SAED pattern confirms the coexistence of the C36 and SiC_{np} phases at the grain boundary region of NC3.0SiC nanocomposites. Fractions of the added SiC_{np} were pushed along the solid-liquid interface and decorated along the boundaries of the C36 phase.

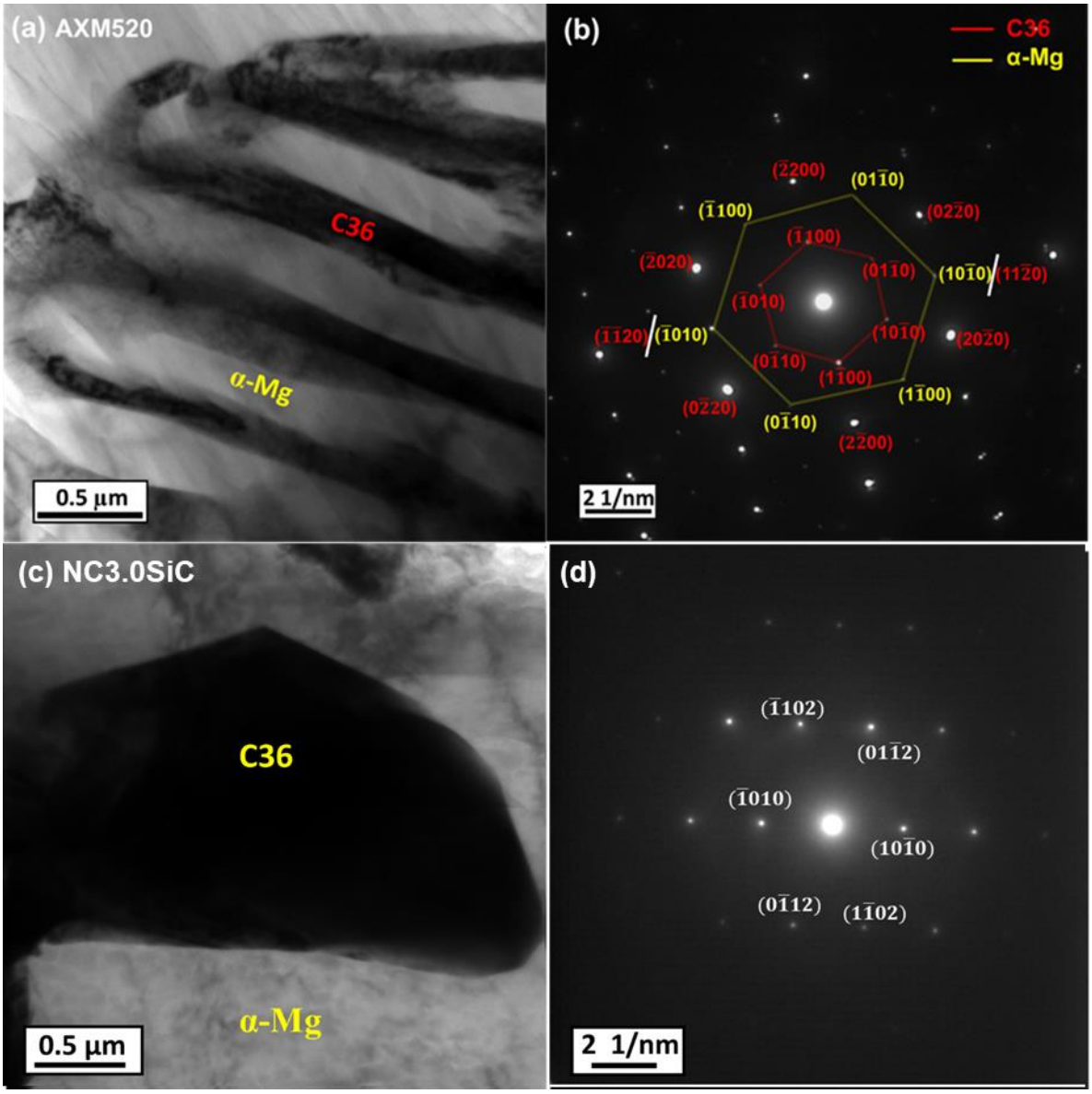

Figure continued to next page

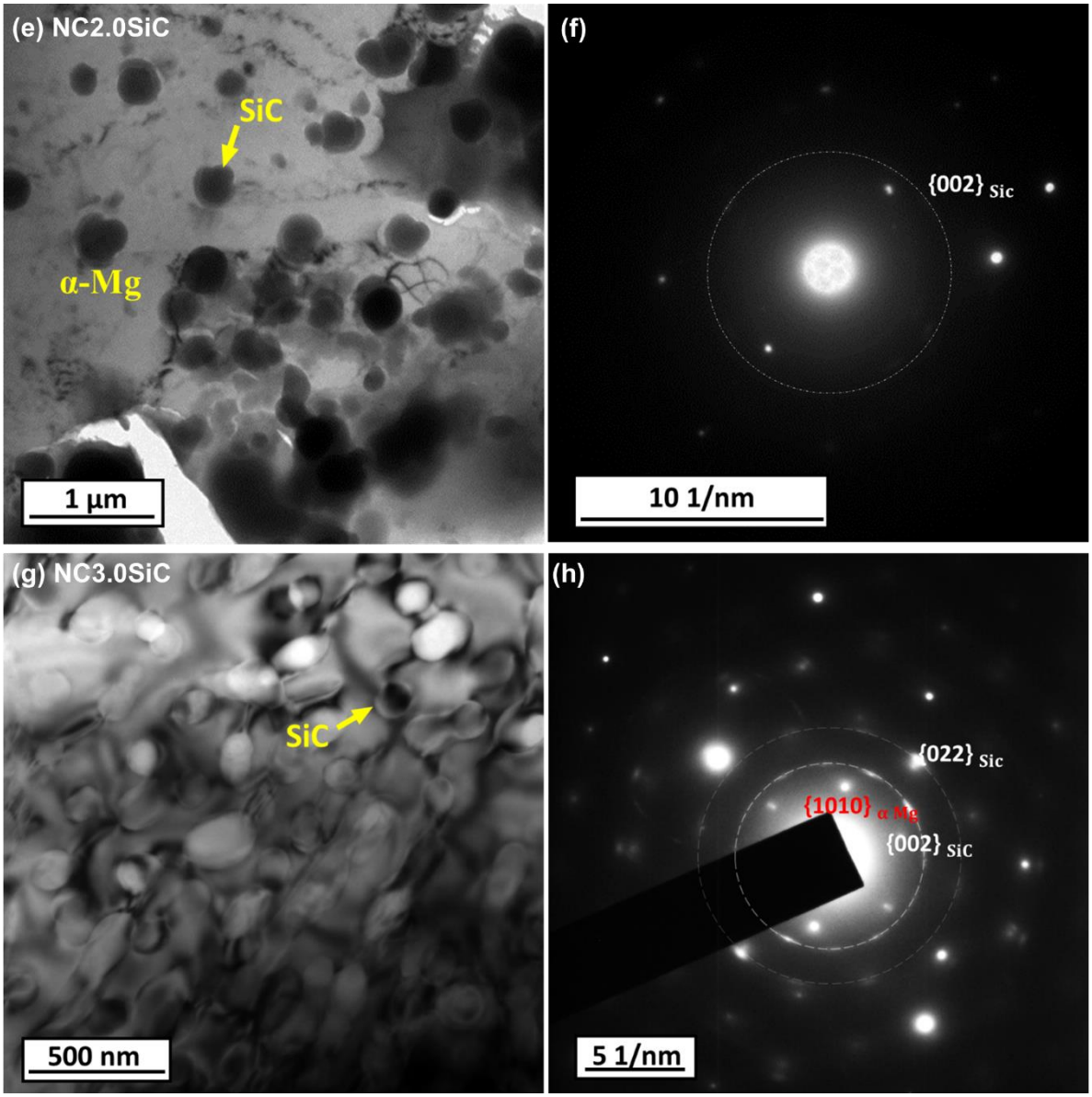

Figure 4.6 (a) TEM BF image taken from the C36 phase of AXM520 alloy, and (b) SAED pattern corresponding to 'a' with beam direction B = [0001]; (c) TEM BF image taken from the C36 phase of NC3.0SiC, and (d) SAED pattern corresponding to 'c' with beam direction B =[$\bar{2}4\bar{2}3$]; (e) TEM BF image taken from the matrix of NC2.0SiC exhibiting the distribution of SiC nanoparticles, and (f) SAED pattern corresponding to 'e'; (g) TEM BF image taken from the matrix of NC3.0SiC exhibiting the agglomeration of SiC nanoparticles, and (h) SAED pattern corresponding to 'g'.

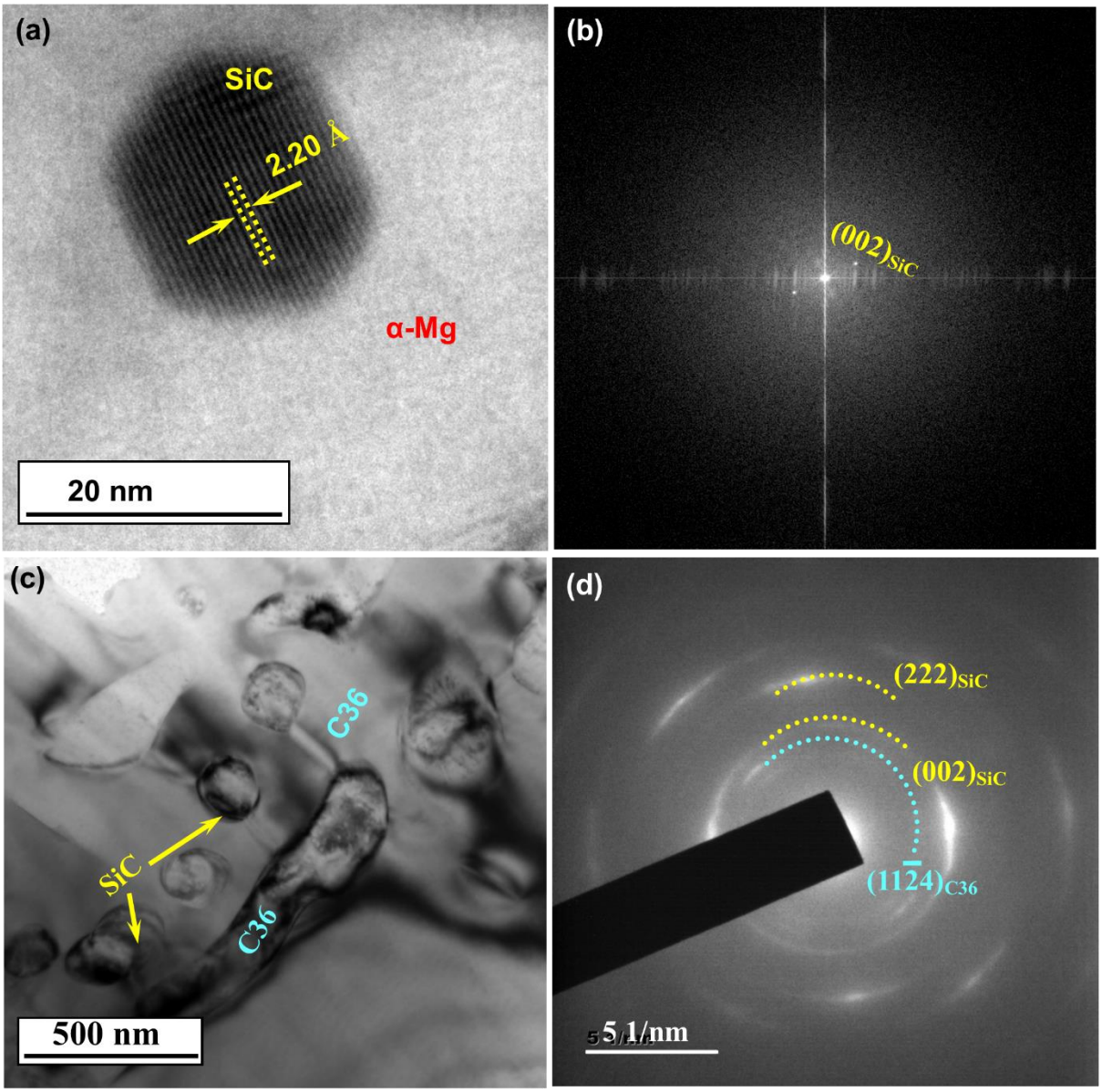

Figure 4.7 (a) HR-TEM image of the SiC_{np} present in α-Mg of NC3.0SiC; (b) FFT corresponding to 'a'; (c) distribution of SiC_{np} close to the C36 phase at the intergranular region of the NC3.0SiC; and (d) SAED pattern corresponding to 'c'

4.5 Summary of chapter 4

In this chapter, the detailed microstructural characterization of the squeeze-cast Mg-5.0Al-2.0Ca-0.3Mn (AXM520) alloy and its nanocomposites dispersed with 0.5, 1.0, 2.0, and 3.0 (wt.%) of SiC_{np} has been presented. The nanocomposites (NCs) were abbreviated as NC0.5SiC, NC1.0SiC, NC2.0SiC and NC3.0SiC. The major findings from the current chapter are summarized below.

i. The microstructures of AXM520 alloy and NCs consist of a primary solid solution (α-Mg), a eutectic of α-Mg and $(Mg,Al)_2Ca$ (C36) phases, and an Al_8Mn_5 phase. Additionally, the SiC phase was also present in the NCs.

ii. The grain size of the NCs reduced as the concentration of the SiC_{np} increased in the AXM520 alloy, and the same decreased by 36.8% in the NC3.0SiC.

iii. The C36 phase formed a continuous network in the AXM520 alloy. However, the same in the NCs was fragmented and became discontinuous with the increase in the fraction of the SiC_{np}. Thus, the C36 phase was the most fragmented in the NC3.0SiC.

iv. The α-Mg and C36 phase present in the AXM520 alloy exhibited an orientation relationship of $(0001)_{\alpha\text{-Mg}} \,||\, (0001)_{C36}$, $[10\bar{1}0]_{\alpha\text{-Mg}} \,||\, [11\bar{2}0]_{C36.}$ The lattice parameter values for the α-Mg and C36 phases were found to be a = 3.19 Å, c = 5.23 Å, and a = 5.92 Å, c = 9.87 Å, respectively.

Chapter 5

Tensile and Compressive Behavior

In the present chapter, the ambient temperature tensile and compressive properties of the AXM520 alloy and NCs have been evaluated. Detailed analyses of the strain-hardening response and fracture surfaces of the tested specimens are carried out. The dislocations in the tested specimens have been characterized using TEM. A summary of the tensile and compressive behavior is presented at the end of this chapter.

5.1 Evaluation of mechanical properties

5.1.1 Tensile Yield Strength, Ultimate Tensile Strength, and % Elongation

Figure 5.1(a) shows the typical engineering stress vs. engineering strain curves obtained at ambient temperature from the AXM520 alloy and the NCs. The tensile properties, i.e., Yield Strength (YS), Ultimate Tensile Strength (UTS), and %Elongation (%El) calculated from Figure 5.1(a) are presented in Figure 5.1(b). The magnitudes of YS, UTS, and %El of the AXM520 alloy were 80.4±8.2 MPa, 111.28±7.1 MPa, and 1.03±0.03%, respectively. All the NCs exhibited superior tensile properties than the AXM520 alloy. The NC with 0.5 (wt.%) SiC_{np} (i.e., NC0.5SiC) exhibited the lowest YS, UTS, and %El among the NCs. The NC2.0SiC exhibited the best tensile properties among the nanocomposites employed in the current study. The YS, UTS, and %El of the NC2.0SiC enhanced by 37.2, 69.8, and 200.9%, respectively, compared to the AXM520 alloy. Unfortunately, with further increase in the nanoparticle's concentration in the nanocomposites, i.e., in the NC3.0SiC, there was a marginal increase in the YS with a deterioration in the UTS and %El compared to the NC1.0SiC and NC2.0SiC. Thus, the YS of the NCs improved gradually with the increase in the SiC_{np} concentration up to 3.0 (wt.%). However, the UTS and %El of the nanocomposite declined with the addition of more than 2.0 (wt.%) SiC_{np} to the AXM520 alloy. Goh et al. [71] too reported an improvement in the YS and UTS of pure Mg with additions of Y_2O_3 nanoparticles up to 2.0 vol.% without deteriorating its ductility much. The low values of %El of the Mg-Al-Ca (AX) and Mg-Al-Ca-Mn (AXM) alloys were also reported previously. The presence of the brittle A12, C36, and C14 phases was responsible for the low elongation of the alloys. Sanyal et al. [35] mentioned that the hardness and modulus mismatch between the matrix and Ca-rich phases introduced a large amount of decohesion in the AXM alloy. The network of Ca-rich phase in their investigation facilitated crack propagation during fracture. Thus, the discontinuous network of

the C36 phase in the NCs significantly inhibited crack propagation, leading to their improved elongation compared to the AXM520 alloy. However, as the concentration of the SiC_{np} increased to 3.0 (wt.%) in the NC3.0SiC, the agglomeration of the nanoparticles increased, resulting in an inferior %El of the NC3.0SiC.

5.1.2 Compressive Yield Strength and Ultimate Compressive Strength

The representative stress-strain plot of the AXM520 alloy, as well as NCs obtained from the uniaxial compressive test at ambient temperature, is shown in Figure 5.1(c). The nature of the plots is in good agreement with the previously reported compressive plots on Mg-based alloys and composites [72,76,78]. The compression properties evaluated from Figure 5.1(c) are presented in Figure 5.1(d). All the NCs exhibited superior compressive strength than the AXM520 alloy. Among the NCs, the NC0.5SiC demonstrated the minimum CYS and UCS. The NC2.0SiC exhibited the best compressive strength among the NCs. The CYS and UCS of the NC2.0SiC enhanced by 23.7 and 53.9% than the AXM520 alloy. Unfortunately, with further increase in the nanoparticles content in the NCs, i.e., in the NC3.0SiC, there is a marginal increase in the CYS with a deterioration in the UCS than the NC2.0SiC. Thus, the CYS of the NCs improved gradually with the increase in the SiC_{np} concentration up to 3.0 (wt.%). However, the UCS declined with the addition of more than 2.0 (wt.%) SiC_{np} to the AXM520 alloy due to the significant agglomeration of the nanoparticles, which weakened the strain-hardening response of the NCs. Accordingly, the UCS value of the NC3.0SiC decreased.

5.1.3 Strain-hardening responses

Hollomon equation [98] relates the true stress (σ) with the true plastic strain (ε) from the point of yielding to UTS through the following equation.

$$\sigma = k\epsilon^n \qquad \text{Equation 5.1}$$

where n and k are the strain-hardening exponent (SHE) and strength coefficient, respectively. The ability of a material to undergo strain-hardening is quantified by the parameter SHE (n). A plot of true stress against true strain in a log-log scale up to UTS results in a straight line. The gradient of the line is SHE (n). Figure 5.2(a) shows the $\log(\sigma_{True})$ vs. $\log(\varepsilon_{true})$ plot for the AXM520 alloy and NCs. The AXM520 alloy exhibits a 'n' value of 0.31, whereas the same

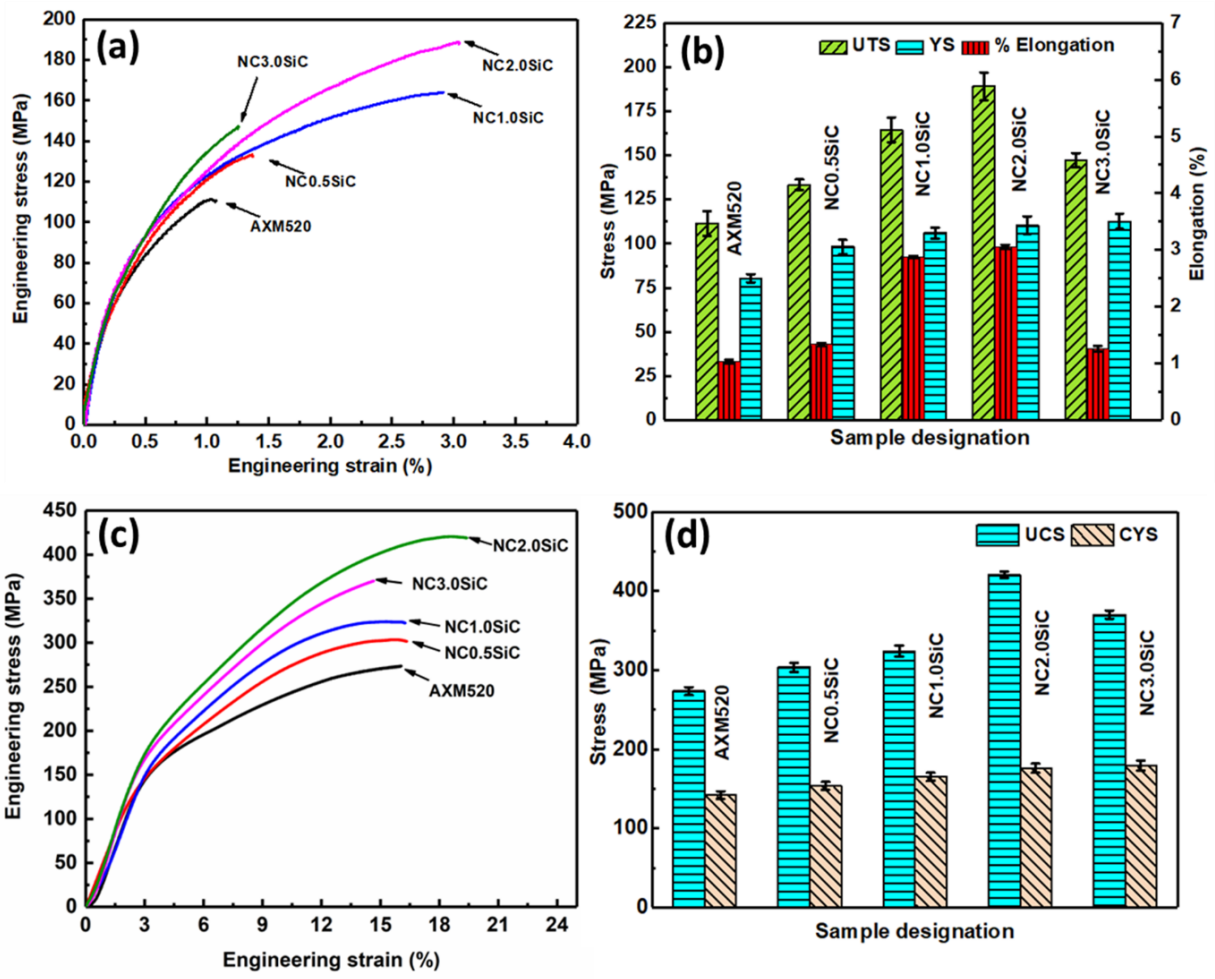

Figure 5.1 (a) Typical engineering stress-strain curves obtained from tensile tests of the AXM520 alloy and NCs, and (b) tensile properties calculated from 'a'; (c) typical engineering stress-strain curves obtained from compression tests of the AXM520 alloy and NCs, and (d) compressive properties calculated from 'c'.

ranges from 0.33 to 0.38 for all the NCs. The 'n' values of the NCs gradually increased as the SiC_{np} concentration increased in the NCs. Among the NCs, the NC3.0SiC displayed the maximum 'n' value, i.e., 0.38. Ganguly et al. [81] too reported that the 'n' values increased with the increase in the SiC concentration in the AZ91-Ca-Sb-based nanocomposites. The same trend was also observed for the 'n' values calculated from the compression tests, as shown in Figure 5.2(b). The AXM520 alloy has a 'n' value of 0.30, whereas all the NCs have 'n' values from 0.31 to 0.37.

During plastic deformation, a material undergoes strain-hardening by virtue of its own plastic deformation. In strain-hardening, the stress value of a material is enhanced with the progress of the deformation, i.e., strain. The phenomenon is attributed to the interactions that took place among the dislocations inside the material. The strain-hardening rate (SHR) is related to the true stress (σ) with the true plastic strain (ε) by $\frac{d\sigma}{d\varepsilon}$. Thus, the SHR is the gradient of the true-stress-strain plot in the uniform plastic deformation region. In real life, a material continues to strain-harden until it fractures. However, the geometrical softening overcomes it at the maximum load, i.e., UTS. Beyond the UTS, the geometrical softening dominates over the strain-hardening rate, leading to the material's failure under tension [64]. Figure 5.2(c) shows the variation of SHR against the true plastic strain during the tensile tests for all the materials employed. The SHR decreased linearly with the progress of deformation (i.e., strain) for both the alloy and NCs. Initially, the SHR was higher, and the same declined continuously, leading to the minimum value at the UTS for the plastic strain range considered, as expected. Further, all the NCs exhibited a higher SHR of ~8000-10000 MPa than ~7600 MPa of the AXM520 alloy. The SHR estimated from the compression test for the alloy, and NCs exhibited the same trend, as shown in Figure 5.2(d). A SHR rate of ~7000 MPa was obtained for the AXM520 alloy, whereas all the NCs exhibited relatively higher values of SHR of ~9500 to 10500 MPa. The strain rate, grain size, texture, temperature, twinning, and alloying additions alter the SHR of Mg-based alloys and nanocomposites [64,99-101]. The superior SHR exhibited by the NCs in the current study was probably governed by the potential grain refinement achieved from the nanoparticles and dislocations generated owing to CTE mismatch. A detailed explanation for the improved SHR with a reduction in grain size is available elsewhere [64,98]. Ganguly et al. [81] reported an enhanced SHR following the SiC nanoparticles dispersion in the AZ91-Ca-Sb-based alloy. Lee and Kim [102] too stated a similar observation in the extruded Mg-Carbon-

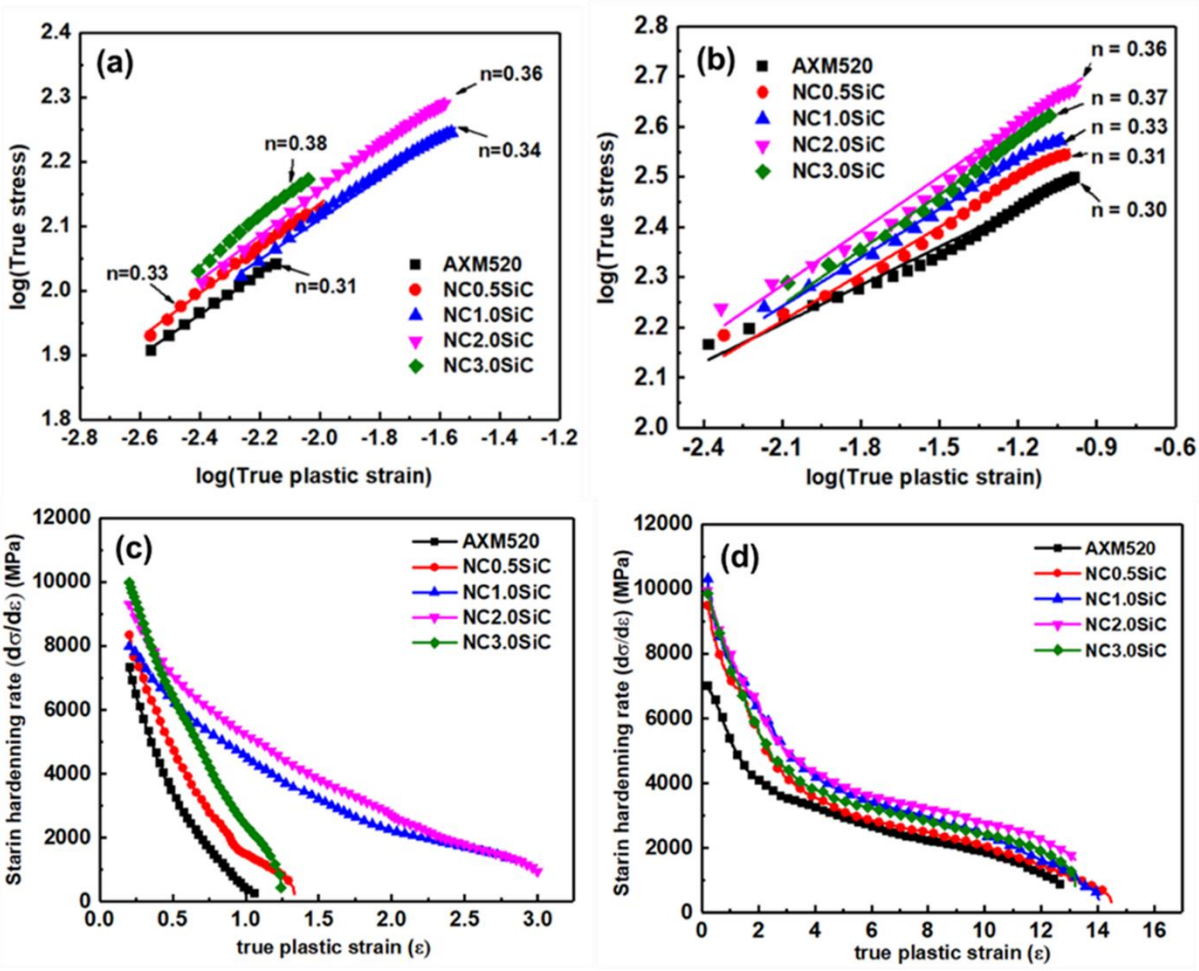

Figure 5.2 Log-log plots of true stress-strain curves for the alloy and NCs displaying the strain hardening exponent (n) calculated from the tensile tests (a) and compression tests (b); variation of strain-hardening rate (dσ/dε) vs. true plastic strain (ε) for the alloy and NCs corresponding to the tensile tests (c), and compression tests (d).

based nanocomposite. A similar strain-hardening response of the extruded Mg-SiC-based composite was observed by Manoharan et al. [103]. Korayem et al. [104] too concluded an increased SHR of pure Mg- and AZ31 alloy-based nanocomposites with the increase of Al_2O_3 nanoparticles content.

5.2 Theoretical prediction of strength and analyses of strengthening mechanisms

The combined effects of strengthening resulting from Hall-Petch, Orowan, CTE mismatch, and load-partitioning contributed to the superior tensile behavior of the AXM520 alloy-based NCs. The grain size of the NCs reduced considerably with an increase in the concentration of the SiC_{np} in the NCs. The contribution to Hall-Petch ($\Delta\sigma_{Hall-Petch}$) strengthening resulting from grain size reduction is predicted as follows [105]:

$$\Delta\sigma_{Hall-Petch} = K{d_m}^{-0.5} \quad \text{Equation 5.2}$$

Here K is a constant related to the material, and d_m is the matrix grain size. In the Orowan mechanism, a dislocation loop is formed around the nanoparticle, resisting the successive dislocation motion and accelerated strain-hardening. In addition, the increased volume fraction of the nanoparticles reduced inter-particle distance between two nanoparticles, restricting dislocation motion further during deformation. The contribution from Orowan strengthening ($\Delta\sigma_{Orowan}$) is estimated as follows [106]:

$$\Delta\sigma_{Orowan} = \frac{0.13G_m b}{\lambda}\ln\frac{d_p}{2b} \quad \text{Equation 5.3}$$

$$\lambda \approx d_p\left[\left(\frac{1}{2V_p}\right)^{\frac{1}{3}} - 1\right] \quad \text{Equation 5.4}$$

where G_m is the modulus in shear of the matrix, b denotes the burger vector, d_p is the diameter of the nanoparticle, λ is the spacing between the nanoparticles, and V_p is the volume fraction of the nanoparticles. The CTE of Mg is significantly different from that of SiC. The dislocation density increased from the difference in CTE values between the AXM520 alloy and SiC_{np}, contributed to the strengthening effect as follows [106]:

$$\Delta\sigma_{CTE} = 1.25G_m b\sqrt{\frac{12\Delta\alpha\Delta T V_p}{bd_p(1-V_p)}} \quad \text{Equation 5.5}$$

where Δα is the difference in CTE values, and ΔT signifies the difference in the processing temperature to the test temperature. The nanoparticles were assumed equiaxed for estimating

the enhancement in YS resulting from the load transfer effect between the matrix alloy and SiC_{np} reinforcement is provided as [106]:

$$\Delta\sigma_l = 0.5V_p\sigma_{o\,[Matrix]} \quad \text{Equation 5.6}$$

The contribution from the individual strengthening mechanism was calculated for all the NCs employing Eq. 5.2 to 5.6, along with the data summarised in Table 5.1. The results obtained are shown in Figure 5.3(a and b). The strengthening from CTE mismatch contributed the most to the overall strengthening of all the NCs. The contributions in strengthening due to the difference in CTE values, Hall-Petch and Orowan increased by 146.0, 18.1, and 121.2 % with the increase in nanoparticle content from 0.5 to 3.0 (wt.%) in the NCs.

Table 5.1 A summary of the parameters used to calculate the strength of the nanocomposites.

Parameters	Value
Hall Petch slope (k_y)	167.2 MPa√μm
CTE (α_{matrix}) of AXM520 alloy	30.40×10^{-6} K^{-1}
CTE (α_{SiC})of SiC_{np}	4.96×10^{-6} K^{-1}
Δα	$\alpha_m - \alpha_{SiC}$
Burgers vector (b)	0.32 nm
Nanoparticle diameter (d_p)	60 nm
Shear modulus (G_m)	17307 MPa
$T_{process}$	250 °C
Volume fraction of nanoparticles V_p	0.0029, 0.0058, 0.0116, and 0.0174

The values of YS of all the NCs were further estimated theoretically employing the 'Summation' [34], 'Modified Clyne' [105], and 'Zhang and Chen' [107] models as stated below, and the results are compared with the experimentally obtained values in Figure 5.3(c).

$$\sigma_{Summation} = \sigma_{0\,[Matrix]} + \Delta\sigma_{Hall-Petch} + \Delta\sigma_{Orowan} + \Delta\sigma_{CTE} + \Delta\sigma_l \quad \text{Equation 5. 7}$$

$$\sigma_{Modified\ Clyne} = \sigma_{0\,[Matrix]} + \sqrt{(\Delta\sigma_{Hall-Petch})^2 + (\Delta\sigma_{Orowan})^2 + (\Delta\sigma_{CTE})^2 + (\Delta\sigma_l)^2} \quad \text{Equation 5. 8}$$

$$\sigma_{Zhang\ and\ Chen} = (1 + 0.5V_p)\left(\sigma_{0\,[Matrix]} + \sigma_{orowan} + \sigma_{CTE} + \frac{\sigma_{orowan} \times \sigma_{CTE}}{\sigma_{0\,[Matrix]}}\right) \quad \text{Equation 5.9}$$

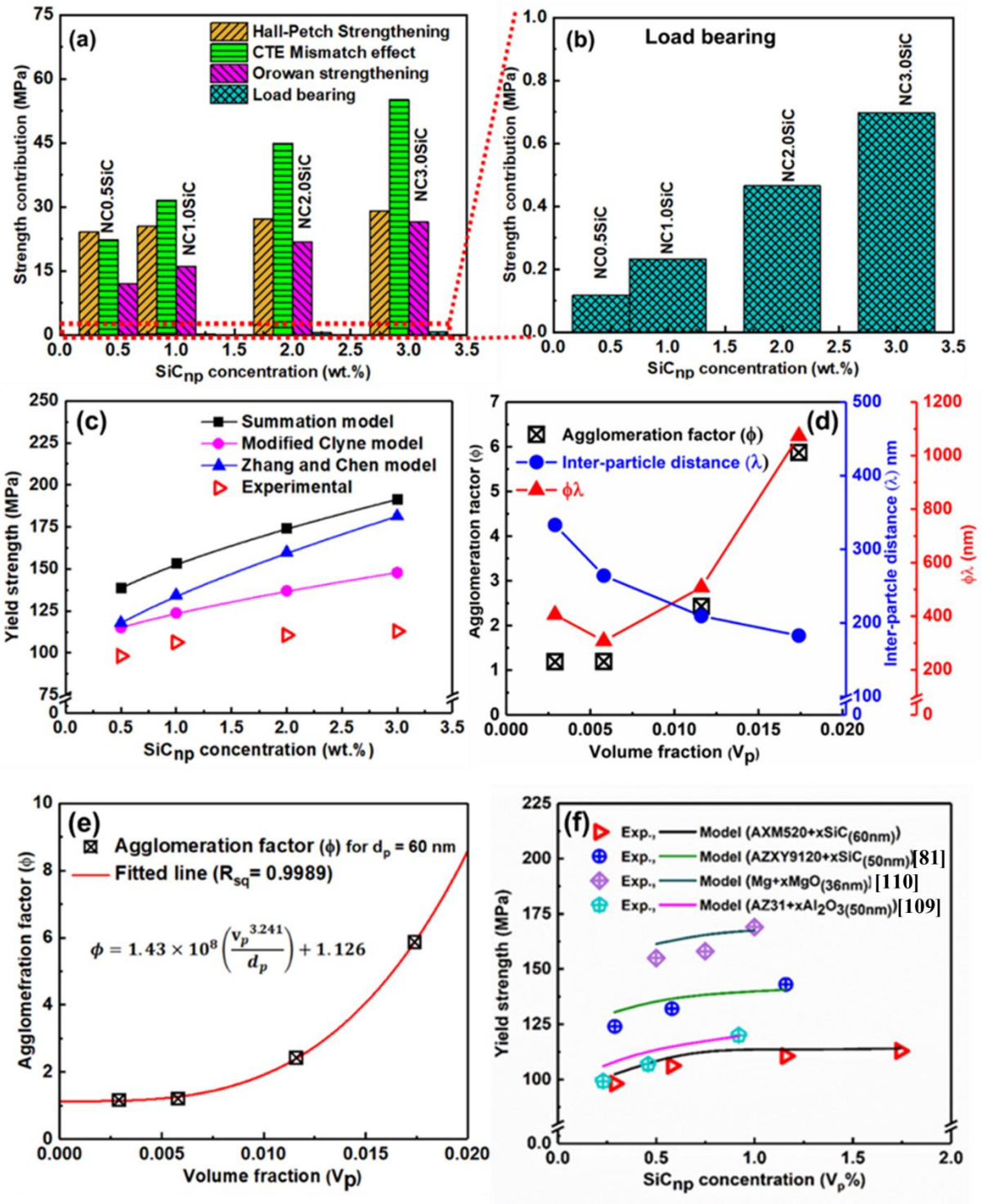

Figure 5.3 (a) Contribution of different strengthening mechanisms to the tensile yield strength (TYS) of the NCs;(b) magnified view of 'a' depicting the load-bearing effect; (c) comparison of the calculated and experimentally determined values of TYS of the NCs; (d) variation of agglomeration factor (φ), inter-particle distance (λ) and 'φλ' with volume fraction (V_p) of the nanoparticles; (e) agglomeration factor (φ) vs. V_p of the nanoparticles with curve fitting; (f) comparison of the experimental and predicted values of TYS.

All the models overestimated the YS of the NCs. The models assumed a homogeneous distribution of nanoparticles. However, the nanoparticles were agglomerated in the NCs during solidification due to their higher surface-to-volume ratio. Thus, the agglomeration of the nanoparticles affected the Orowan strengthening by increasing inter-particle distance (λ). Therefore, an agglomeration factor (ϕ) was introduced in the Orowan equation (Eq. 5.3) to assess the degree of agglomeration in the NCs.

$$\Delta\sigma_{Orowan} = \frac{0.13G_m b}{\phi\lambda}\ln\frac{d_p}{2b} \qquad \text{Equation 5.10}$$

Mallmann et al. [108] reported that the cluster of nanoparticles contributed significantly to $\Delta\sigma_{CTE}$, whereas the contribution from the individual nanoparticle was negligible. They also concluded that the experimental value of $\Delta\sigma_{CTE}$ in the nanocomposite was half of the $\Delta\sigma_{CTE}$ value calculated from Eq. 5.5. Therefore, a value of $0.5\Delta\sigma_{CTE}$ is considered instead of $\Delta\sigma_{CTE}$. Thus, the 'Zhang and Chen' model is modified as follows:

$$\sigma_{Zhang-Chen\,mod} = \left(1 + 0.5V_p\right)\left(\sigma_{o\,[Matrix]} + \frac{\sigma_{Orowan}}{\phi} + \frac{\sigma_{CTE}}{2} + \frac{\sigma_{orowan} \times \sigma_{CTE}}{2\phi\sigma_{o\,[Matrix]}}\right) \qquad \text{Equation 5.11}$$

The values of agglomeration factor (ϕ) from Eq. 5.11 and inter-particle distance (λ) from Eq. 5.4 were evaluated for all the NCs, and the same are shown in Figure 5.3(d). The ϕ values remain almost constant up to 0.0058 V_p and then increase sharply, whereas the inter-particle distance (λ) decreases continuously with the increase in V_p, as expected. Thus, the agglomeration of the nanoparticles in the NCs was not significant up to 0.0058 vol. fraction of the SiC_{np} (i.e., NC1.0SiC). Beyond this, the same increases significantly, leading to the highest value in the NC3.0SiC. The parameter $\phi \times \lambda$ indicates the inter-particle distance between two agglomerates, and following an initial decrease, its value gradually increases, as ϕ was dominating over λ. The agglomeration factor (ϕ) is related to the volume fraction (V_p) and average diameter (d_p) of the nanoparticle as follows.

$$\phi \propto \frac{(V_P)^n}{d_P} \qquad \text{Equation 5.12}$$

The exponent n is considered as ϕ increased significantly with the increase in the nanoparticle content. Figure 5.3(e) displays the results of the fitting of Eq. 5.12, and the expression of ϕ is obtained as

$$\phi = \frac{C_1 \times (V_p)^n}{d_p} + C_2 \qquad \text{Equation 5.13}$$

where C_1 [=1.430 × 10^8 nm] and C_2 [=1.126] are the fitting constants. The value of n is derived as 3.241. In the present investigation, the average diameter of the nanoparticles, d_p, is 60 nm. The evaluated value of ϕ from Eq. 5.13 was utilized to calculate the YS of all the NCs using the modified Zhang and Chan model proposed in Eq. 5.11. The theoretically calculated YS values of all the NCs are as per the experimental values, as shown in Figure 5.3(f). The equation was also employed to predict the YS of some pure Mg and Mg alloy-based nanocomposites reported in the literature [81,109,110]. The predicted values were pretty close to that of the experimental data, as depicted in Figure 5.3(f).

5.3 Observation of dislocations in post-tensile samples

Figure 5.4 (a to d) shows the dislocation arrangement inside the α-Mg grain of the tensile-tested AXM520 alloy. The TEM bright-field image in Figure 5.4(a) exhibits the dense dislocation forest inside α-Mg grain in the AXM520 alloy. The measured 'd' spacing is approximately 2.49 Å, which corresponds to $[10\bar{1}1]$ '**g**' vector, as shown in Figure 5.4(b). Further, the dark-field images corresponding to '**g**' and '**-g**' vectors are shown in Figure 5.4(c and d). Both images exhibit the **g.b** = 0 invisibility criteria and reveal the dense dislocation forest in the deformed region. The presence of dislocation forest in the grain interior of the primary phase was reported by other researchers as well [111].

The deformed tensile tested samples of the AXM520 alloy and NC2.0SiC were further examined under TEM, and the micrographs are displayed in Figure 5.5(a to d). The TEM BF image and its corresponding two-beam SAED pattern taken from the alloy in Figure 5.5(a and b) reveal the piled-up of numerous dislocations around the C36 phase. The presence of the C36 phase interacted with the dislocations and inhibited their motion, giving rise to the higher dislocation density. Wang et al. too reported an analogous dislocation network around the β-$Mg_{17}Al_{12}$ as well as Al_8Mn_5 phases in the stressed AZ91 and AM50 alloys [112,113]. The BF--TEM image and its corresponding SAED pattern taken from the NC2.0SiC in Figure 5.5(c and d) exhibit that the nanoparticles restricted the dislocation motion as well, and thus there was an additional hindrance to the dislocation motion in the nanocomposites. The consequences of the above factor gave rise to the superior strength of the NCs. Ganguly et al. [81] showed that there was a pile-up of dislocations around the SiC nanoparticles in the AZ91-Ca Sb+2.0SiC_{np} (wt.%) nanocomposite subsequent to the tensile test at 473 K.

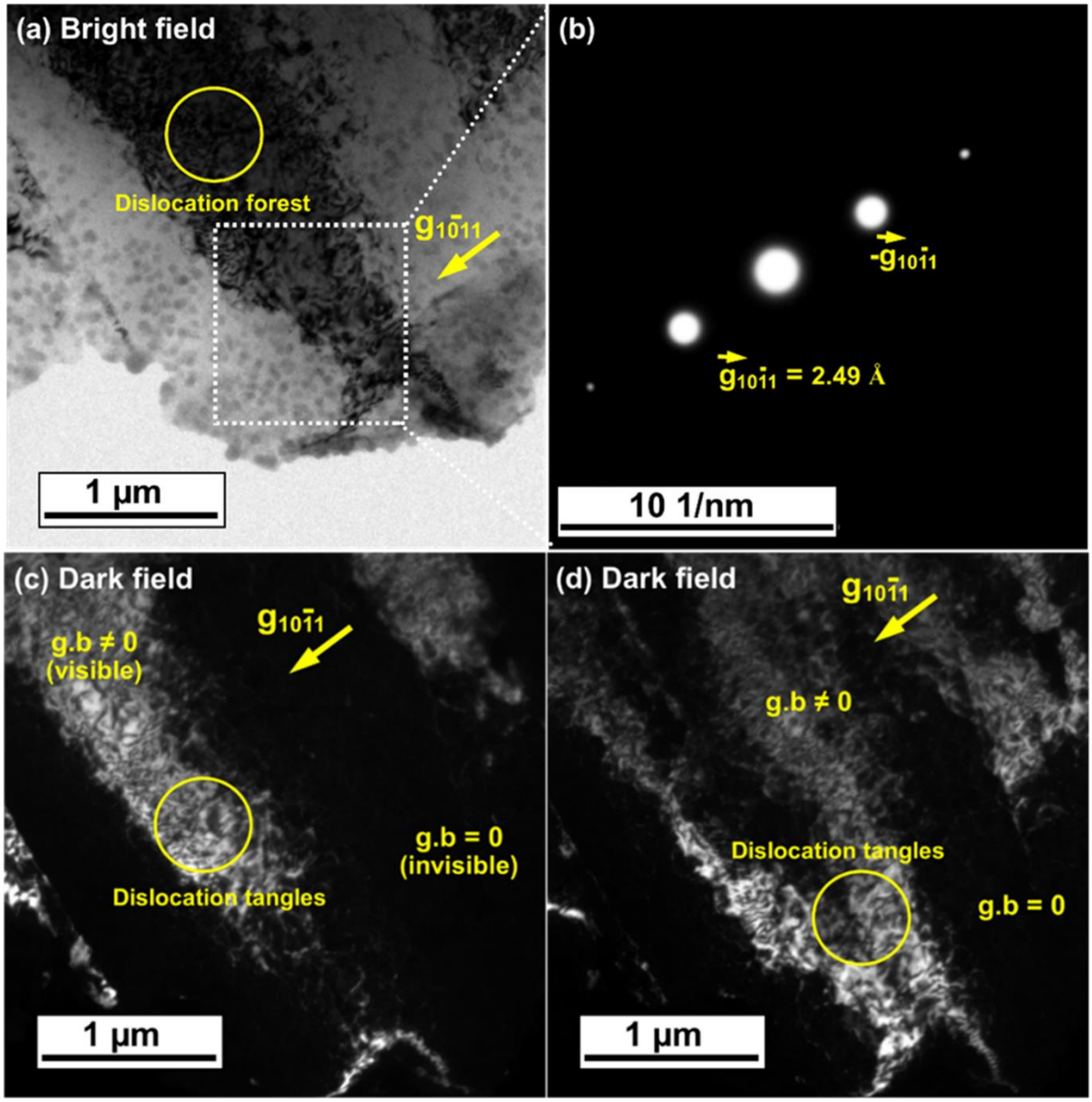

Figure 5.4 (a) TEM bright-field image exhibiting dense dislocation forest inside α-Mg grain in the AXM520 alloy; (b) weak beam diffraction pattern acquired from the region shown in 'a'; (c and d) TEM dark-field images exhibiting dense dislocation tangles [corresponding to spot $\vec{g}_{10\bar{1}1}$ and $-\vec{g}_{10\bar{1}1}$ indicated in 'b', respectively.]

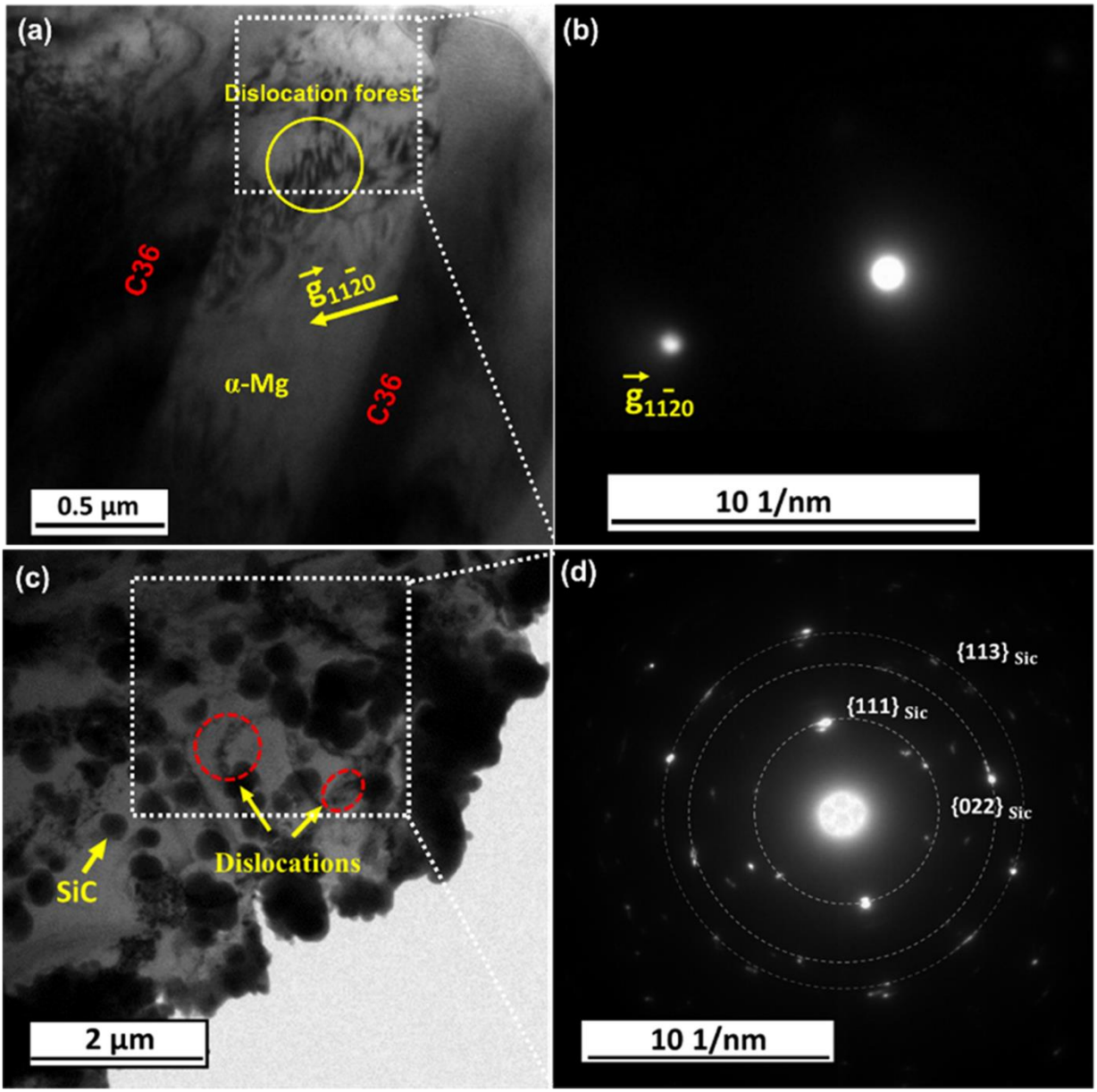

Figure 5.5 (a) TEM BF image exhibiting the dislocation pile-ups at the interface of α-Mg and C36 phases in the AXM520 alloy, and (b) SAED pattern corresponding to 'a' exhibiting two beam condition; (c) interaction of dislocations with the SiC nanoparticles in the NC2.0SiC, and (d) SAED corresponding to 'c'.

5.4 Analyses of fracture surfaces

The SEM images of the tensile fracture surfaces of the AXM520 alloy, NC2.0SiC and NC3.0SiC, are reported in Figure 5.6(a and b). The fracture surface of the AXM520 alloy in Figure 5.6(a) exhibits the presence of a few deep regions (indicated by A) with intergranular cracks. The cracked region (indicated by B) originated at the interface of the α-Mg and C36 phases. The coarse C36 phases acted as a stress raiser and initiated the crack. Subsequently, the crack propagated throughout the interface, leading to failure of the AXM520 alloy by intergranular fracture. The micrograph of the NC2.0SiC in Figure 5.6(b) reveals the presence of multiple cracks (marked by B), cleavage planes (indicated by C), and cleavage steps (indicated by D) indicating a transgranular mode of cleavage fracture [64]. In addition, multiple microvoids (marked as E) were observed in the NC2.0SiC. The presence of feature 'E' suggests that higher energy was absorbed for their formation and coalescence during the tensile deformation of the NC2.0SiC. Thus, it indicates a higher ductility of the NC2.0SiC than that of the unreinforced AXM520 alloy.

Figure 5.6(c and d) presents the fractographs of the compression-tested AXM520 alloy and NC2.0SiC. The fractographs show typical shear bands (marked as A) along the shear direction and shear steps perpendicular to it (marked as B). The presence of microcracks (marked as C) in the shear band regions was also observed. Barnett et al. [114] suggested that the microcracks resulted from the interaction of voids and secondary phases in the AZ31 alloy. The crack propagated through the cross-section of the sample at ~45 ° with respect to the loading direction. Careful observation of the fracture surface of the AXM520 alloy in Figure 5.6(c) reveals shallow shear steps than the presence of deep shear steps in the NC2.0SiC, as shown in Figure 5.6(d). The higher population of shear bands and wider shear steps indicate higher energy absorption during failure of the NC2.0SiC under compression compared to the alloy and other NCs employed [34,79].

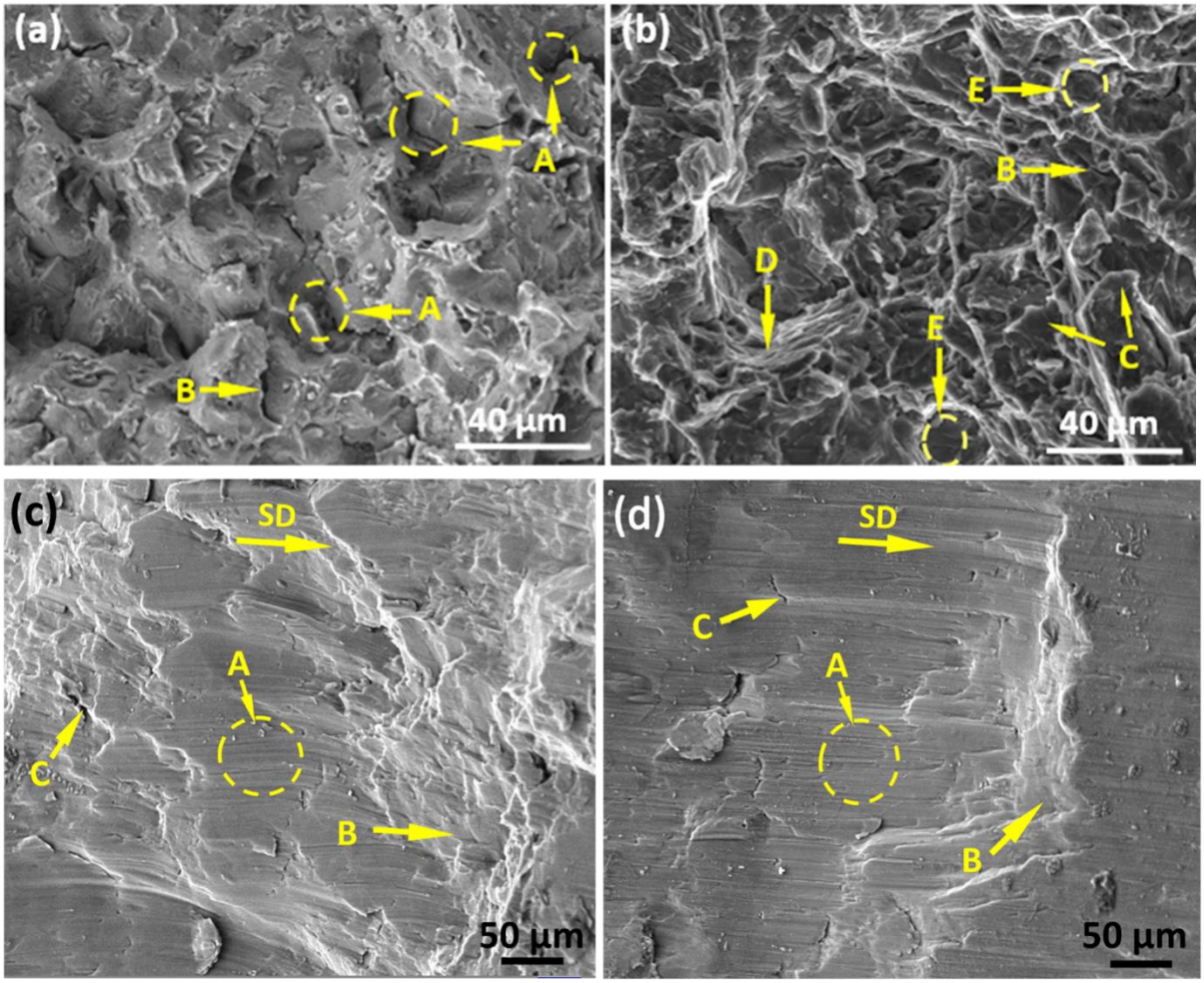

Figure 5.6 Fracture surfaces of the tensile tested (a) AXM520 alloy, and (b) NC2.0SiC; fracture surfaces of the compression tested (c) AXM520 alloy, and (d) NC2.0SiC ('SD' shear direction).

5.5 Summary of chapter 5

In the present chapter, the ambient temperature tensile and compressive properties of the AXM520 alloy and NCs have been evaluated. Detailed analyses of the strain-hardening response and fracture surfaces of the tested specimens are carried out. The major findings from the current chapter are summarized below.

i. All the NCs exhibited superior tensile properties than the AXM520 alloy. The NC2.0SiC with 37.2 and 69.8% enhancement in YS and UTS exhibited the most superior tensile properties. The %El of the AXM520 alloy and NC2.0SiC were 1.03 ± 0.03 and 3.1 ± 0.02%, and it decreased to 1.29 ± 0.02% in the NC3.0SiC. The UTS and %El of the NCs declined with more than 2.0 (wt.%) SiC_{np} to the AXM520 alloy because of the nanoparticle agglomeration.

ii. The superior compressive properties were exhibited by the AXM520 alloy with the SiC_{np} additions. The presence of thicker shear bands in the fractograph of the NC3.0SiC indicated its higher energy absorption capability during failure than the AXM520 alloy.

iii. The strengthening from CTE mismatch contributed the most to the overall strengthening of all the NCs, and the same was 146.0% greater in the NC3.0SiC than the NC0.5SiC. The contribution from Orowan strengthening also increased by 121.2%. However, the Hall-Petch strengthening increased only by 18.1%with the increase in nanoparticle content from 0.5 to 3.0 (wt.%) in the NCs.

iv. The 'Zhang and Chen' model was modified by introducing an agglomeration factor (ϕ). The theoretically predicted YS of all the NCs using the modified 'Zhang and Chen' model matches pretty well with the experimentally obtained values of the NCs.

Chapter 6

Creep Behavior

This chapter deals with the detailed creep behavior of the squeeze-cast Mg-5.0Al-2.0Ca-0.3Mn (wt.%) (AXM520) alloy and NCs. The creep behavior of the AXM520 alloy and NCs has been examined using impression creep tests. The observed creep rates are correlated with the as-cast microstructures of the alloy and nanocomposites. The governing creep mechanisms have been determined in the alloy and nanocomposites in the temperature and stress ranges employed. Further, the post-creep microstructural analyses of the alloy and nanocomposites have been carried out. A summary of the impression creep behavior of the AXM520 alloy and nanocomposites is presented at the end of this chapter.

6.1 Creep behavior

6.1.1 Nature of creep curves and comparison of creep responses

The creep performance of the AXM520 alloy and nanocomposites was investigated utilizing the impression creep technique. The variation of impression (indentation) depth with time at 498 K and 435 MPa for all the materials has been presented in Figure 6.1(a) over the same time duration. At the beginning of each creep curve, there is a certain jump in the indentation depth, and it is termed as the impression depth, similar to the instantaneous strain observed in a conventional tensile or compressive creep curve. The primary creep and thereafter a secondary or steady-state creep stage follow the instantaneous impression depth. A typical tensile creep curve exhibits three stages of creep, i.e., primary, secondary, and tertiary stages. However, the tertiary stage is not observed in an impression creep as the indentation took place under compressive stress. The compressive stress generally aids in forming a stable deformed zone beneath the indenter and prolongs the secondary stage. The impression velocities (dh/dt) derived for these curves are plotted in Figure 6.1(b) against time. The impression velocity initially decreased with time, then became almost constant, indicating a steady-state achieved. The decrease in impression velocity in the primary stage was attributed to the strain-hardening rate that dominated the recovery rate in the materials. After that, the strain-hardening rate and recovery rate counterbalanced each other, resulting in a steady-state creep. The creep

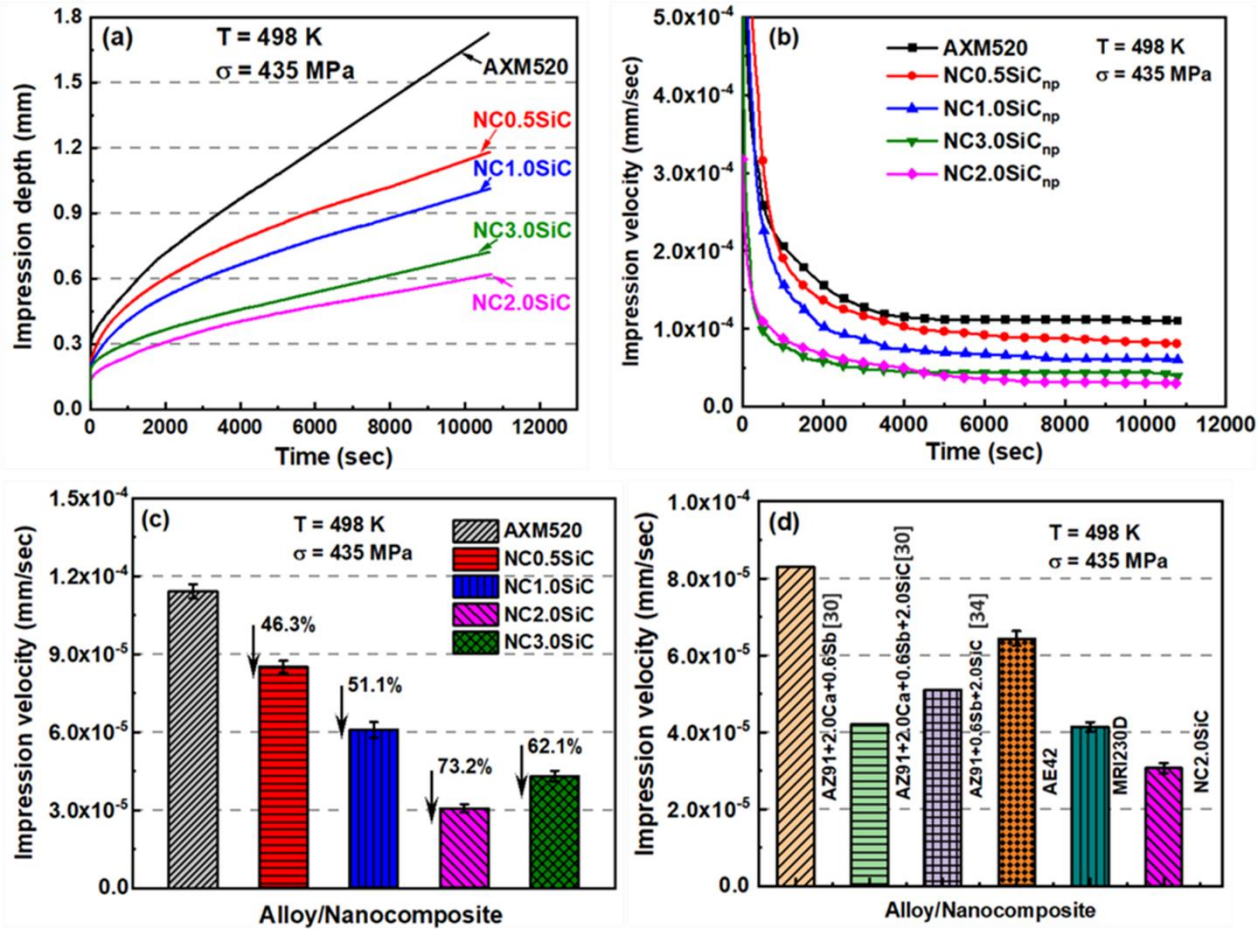

Figure 6.1 (a) Impression depth vs. time plots for the AXM520 alloy and nanocomposites nanocomposite creep tested at 498 K and 435 MPa; (b) impression velocity vs. time plots based on 'a'; and (c) steady-state impression velocities estimated from 'a'; and (d) steady-state impression velocities estimated from 'a', as well as previously reported nanocomposites, and alloy [30,34].

performance of the alloy and nanocomposites can be quantified in terms of indentation depth and steady-state impression velocity. At particular stress and temperature, a lower value of impression depth for a fixed duration or a lower value of steady-state impression velocity specifies superior creep performance. The impression depths recorded for the nanocomposites significantly reduced over the AXM520 alloy. The indentation depth gradually decreases as the SiC nanoparticles contents increase in the nanocomposites up to 2.0 (wt.%) SiC_{np}, and thus, it was the lowest in the case of NC2.0SiC. However, the impression depth did not decrease, although the fraction of SiC_{np} was changed from 2.0 to 3.0 (wt.%). The values of the V_{imp} of AXM520 and NCs are summarized in Figure 6.1(c). The impression velocities of the NCs were lower than AXM520 alloy, indicating superior creep resistance of the former materials compared to the latter. The creep performance of the NCs increased as SiC_{np} content increased; thus, the creep resistance of NC2.0SiC increased by 73.2%. However, with the further increase in the nanoparticles content, the creep resistance deteriorated, and accordingly, the NC3.0SiC exhibited a 62.1% improvement compared to the alloy. The deterioration of creep resistance of NC3.0SiC was attributed to the agglomeration of nanoparticles, resulting from the higher content of SiC_{np} in the NCs. Thornby et al. [115] explored the creep response of the Mg-(0-0.75 vol.%) CNT nanocomposites. They, too, observed that the creep performance of the NCs improved up to 0.5 vol.% CNT content, and beyond that, the creep resistance deteriorated. Further, the well-known creep-resistant AE42 and MRI230D alloys at the comparable stress and temperature (i.e., 435 MPa and 498 K) were subjected to impression creep tests, and the creep rates of these two alloys are compared with that obtained in NC2.0SiC in in Figure 6.1(d). The reported values of the AZ91+2.0Ca+0.6Sb, AZ91+2.0Ca+0.6Sb+2.0SiC, and AZ91+0.6Sb+2.0SiC are also compared with that of NC2.0SiC in Figure 6.1(d) [30,34]. Interestingly, the impression velocity of the NC2.0SiC is the lowest. Thus, it revealed the best creep performance among the standard creep-resistant alloys and nanocomposites employed for comparison.

6.1.2 Assessment of creep mechanism

A conventional tensile or compressive creep test is generally conducted at a constant temperature and constant stress to evaluate the creep performance of materials. The temperature (T), stress (σ), and grain size (d) dependence of creep rate ($\dot{\epsilon}$) under steady-state condition is expressed using the following power-law relationship [65].

$$\dot{\epsilon} = A\left(\frac{b}{d}\right)^{p}\left(\frac{Gb}{kT}\right)D_0\left(\frac{\sigma}{G}\right)^{n} e^{\left(\frac{-Q_c}{RT}\right)} \qquad \text{Equation 6.1}$$

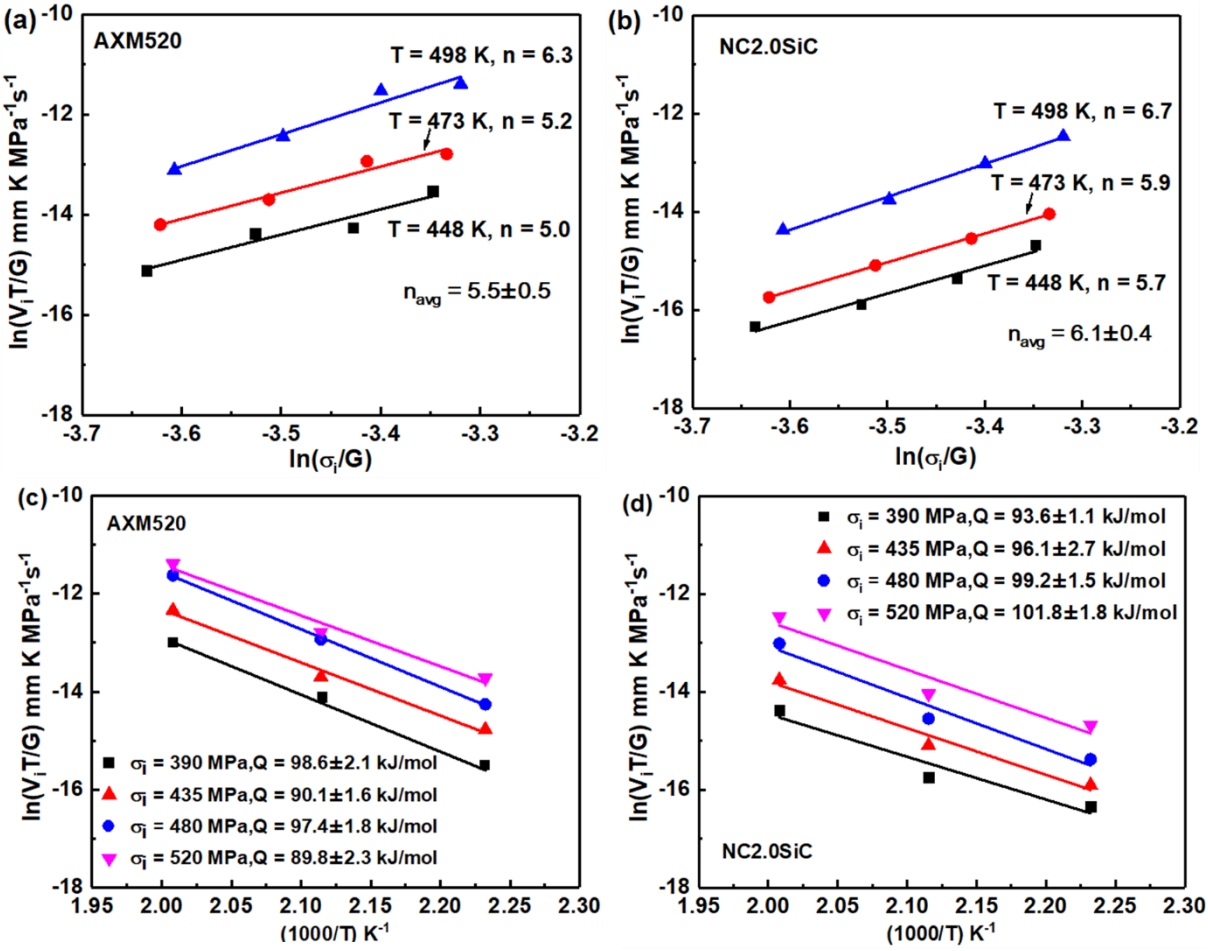

Figure 6.2 Stress dependence of the steady-state impression velocities at different temperatures for the (a) AXM520 alloy and (b) NC2.0SiC; temperature dependence of the steady-state impression velocities at different stresses for the (c) AXM520 alloy and (d) NC2.0SiC.

The σ and $\dot{\epsilon}$ in a tensile/compressive creep are related to the stress employed in impression creep (σ_{imp}) and impression velocity (V_{imp}) (calculated under steady-state) as follows:

$$\dot{\epsilon} = \frac{V_{imp}}{C_2 \emptyset} \text{ and } \sigma = \frac{\sigma_{imp}}{C_1} \text{ where } \sigma_{imp} = \frac{4F}{\pi \emptyset^2} \qquad \text{Equation 6.2}$$

Thus, the expression equivalent to equation (1) in an impression creep is given by [116].

$$\left(\frac{V_{imp}\, T}{G}\right) = B \left(\frac{\sigma_{imp}}{G}\right)^n e^{\left(-\frac{Q_c}{RT}\right)} \qquad \text{Equation 6.3}$$

In equation 6.3, B is an overall pre-exponential constant. The definitions of the parameters of equations 6.1 to 6.3 are provided in Table 6.1. The value of shear modulus (G) decreases with an increase in temperature. Thus, an expression provided in [30] for Mg alloy is employed for temperature-compensated shear modulus. Stress exponents (n) and activation energies (Q) were evaluated from Equation 6.3 to ascertain the mechanism responsible for creep in the materials. A series of creep tests were conducted at varying stress and temperature. The n and Q values were evaluated from the gradients of $\ln\left(\frac{V_{imp}\, T}{G}\right)$ vs. $\ln\left(\frac{\sigma_{imp}}{G}\right)$ (at constant T), as well as $\ln\left(\frac{V_{imp}\, T}{G}\right)$ vs. $\left(\frac{1}{T}\right)$ (at constant σ) plots, respectively. The representative plots exhibiting the calculation of n and Q for AXM520 and NC2.0SiC are provided in Figure 6.2(a to d). The summary of n and Q values for all the materials employed are included in Tables 6.2 and 6.3, respectively.

Table 6.1 Definitions of the parameters used in the equations.

Symbols	Definition	Symbols	Definition
$\dot{\varepsilon}$	Steady-state creep rate (s^{-1})	**Q**	Creep activation energy (kJ. K^{-1}.mol^{-1})
A	A material constant	**R**	Universal gas constant (8.314 J. K^{-1}.mol^{-1})
b	Burgers vector (Å)	**T**	Absolute temperature (K)
D	Grain size (μm)	V_{imp}	Impression velocity (mm.s^{-1})
p	Inverse grain size exponent	**Ø**	Indenter (Punch diameter (mm))
G	Shear modulus (MPa)	**h**	Impression depth (mm)
D_0	Coefficient of self-diffusion	**F**	Applied load on punch (N)
K	Boltzmann's constant (1.38×10^{-23} kg.m^2. s^{-2}. K^{-1})	**B**	A constant
σ	Applied stress (MPa)	C_1, C_2	Constants
n	Stress exponent	σ_{imp}	Stress in impression creep (MPa)

Table 6.2 Summary of the n values obtained from the creep tests at different temperature levels.

Temperature (K)	Stress exponent (n)				
	AXM520	**NC0.5SiC**	**NC1.0SiC**	**NC2.0SiC**	**NC3.0SiC**
448	5.0	4.3	5.4	5.7	6.2
473	5.2	6.7	6.4	5.9	5.5
498	6.3	5.8	6.5	6.7	6.5
Average (n_{avg})	5.5±0.5	5.6±1.0	6.1±0.5	6.1±0.4	6.1±0.4

Table 6.3 Summary of the Q values obtained from the creep tests at different stress levels.

Stress (MPa)	Activation energy (Q) (kJ/mol)				
	AXM520	**NC0.5SiC**	**NC1.0SiC**	**NC2.0SiC**	**NC3.0SiC**
390	98.6±2.1	80.6±5.3	93.2±2.8	93.6±1.1	88.1±1.1
435	90.1±1.6	81.4±0.2	78.1±0.6	96.1±2.7	98.1±0.4
480	97.4±1.8	82.3±0.6	84.4±0.6	99.2±1.5	92.3±2.3
520	89.8±2.3	92.2±2.9	105.5±2.3	101.8±1.8	93.9±1.9

The n values for the alloy were 5.0 to 6.3, and the same for the nanocomposite was from 4.3 to 6.7, indicating that dislocation climb was the creep mechanism for all the materials. The Q values were in the range from 89.8±2.3 to 98.6±2.1 kJ/mol for the alloy, whereas the same was in the range from 78.1±0.6 to 105.5±2.3 kJ/mol for the NCs. The Q value in the present study lies between 78.1 to 105.5 kJ/mol. The energy needed for self-diffusion within the lattice of Mg is 135 kJ/mol, and the same for pipe-diffusion is 92 kJ/mol [117]. Therefore, the climb of dislocation assisted by pipe diffusion was the mechanism for creep deformation in the alloy and NCs at all the combinations of temperature and stress values utilized in the present study.

6.2 Post-creep microstructural analysis

6.2.1 Observation of sub-surfaces

The specimens of the AXM520 alloy and NC2.0SiC exposed to creep deformation at 435 MPa and 498 K were bisected along the diameter of the impressions to observe the microstructural changes below the indentation. One such bisected piece for each material was taken, and the surfaces below the indentation were observed under a microscope. Figure 6.3(a and b) exhibits the grain orientation map of AXM520 alloy and NC2.0SiC, respectively. The area mapped with identical color signifies the same orientation of the grains. The orientation maps of

AXM520 alloy and NC2.0SiC exhibited three separate regions below the indentation, namely R1, R2 and R3. The regions R1 and R3 correspond to undeformed zones below the indenter. The region R2 indicates the deformed region. The regions R1 and R3 exhibit comparatively larger grains than region R2. Additionally, region R2 displays a higher number of oriented grains than regions R1 and R3. The average widths of region R2 in the AXM520 alloy and NC2.0SiC was 203.8 ± 21.3 μm and 128.3 ± 15.2 μm, respectively. Thus, the extent of deformed zone of NC2.0SiC was less compared to the AXM520 alloy. The grain boundary maps taken from the AXM520 alloy and NC2.0SiC are shown in Figure 6.3(c and d). The grain that has miss orientation angle below 15 ° is known as a low-angle grain boundary (LAGB), while the high-angle grain boundary (HAGB) has a characteristic miss orientation angle greater than 15 °. The population of HAGBs is higher in the deformed region R2 compared to regions R1 and R3. The presence of a large population of HAGBs in R2 indicates that the grains in the plastically deformed region had undergone dynamic recrystallization owing to exposure at elevated temperature during the creep tests. Figure 6.3(e and f) exhibits the Kernel Average Misorientation (KAM) maps constructed from the deformed regions of both the AXM520 alloy and NC2.0SiC nanocomposite. The KAM map represents the average misorientation between a particular pixel and its specified nearest neighbor. The KAM maps estimate the deformation in crystals [118]. In the present investigation, for constructing the KAM maps the average misorientation of a particular pixel was calculated up to its three nearest neighbors with the provision that misorientation not exceeding 5 °. The different colours indicate the extent of local misorientation inside individual grain. Blue and red colours were for the grains without any misorientation (0 °) and the maximum misorientation (5 °), respectively. The changeover of the blue colour corresponding to the KAM distribution at low angle to yellow colour corresponding to higher angle indicates the increase in the grain boundary misorientation strain (GBMS) among the grains. Thus, the intensity of blue colour corresponding to region R2 is the highest compared to regions R1 and R3 in both the alloy and nanocomposite. The lower KAM value of the deformed region, R2, compared to the undeformed region, R3, was attributed to the dynamic recrystallization of the deformed region during the impression creep test. The creep tests were performed at a constant stress and constant temperature. The deformation and dynamic recrystallization took place simultaneously owing to the exposure to temperature for a long time. In addition, the intensity of blue colour in the region R2 of the nanocomposite reduced compared to that in the alloy indicating that the local GBMS was more in the nanocomposite.

The regions below indentations for AXM520 alloy and NC2.0SiC exposed to creep at 435 MPa and 498 K were further characterized using SEM, and the micrographs are shown in Figure 6.4(a and b). Three distinct regions below the indentation are observed, as discussed earlier. The deformation characteristics of the region below the cylindrical indenter in an impression creep is well explained using the typical Hertzian stress distribution employing [119]

$$\frac{\sigma_z}{p_m} = -\frac{1}{2}\left(1 - \frac{r^2}{a^2}\right)^{-1/2} \qquad \text{Equation 6.4}$$

where σ_z is the applied normal stress, P_m denotes the mean contact pressure below indentation, 'a' is the cylindrical flat indenter (punch) radius and r is the radial distance from the center of the indenter. At r = 0, i.e., at the center of the indenter, σ_z equals to -0.5P_m; and at r = a, i.e., at the edges of the indenter, reaches infinity at the edges of the indenter, i.e., r = a. Thus, the region immediately beneath the indenter, i.e., region R1, exhibits a low deformation region and forms a hemispherical dead zone. The region marked as R2 shows the characteristics of localized shear deformation owing to high stress concentration at the periphery of the indenter. The width of region R2 implies the ability of the material to withstand the applied stress. The extent of region R2 was different in AXM520 alloy and NC2.0SiC. Region R3, away from the indenter periphery, exhibits a microstructure comparable to the undeformed one, indicating that the stress experienced in this region was negligible.

The magnified view of region R2 in Figure 6.4(a) exhibits that the connectivity of the C36 phase in the AXM520 alloy was completely disintegrated and fragmented along the flow of the metal. The disintegration of the C36 phase was also observed in NC2.0SiC, as shown in Figure 6.4(b). However, the fragmentation of the C36 was not severe as compared to the AXM520 alloy. This indicates that additions of SiC_{np} in the AXM520 alloy improved deformation resistance of α-Mg. Thus, narrowing down the extent of region R2 in NC2.0SiC implies its improved creep response over AXM520 alloy. The improved strengthening of α-Mg matrix in NC2.0SiC was attributed to the Orowan strengthening imparted by the SiC nanoparticles. The presence of the C36 phase alone in AXM520 alloy provided the grain boundary pinning effect during creep deformation. However, the dispersion of SiC_{np} in AXM520 alloy strengthened the α-Mg matrix by Orowan strengthening. Thus, the creep performance of the NC2.0SiC was improved significantly than the AXM520 alloy. However, the effect of Orowan strengthening reduced when the fraction of SiC_{np} increases to 3.0 (wt.%) in NC3.0SiC. The declination in creep property of the NC3.0SiC was governed by the agglomeration of SiC_{np} as the amount of SiC increased.

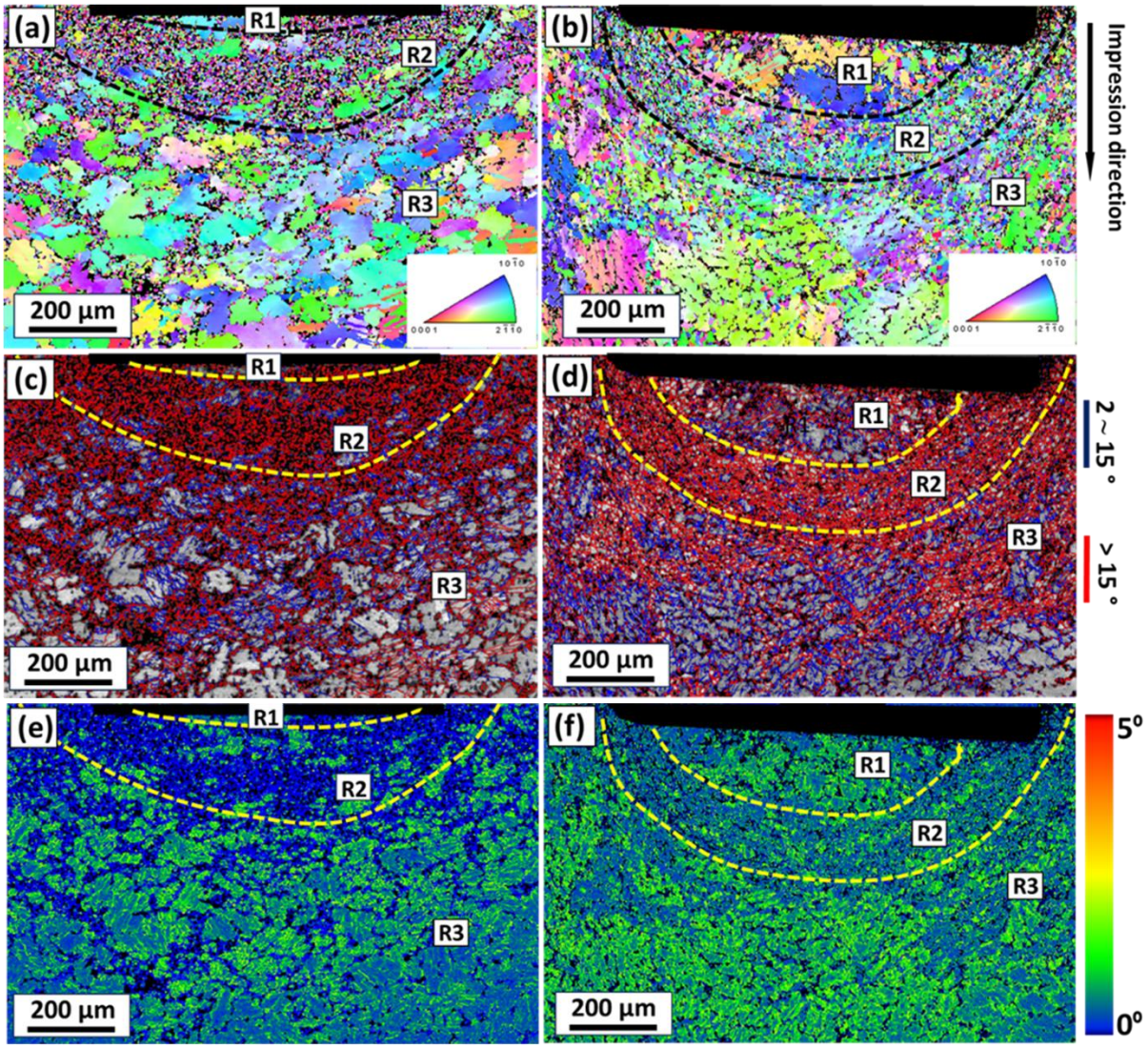

Figure 6.3 EBSD map of the creep tested samples showing grain orientation map under the punch for (a) AXM520 alloy, and (b) NC2.0SiC creep tested at 498 K and 435 MPa; corresponding grain boundary maps (c and d) and KAM maps (e and f) for the AXM520 alloy (from a) and NC2.0SiC (from b).

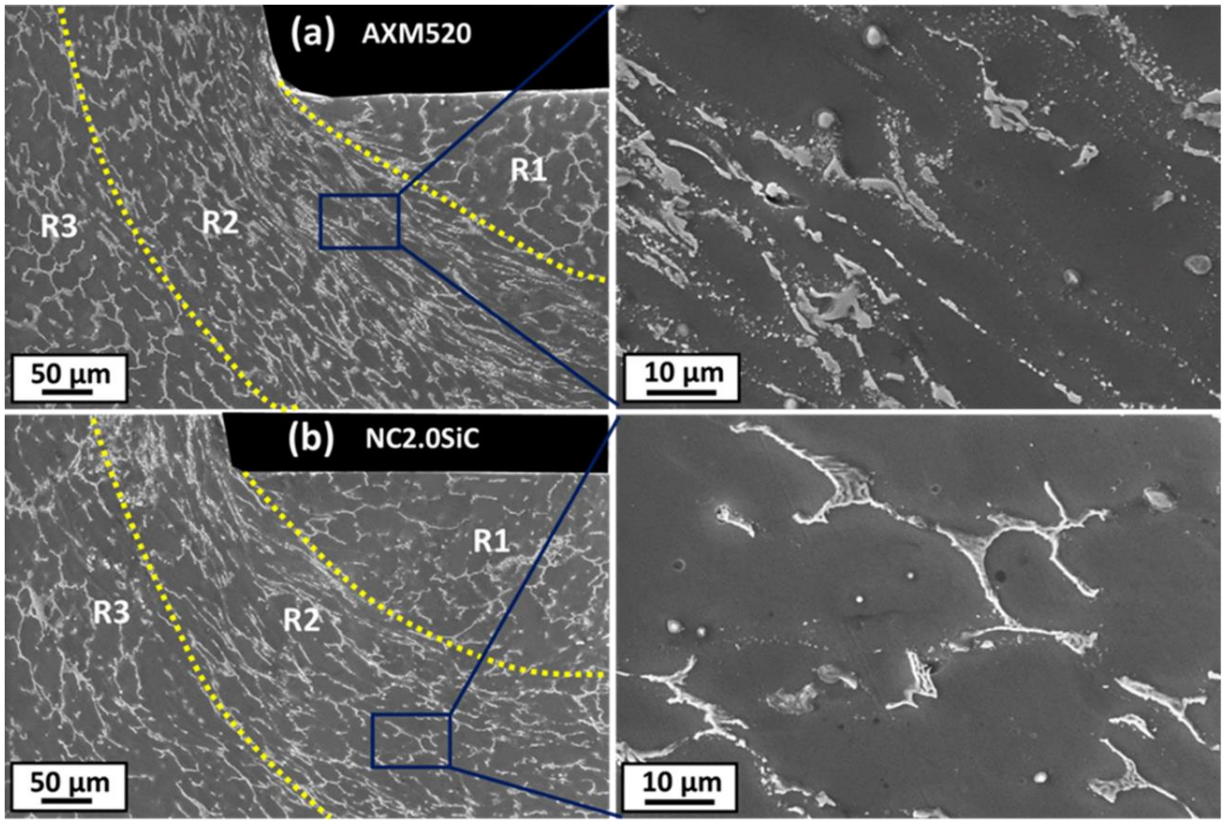

Figure 6.4 SEM micrographs displaying flow configuration underneath the indentations for the (a) AXM520 alloy, and (b) NC2.0SiC nanocomposite creep tested at 498 K and 435 MPa.

6.2.2 Observation of dislocations

The TEM brightfield (BF) images of the creep-exposed AXM520 alloy and NC2.0SiC specimens are shown in Figure 6.5(a to e). The presence of numerous dislocations is observed in the micrographs. Figure 6.5(a) exhibits the dislocation forest in the α-Mg matrix of the AXM520 alloy, and Figure 6.5(b) exhibits a planner defect bounded by two parallel edges. The presence of several dislocations within the planner defect is also noted. The characteristic of the planner defect in the micrograph is similar to that of twins. The formation of twins in the Mg alloys during creep deformation was described previously as well [120]. The dense dislocation network in the α-Mg matrix is portrayed in Figure 6.5(c). These features indicate that the dislocations interacted during movement, creating a dislocation network and dislocation entangled during creep deformation of the AXM520 alloy. The dislocations are free to move inside the grain during creep deformation under the applied stress in the absence of any obstacle. However, their movement is restricted once they reach the grain boundaries. This is because the regular arrangement of atoms at the grain boundary is broken, and there is a difference in orientation between the two grains. Thus, the grain boundaries act as an obstacle to the dislocation's movement. The dislocations created a pile-up around the C36 phase in the AXM520 alloy, as shown in Figure 6.5(d). The pile-up of dislocation provides a back stress to the incoming dislocations, which is one of the factors responsible for the work-hardening of the alloy. The presence of several dislocations within the grain is also observed. The presence of a secondary phase at the grain boundaries also impeded the motion of dislocations during the creep deformation. The SiC_{np} in the NC2.0SiC provided additional obstruction to the dislocation motion, and a pile-up of dislocation took place near the SiC nanoparticles, as shown in Figure 6.5(e). The SAED pattern acquired from Figure 6.5(e) is shown in Figure 6.5(f). The analysis of the SAED pattern confirms the presence of SiC_{np} in α-Mg. Thus, the additional strengthening owing to the presence of SiC_{np} in NC2.0SiC caused its superior creep performance over the AXM520 alloy. Figure 6.6(a to f) exhibits the BF and DF TEM micrographs taken with B = $[\bar{1}2\bar{1}1]$ from the grain interior (i.e., α-Mg phase) of the AXM520 alloy creep tested at 498 K and 435 MPa. The BF and DF images in Figure 6.6(a and b) reveal the dislocations in the selected region. To understand the nature of dislocations, the **g.b** analyses were performed. The <c> type dislocation inside the grain interior was made visible with **g**= {0002} and is presented in Figure 6.6(c and d). The <a> type dislocation in the same region was also made visible with **g**= $\{10\bar{1}0\}$ and is shown in Figure 6.6(e and f). The probable burger vectors of the dislocations are $\pm[11\bar{2}3]$, $\pm[\bar{2}113]$, $\pm[11\bar{2}\bar{3}]$, and $\pm[\ \bar{2}11\bar{3}]$ [121]. The presence

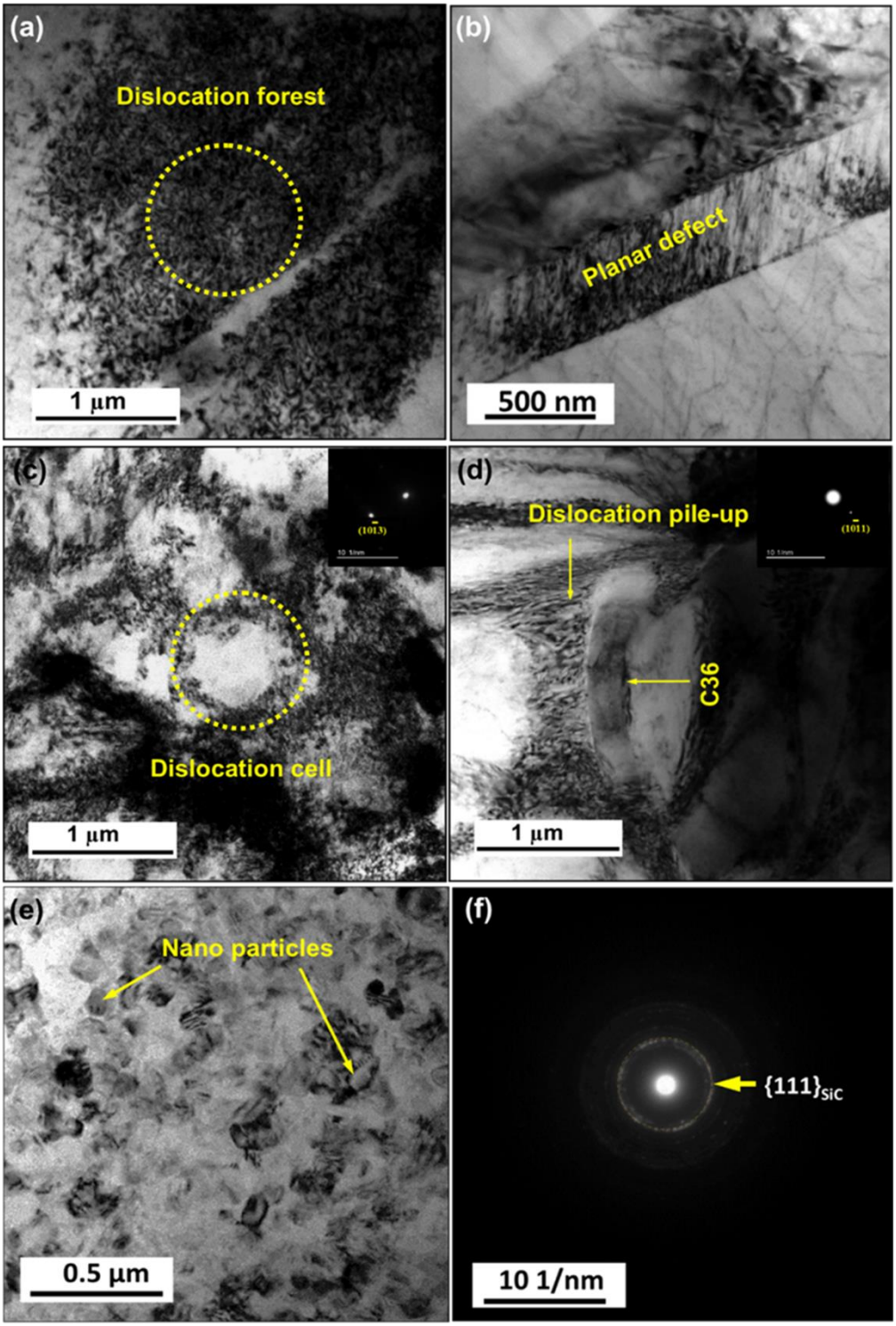

Figure 6.5 Bright Field (BF) TEM micrographs of the AXM520 alloy creep tested at 498 K and 435 MPa showing the (a) dislocation forest, (b) planner defect, (c) dislocation cell in the α-Mg matrix, and (d) dislocation pile-ups around the C36 phase; (e) BF TEM micrograph micrographs of the NC2.0SiC nanocomposite creep tested at 498 K and 435 MPa showing the dislocation pile-ups near the nanoparticles, and (f) SAED pattern taken from 'e'.

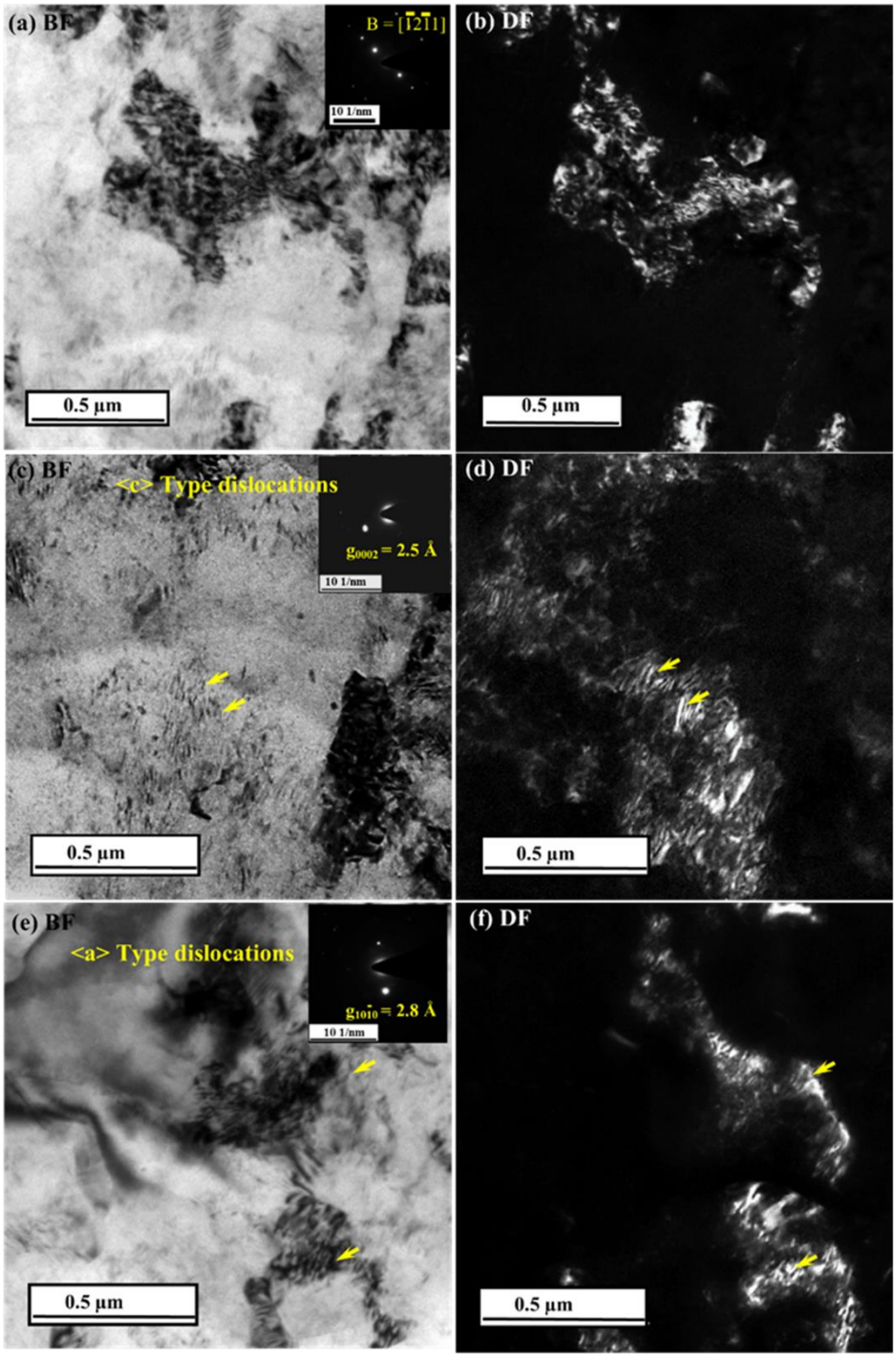

Figure 6.6 BF (a) and DF (b) TEM micrographs taken with B = [1$\bar{2}$1$\bar{1}$] from the grain interior (i.e., α-Mg phase) of the AXM520 alloy creep tested at 498 K and 435 MPa depicting the dislocations; BF (c) and DF (d) TEM micrographs taken with $\overrightarrow{g_{[0002]}}$ reveal the presence of <c> type dislocation in 'a'; BF (e) and DF (f) TEM micrographs taken with $\overrightarrow{g_{[10\bar{1}0]}}$ reveal the presence of <a> type dislocation in 'a'.

of the <c> type dislocation indicates the activation of the <c> slip plane at elevated temperature. In addition, the dissociation of the <c+a> dislocation into <a> and <c> components and the subsequent annihilation of the <a> dislocation (basal component) by glide leave the <c> dislocation [122,123].

6.3 Summary of chapter 6

In this chapter, the detailed creep behavior of the squeeze-cast Mg-5.0Al-2.0Ca-0.3Mn (wt.%) (AXM520) alloy and NCs has been presented. The major findings from the current chapter are summarized below.

i. The NCs revealed improved creep performance compared to the AXM520 alloy under the experimental parameters utilized. The creep resistance of the NCs increases with the increase in the SiC_{np} content. The NC2.0SiC exhibited an increase in creep resistance by 73.2% compared to the alloy. However, the creep resistance deteriorated with a further increase in the fraction of the SiC_{np} in the NC3.0SiC, due to the agglomeration.

ii. The stress exponents varied from 5.0 to 6.7, and activation energies varied from 89.8 to 101.8 kJ/mol, implying the deformation at elevated temperature in the AXM520 alloy and NCs was dominated by the climb of dislocation assisted by the pipe diffusion.

iii. The pile-ups of dislocations took place around the C36 phase and near the SiC_{np}. The additional strengthening owing to the presence of the SiC_{np} in the NCs was responsible for their improved creep performance compared to the AXM520 alloy.

Chapter 7

Corrosion Behavior

In this chapter, the corrosion behavior of squeeze-cast Mg-5.0Al-2.0Ca-0.3Mn (wt.%) (AXM520) alloy and nanocomposites are investigated by hydrogen evolution, and potentiodynamic polarization methods in an aqueous NaCl solution. The corrosion products and corroded surfaces are analyzed with the help of X-ray Diffraction (XRD), Scanning Electron Microscopy (SEM), and X-ray photoelectron spectroscopy (XPS). The corrosion behavior of the alloy and NCs is correlated with their initial as-cast microstructures. A summary of the corrosion work is presented at the end of this chapter.

7.1 Hydrogen evolution and immersion tests

Mg undergoes corrosion by reacting with water and emit H_2 gas as per the below equation [124]:

$$Mg + 2H_2O \rightarrow Mg(OH)_2 + H_2 \uparrow \qquad \text{Equation 7.1}$$

The results of hydrogen evolution tests for AXM520 alloy and NCs following 60 h of immersion in NaCl are plotted in Figure 7.1(a). The H_2 evolution for the alloy and NCs accelerated with the passing immersion time. The H_2 evolution of the individual NC remains lower than the alloy. Figure 7.1(b) presents the corrosion rates assessed from the immersion tests. The NCs exhibit a lower rate of corrosion than that of AXM520 alloy for the entire duration. Thus, the incorporation of SiC_{np} caused a reduced corrosion rate of NCs. Further, the corrosion rate gradually diminished with the rise in SiC_{np} concentration in the alloy. The lowest corrosion rate was exhibited by NC3.0SiC. The corrosion rates (mm/yr) of the AXM520 and NC3.0SiC obtained from the current study are compared with the values previously reported for the various Mg-Al-based alloys and their composites in Table 7.1. The newly developed NCs in the current study displayed significantly greater resistance during corrosion relative to the published values. The corrosion rates of the AXM520 and NCs calculated from the weight loss measurements are shown in Figure 7.1(c and d). The results of immersion tests reconfirm the trend observed in the corrosion rates observed in the hydrogen evolution tests for the alloy and NCs. The NCs exhibited lower rates of corrosion than the AXM520 alloy for the entire duration. In addition, the corrosion rate gradually diminished with the increase in SiC_{np} concentration in the alloy.

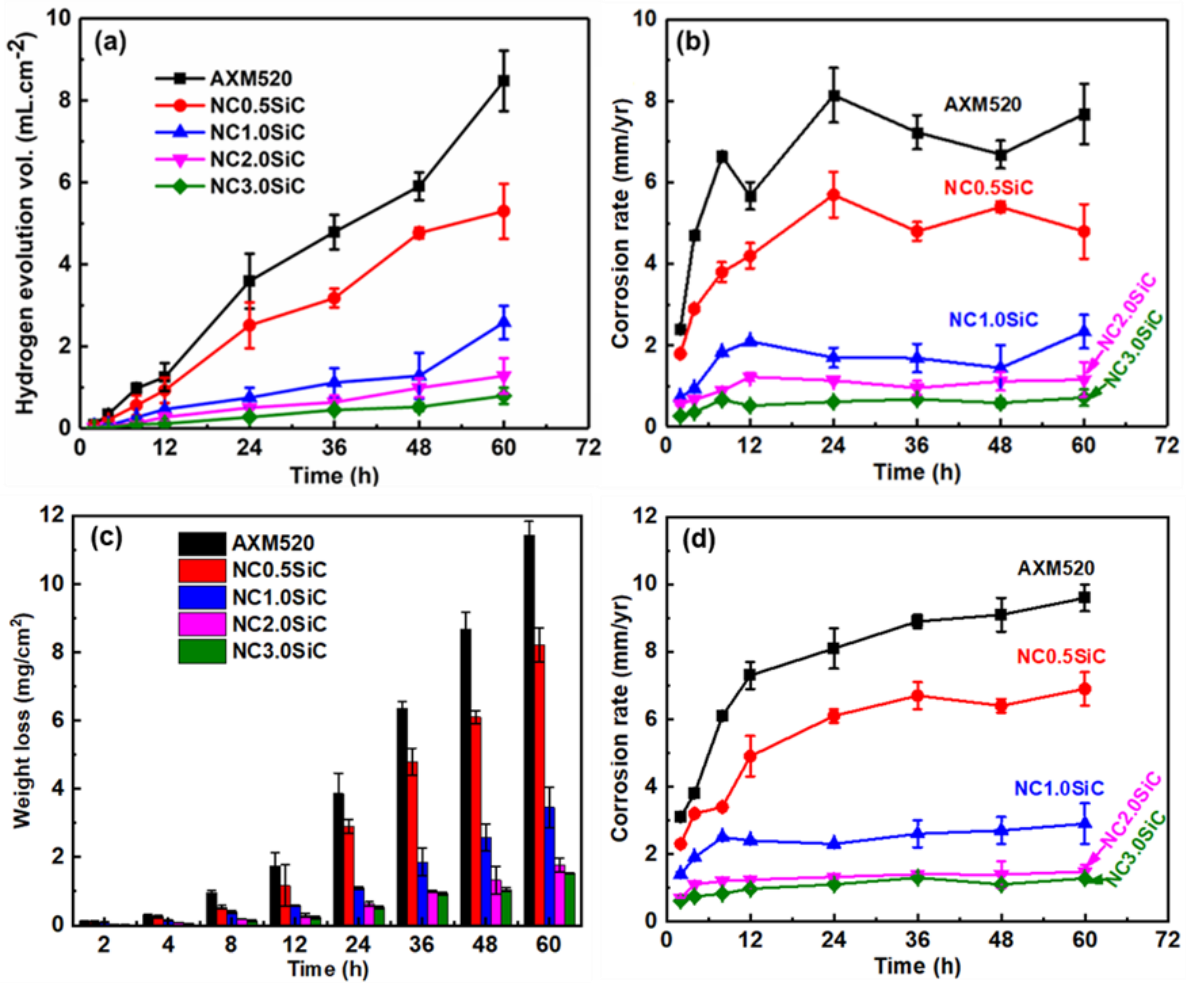

Figure 7.1 (a) Hydrogen evolution as a function of time, (b) corrosion rate calculated from 'a' for AXM520 and NCs, (c) weight loss of the alloy and NCs as a function of time, and (d) corrosion rates calculated from 'c'.

Table 7.1 A comparison of corrosion rates evaluated from H_2 evaluation tests in the present study with that obtained on various Mg-Al-based alloys and their composites.

Materials	Fabrication Process	Corrosion medium	Immersion time (h)	Corrosion rate (mm/yr)	Ref.
AZXY9120+ 2.0 wt. SiC_{np}	Squeeze casting	0.1 (M) NaCl Soln.	10	102.00±1.30	[44]
AZXB9120	Squeeze casting	0.1 (M) NaCl Soln.	12	69.20±2.40	[125]
AZ91+2.0 (wt.%) GNP	Squeeze casting + 20 s ultrasonic shot peening	0.1 (M) NaCl Soln.	12	20.00±1.70	[126]
Mg-1.0Al-0.3Ca	Extruded and heat treated at T6 200 ºC for 4 h	0.6 (M) NaCl Soln.	48	4.36±0.77	[127]
AXM520	Squeeze casting	0.6 (M) NaCl Soln.	60	7.08±0.85	This work
AXM520+3.0 (wt.%) SiC_{np}	Squeeze casting	0.6 (M) NaCl Soln.	60	0.63±0.13	This work

7.2 Open circuit potential (OCP)

The results from the OCP tests of the AXM520 and fabricated NCs are plotted in Figure 7.2. Following an initial small variation, the OCP of all the materials achieved a steady state, and it was attributed to a stable corrosion layer formation on the surfaces of the alloy and NCs [44]. The OCP values shifted more to the positive voltage (E_{OCP}) as the wt.% of nanoparticles gradually raised in the AXM520 alloy. The average OCP values for all the tested materials assessed from the curves in Figure 7.2 are summarized in Table 7.2. The AXM520 alloy exhibited the lowest E_{OCP} (i.e., -1559.7 ± 4.8 mV) among the materials employed. The OCP values of all the NCs were higher in contrast to the alloy, and the values gradually became bigger with the increased wt.% of the SiC_{np} content in NCs. Among the NCs, the lowest E_{OCP} (i.e., -1538.2 ± 5.3 mV) and highest (i.e., -1453.1 ± 5.3 mV) values were exhibited by NC0.5SiC and NC3.0SiC, respectively. The E_{OCP} values for the NC1.0SiC and NC2.0SiC were

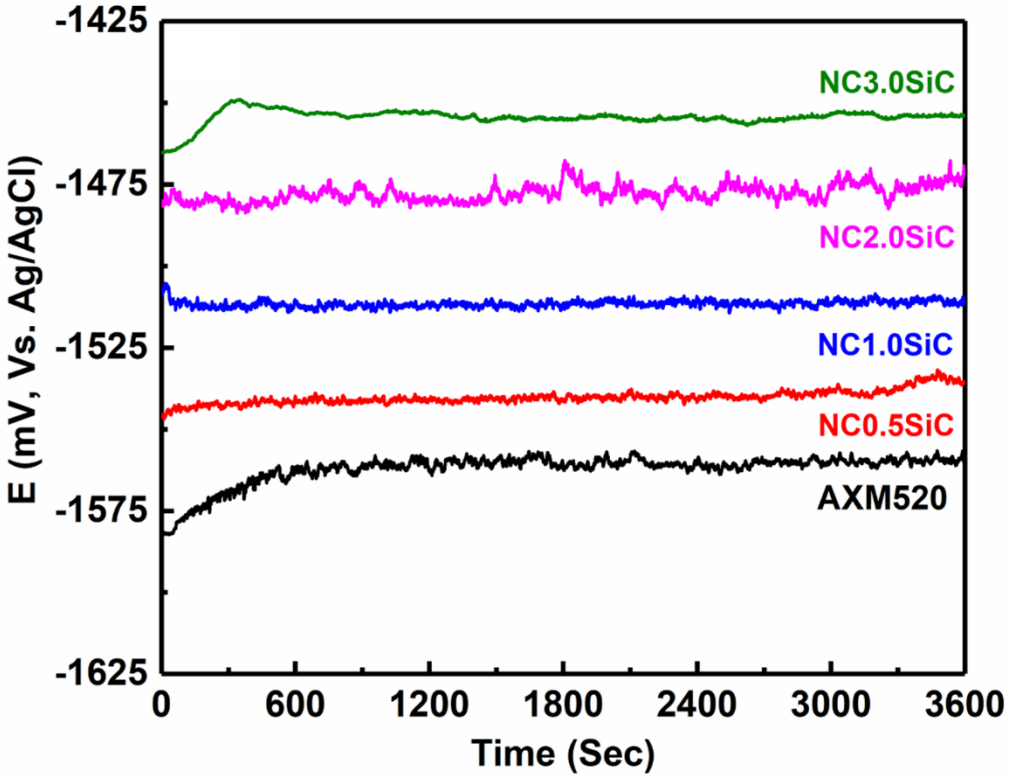

Figure 7.2 Variation of OCP recorded as a function of time for all the materials tested.

-1511.5 ± 2.7 and -1474.3 ± 6.7 mV, respectively. Thus, the NC3.0SiC was the noblest among the NCs, and it exhibited a 6.8% improvement in E_{OCP} value compared to the AXM520 alloy.

7.3 EIS studies

Figure 7.3(a) exhibits the Nyquist plots for as-cast AXM520 and NCs. The loop radius of the curve obtained from the AXM520 alloy was the smallest, and it was bigger for all the NCs, indicating the corrosion resistance was the lowest for the alloy. The loop radius increased with the increase in SiC_{np} in the NCs, which suggests that the corrosion resistance of NCs enhanced as wt.% of SiC_{np} is increased in them. Among the NCs, the loop radius was the highest for NC3.0SiC and lowest for NC0.5SiC. The presence of an inductive loop at the low-frequency domain signifies the adsorption and decomposition of ions due to the reaction of the α-Mg phase with the C36 phase [128]. The coupling of the primary phase with the secondary phases resulted in galvanic corrosion of both the alloy and NCs [124]. The large loops at high and mid-frequency ranges correspond to the capacitive loops, which is attributed to the charge transfer resistance at the interface of the electrolyte and working electrode. The increased loop radius of the NCs at higher frequency with increasing SiC_{np} content suggests that the charge transfer rate became slow in the NCs compared to the AXM520 alloy. The inductance loop at low-frequency region is associated with the localized corrosion by Cl^- ions and break down of the corrosion product film.

Figure 7.3(b) displays the Bode magnitude plots for all the as-cast compositions. The plots exhibit the variation of impedance magnitude (|Z|) within the chosen frequency range. The AXM520 alloy exhibited the lowest value of |Z| whereas, it was highest in NC3.0SiC. The values of |Z| for all the NCs were higher compared to the alloy. The |Z| value proportionally improved with that of the SiC_{np} wt.% in AX520. This implies that the resistance against corrosion of the AXM520 is enhanced with the added SiC_{np} reinforcement. The |Z| value exhibited in the low-frequency region showed a positive slope, implying the presence of an inductive loop. The negative slope of the variation of |Z| at the mid and high-frequency range suggests the presence of a capacitive loop. The variation of |Z| parallel to the abscissa implies the presence of pure resistance. Figure 7.3(c) presents the Bode phase plots for all the compositions corresponding to the Nyquist plot displayed in Figure 7.3(a). In the Bode phase diagram, an increase in the phase angle and width of the peak implies a higher resistance, reduced capacitance, and higher corrosion resistance [127,129,130]. In the present

investigation, the phase angle and FWHM (Full-Width Half Maxima) of the largest peak corresponding to these plots increased proportionally with the increased SiC_{np} concentration in the AXM520 alloy. The FWHM value of the AXM520 alloy is 1.81 ± 0.12, and it is 2.30 ± 0.13 for NC3.0SiC. The NC0.5SiC showed the lowest value of FWHM (1.86 ± 0.10) among the NCs. Figure 7.3(d) presents the equivalent circuit that closely matches the electrochemical behavior depicted in Figure 7.3(a to c). The impedance of the circuit that mimics the exact corrosion behavior of all the compositions is calculated from the equation:

$$Z = Z_{R_s} + \left(\frac{1}{Z_{R_l}+Z_L} + \frac{1}{\frac{Z_{R_F} Z_{CPE_F}}{Z_{R_C}+Z_C} + \frac{Z_{R_{DL}} Z_{CPE_{DL}}}{Z_{R_{DL}}+Z_{CPE_{DL}}}} \right)^{-1} \quad \text{Equation 7.2}$$

The fitted data corresponding to the elements shown in Figure 7.3(d) are summarized in Table 7.2. The values of solution resistance (R_s), were almost the same for all the materials tested (i.e.,10.91 to 11.28 Ω.cm^2). The element CPE represents the nonlinear capacitance with two components, Y and n. The magnitude of n ranges from 0 to 1. As the value of n is approaching 1, it represents a more capacitive nature of the element. In the present study, the CPE_{DL} is associated with the capacitance of the electric double-layer at the interface of the NaCl solution and working electrode. The CPE_F is associated with the capacitance of the corroded film. Further, the impedance of the component (Z_{CPE}) is calculated from the equation [131]:

$$Z_{CPE} = \frac{1}{Y(if)^n} \quad \text{Equation 7.3}$$

In the above equation, Y and n are the empirical parameters as described earlier, *f* represents the frequency, and $i = \sqrt{-1}$.

From Table 7.2, it is observed that the values of Y are inversely related to SiC_{np} wt.% in the AXM520 system, and accordingly, the values of $Z_{CPE_{DL}}$ and Z_{CPE_F} increases. The electronic double layer and corrosive film provided a higher resistance during charge transfer in NCs, which resulted in the superior corrosion inhibition property of the NCs. Furthermore, the resistances of the double layer (R_{DL}) and corroded film (R_F) also increased with the increase in SiC_{np}, indicating improved corrosion performance. It implies that the corrosive films were more inert in NCs compared to the AXM520 alloy, resulting in less dissolution of the α-Mg phase [129]. The series arrangement of inductance (L) and its resistance (R_L) represents the localized corrosion of the α-Mg phase. This is attributed to the poor stability and breaking of the $Mg(OH)_2$ film [132,133]. The values of L and R_L increased as the concentration of the SiC_{np}

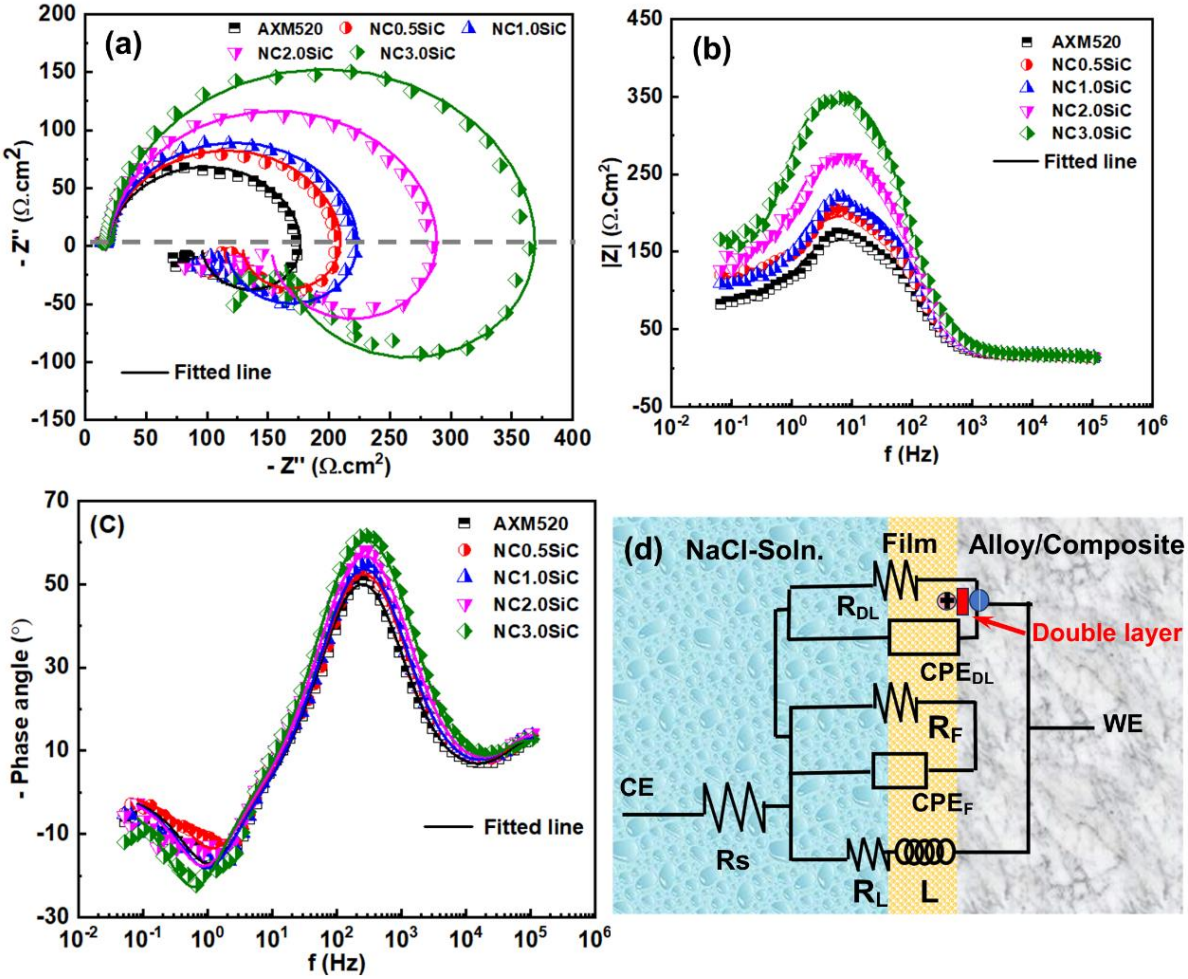

Figure 7.3 Presentation of (a) Nyquist plots, (b) impedance vs. frequency, and (c) phase angle vs. frequency Bode plots for AXM520 alloy and NCs; and (d) equivalent circuit for the observed EIS response.

increased, indicating the formation of a stable corrosion film on NCs. The polarization resistance (R_p) of the equivalent circuit is calculated using the following equation at $f = 0$ [128].

$$\frac{1}{R_p} = \frac{1}{R_F + R_{DL}} + \frac{1}{R_L} \quad \text{Equation 7.4}$$

The calculated values of R_p are enlisted in Table 7.2. The smallest magnitude of R_p for the AXM520 alloy indicates its highest corrosion rate. The values of R_p for the NCs were higher indicating their reduced corrosion rate than the alloy.

Table 7.2 Summary of the elements obtained from the equivalent circuit fitted with the experimental EIS data.

Materials	R_s ($\Omega.cm^2$)	R_{DL} ($\Omega.cm^2$)	CPE_{DL} ($F.cm^{-2}$)		R_f ($\Omega.cm^2$)	CPE_f ($F.cm^{-2}$)		R_L ($\Omega.cm^2$)	L ($H.cm^2$)	R_P ($\Omega.cm^2$)	OCP (mV)
			Y (10^{-7})	n		Y (10^{-5})	n				
AXM520	10.9±0.7	6.4±1.2	9.2±0.8	0.93±0.02	154.8±6.2	2.3±0.7	0.93±0.07	160.9±9.5	30.1±0.3	80.5	-1559.7 ± 4.8
NC0.5SiC	10.9±0.4	6.5±0.9	8.9±0.3	0.91±0.03	183.9±9.5	1.9±0.3	0.93±0.06	202.5±9.1	37.6±1.2	98.1	-1538.2 ± 5.3
NC1.0SiC	9.1±1.2	7.3±0.4	7.6±0.2	0.84±0.01	198.1±2.4	1.7±0.5	0.94±0.04	216.4±17.9	40.1±2.7	105.3	-1511.5 ± 2.7
NC2.0SiC	10.3±0.9	8.9±1.0	5.2±0.8	0.94±0.02	263.8±1.6	1.5±0.8	0.92±0.05	246.1±10.7	59.3±3.2	129.3	-1474.3 ± 6.7
NC3.0SiC	11.2±0.6	10.1±1.1	4.9±0.5	0.96±0.01	344.1±2.1	1.2±0.3	0.93±0.01	262.0±6.1	76.1±5.8	150.6	-1453.1 ± 5.3

7.4 Potentiodynamic polarization test

Figure 7.4(a) presents the Tafel plots obtained from the potentiodynamic polarization tests of the as-cast AXM520 and its NCs. The corrosion rate (mm/yr), I_{corr}, and E_{corr} were calculated from Figure 7.4(a), and their variations as a function of SiC_{np} concentration are revealed in Figure 7.4(b). The E_{corr} shifted to a more positive value, whereas the I_{corr} values dropped significantly as wt.% of dispersed SiC_{np} increased in AXM520 alloy. The corrosion rate of AXM520 alloy was highest, i.e., 0.58 ± 0.02 mm/yr. The corrosion rate of the NCs was lower than the alloy. The NC0.5SiC had a corrosion rate of 0.49 ± 0.03 mm/yr, which is highest among the NCs. The NC1.0SiC and NC2.0 exhibited a corrosion rate of 0.19 ± 0.07 and 0.11 ± 0.05 mm/yr, respectively. The NC3.0SiC showed 91.3 % (0.05 ± 0.01 mm/yr) improvement in contrast to the corrosion rate of AXM520 alloy. Thus, the additions of SiC_{np}

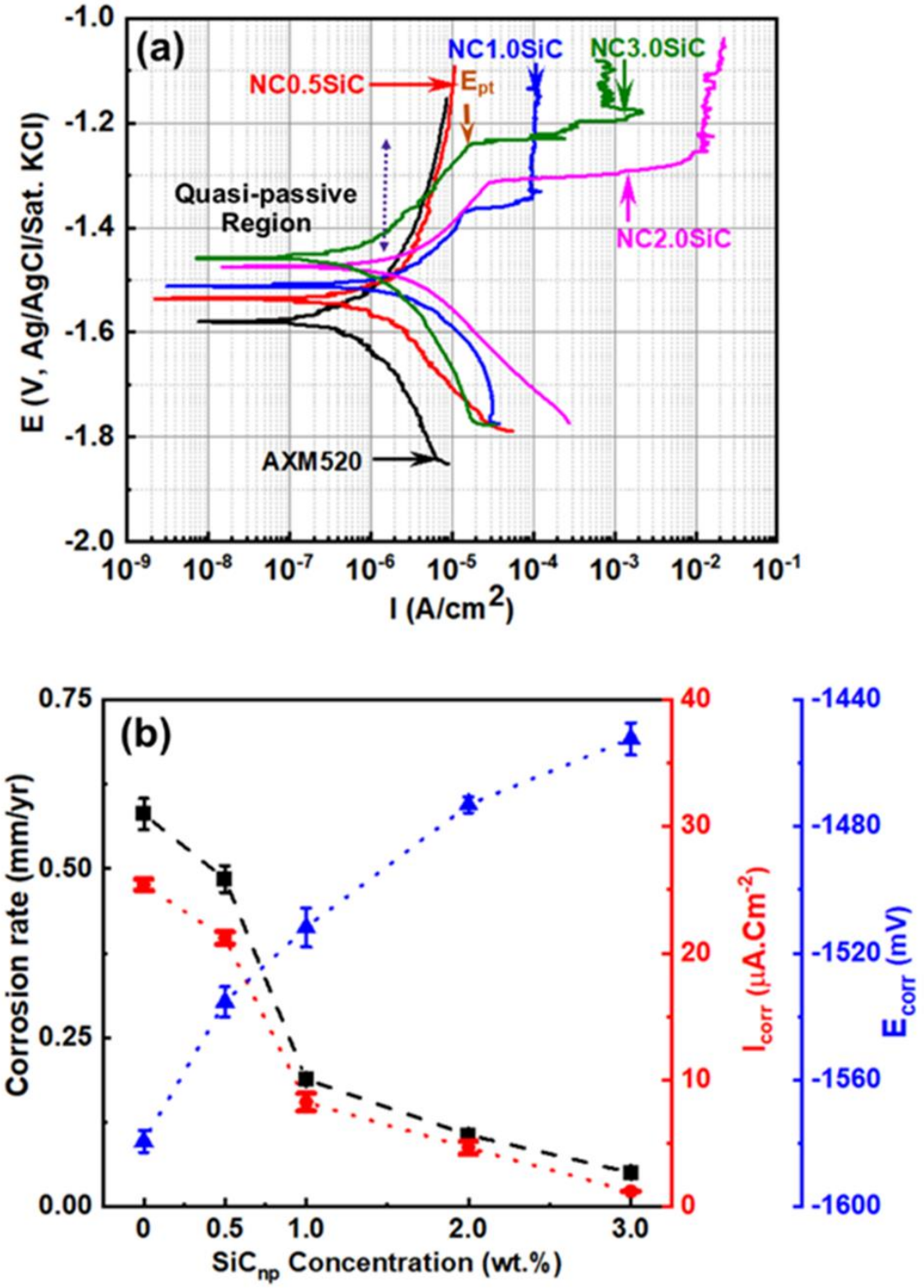

Figure 7.4 (a) Potentiodynamic polarization curves; (b) the variation of calculated Icorr, $E_{corr,}$ and corrosion rates with SiC_{np} concentration for the AXM520 alloy and NCs.

significantly inhibited the corrosion of AXM520 alloy. The improved corrosion rate of Mg alloys owing to nanoparticle addition was reported earlier as well [44,126]. Most interestingly, the anodic branch of the NC1.0SiC, NC2.0SiC, and NC3.0SiC exhibited nobler pitting breakdown potential (E_{pt}) as compared to the AXM520 and NC0.5SiC. After E_{pt} potential, all the curves exhibited a rapid increase in current density, indicating the breakdown of the semi-protective film and the rapid dissolution of the α-Mg phase. The difference between E_{corr} and E_{pt} of NC1.0SiC, NC2.0SiC, and NC3.0SiC were 141.4 ± 5.4, 173.14 ± 2.3, and 215.3 ± 2.6, respectively. The results again confirm that the resistance against pitting corrosion increased as the SiC_{np} concentration increased in the AXM520 alloy.

7.5 Volta potential measurement

The results of the hydrogen evolution tests and electrochemical corrosion tests signify that the dispersion of SiC_{np} significantly inhibited the corrosion of AXM520 alloy. Therefore, the volt potential difference between α-Mg and C36 in AXM520 alloy as well as NC3.0SiC was quantified to understand the corrosion behavior. Figure 7.5(a to d) exhibits the SKPFM results obtained from AXM520 alloy and NC3.0SiC. Figure 7.5(a and c) exhibits the volta potential maps, and Figure 7.5(b and d) portrays the variation of volta potential as a distance along the lines marked in the former images. The difference in potential between α-Mg and C36 phases at the grain boundaries was 85.29 ± 1.52 mV in AXM520, as shown in Figure 7.5(a and b). Metalnikov et al. [134] showed that the potential difference between these two phases was 140 mV in AXM610 alloy. Baek et al. [135] studied the corrosion behavior of the AZ61 with varying Ca wt.%. They reported that the potential difference between primary α-Mg and secondary C36 phase was 230 mV in AZX611 alloy. Thus, the alloy composition significantly alters the volta potential difference between the two constituent phases. In NC3.0SiC, the potential of the C36 phase was 36.95 ± 1.13 mV higher than the α-Mg phase, as displayed in Figure 7.5(c and d). The decrease in the volta potential difference was owing to the dispersion of SiC_{np} in the α-Mg phase. A significant amount of SiC_{np} was engulfed by the α-Mg phase during solidification of the NCs. Thus, the potential of the α-Mg phase is reduced by 1.6 times in the NC3.0SiC compared to that in the AXM520 alloy. The addition of nanoparticles increased the viscosity of the melt [90,91], which decreased the solid-liquid interface velocity during solidification. The decreased interface velocity entrapped a higher amount of SiC_{np} in the grain boundaries along with the C36 phase, as shown in Figure 4.7(c). These entrapped SiC_{np} in the intergranular region hindered the charge transfer between the α-Mg and C36 phases

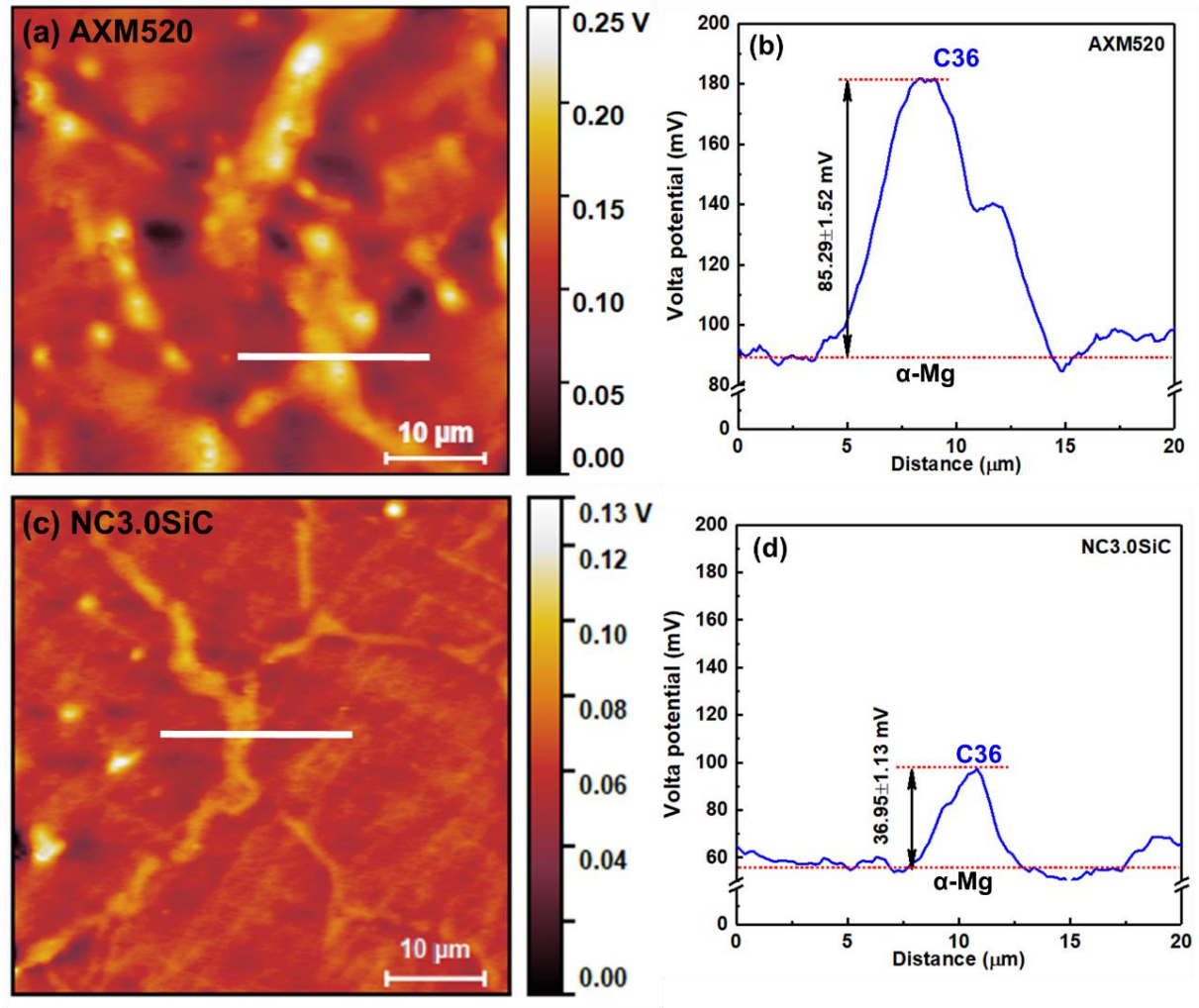

Figure 7.5 Volta potential maps for (a) AXM520 and (c) NC3.0SiC; the variation of volta potential (b and d) across the lines marked in 'a' and 'c' exhibiting the potential difference between α-Mg and $(Mg,Al)_2Ca$ (C36) phases.

owing to the poor conductivity of the SiC_{np}. Therefore, the reduced volta potential difference led to slower charge transfer between the α-Mg and C36 phase in NCs, which essentially improved the corrosion resistance of NCs with respect to AXM520 alloy. The aforementioned results further confirm the increased impedance resistance (L) in the NCs, as listed in Table 7.2. Ganguly et al., in two separate studies, concluded that adding SiC_{np} or graphene nanoparticles decreased volta potential values between α-Mg and β-$Mg_{17}Al_{12}$ phases in AZ91-based alloys, resulting in the better corrosion properties of the NCs compared to the monolithic alloy [44,126].

7.6 Characterization of corrosion film

7.6.1 SEM micrographs of corroded film

Figure 7.6(a to e) exhibits the SEM micrographs of the corroded film formed on the contact surface of AXM520 alloy and NCs following the electrochemical tests. The film primarily consists of $Mg(OH)_2$ (as confirmed by the XRD patterns discussed in section 7.6.2) which is insoluble in an aqueous medium [124,125]. The Cl^- ions in the aqueous NaCl solution attacked the $Mg(OH)_2$ layer and formed the soluble $MgCl_2$, which deteriorated the protective layer. Figure 7.6(a) exhibits the corrosion layer formed on the AXM520 alloy. The presence of excessive cracks on the corroded film is observed. However, the cracks were shallower and less visible in the NCs, as exhibited in Figure 7.6(b to e). As a result, the quantity of $Mg(OH)_2$ phase formed reduced as the SiC_{np} wt.% gradually enriched in the NCs. The EDS results obtained from the corroded films of the AXM520 alloy and NC3.0SiC are shown in Figure 7.7(a to d). It is evident that the corroded film on the NC3.0SiC contains relatively higher Al (i.e., 7.05 wt.%) than that (0.83 wt.%) of the AXM520 alloy. The higher Al content on the corrosion film of the NC3.0SiC was attributed to the higher Al content in the α-Mg phase, as discussed earlier in section 4.1 of chapter 4.

7.6.2 XRD and FTIR analysis of the corroded products

Figure 7.8(a) exhibits the XRD profile of the collected corroded products from the top of the corrosion-tested AXM520 and NCs. The presence of $Mg(OH)_2$ compound in the corrosion films of the tested alloy and NCs is confirmed. The XRD peaks corresponding to the parent α-Mg were also observed. The reaction leading to the formation of $Mg(OH)_2$ was discussed in Equation 7.1. The $MgCO_3.3H_2O$ (nesquehonite) phase was also identified in the XRD peaks of all the samples. The formation of the compound indicates that atmospheric CO_2 also plays

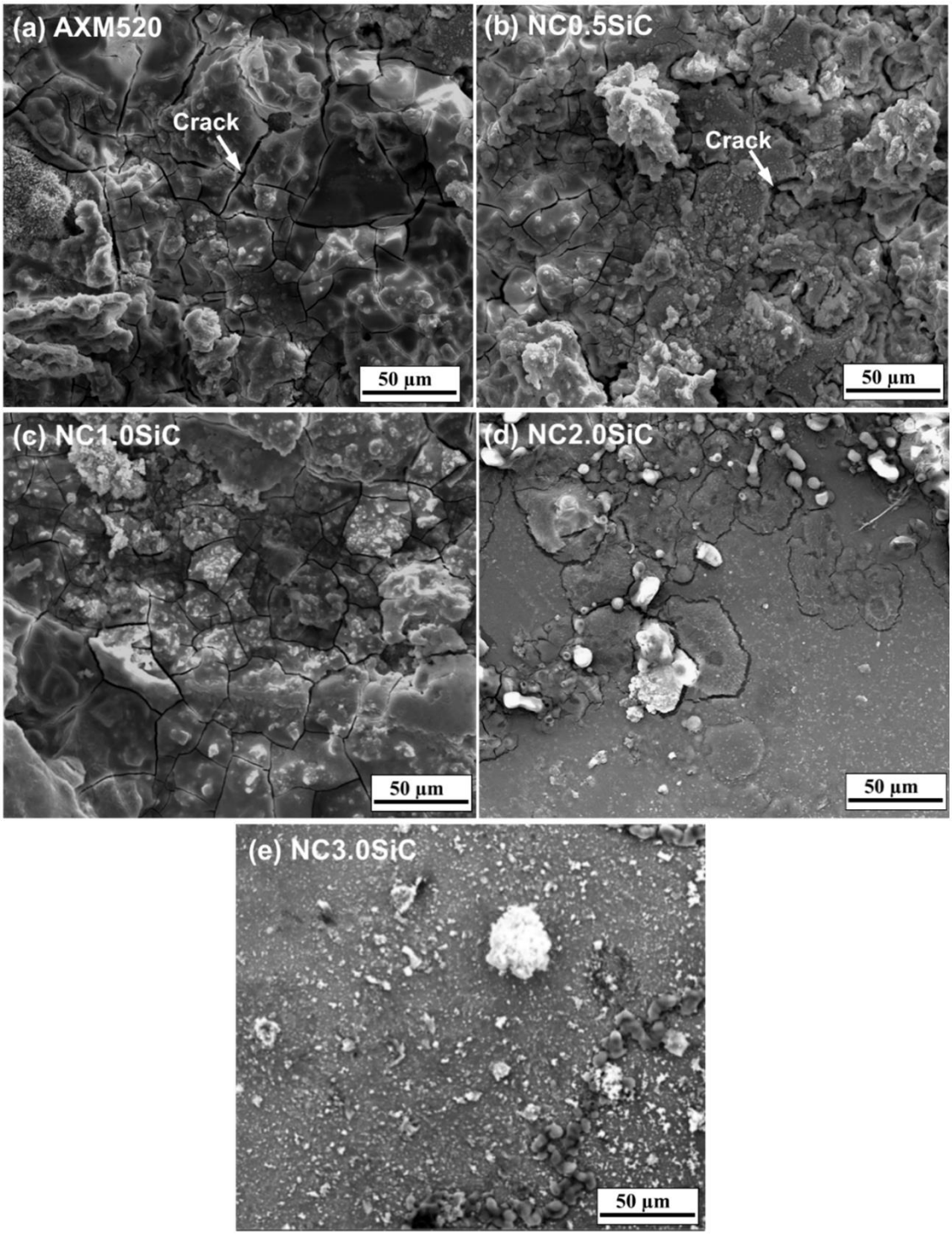

Figure 7.6 SEM images of the corrosion films formed on the surfaces of AXM520 (a) and NCs (b to e).

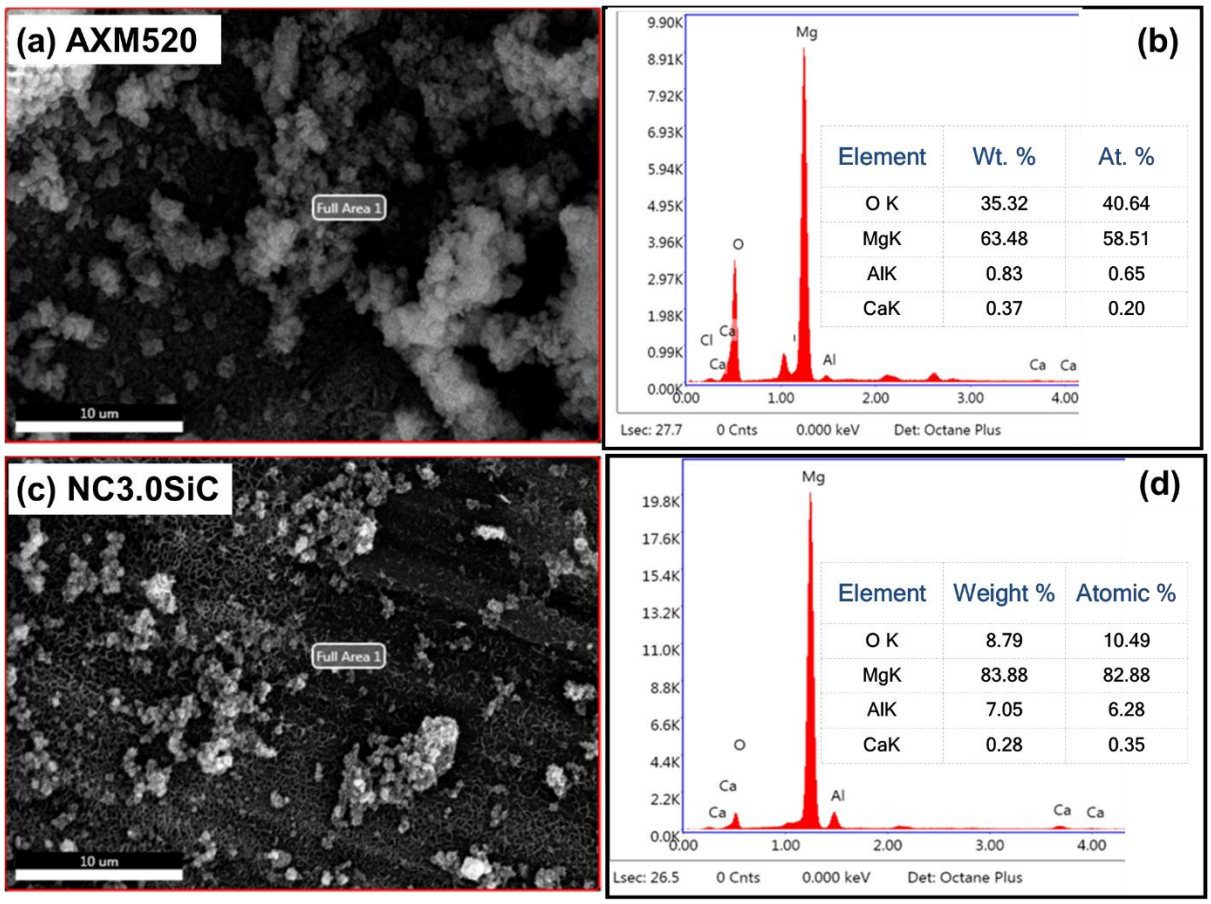

Figure 7.7 EDS results obtained from the corroded films of the AXM520 alloy (a and b) and NC3.0SiC (c and d) confirming the higher Al content on the corrosion film of the NC3.0SiC.

a significant part in the corrosion of Mg-based alloys and NCs. The CO_2 in the atmosphere reacted with $Mg(OH)_2$ as per the reaction [125,126].

$$Mg(OH)_2 + CO_2 \rightarrow MgCO_3 + H_2O \quad \text{Equation 7.5}$$

Further, $MgCO_3$ combined with H_2O present in the aqueous NaCl solution formed $MgCO_3.3H_2O$. In addition, the Layered Double Hydroxide (LDH) was also detected on the corroded films of the alloy and NCs. The LDH formation took place owing to the increased pH (~11.2) of the electrolyte [136,137]. The pH of the electrolyte increased by the dissolution of $Mg(OH)_2$ from the corroded films. Furthermore, the increase in the peak intensity of the LDH phase was attributed to the increased Al content in the α-Mg phase of the NCs. The increased LDH content resulted in an increase in the charge transfer resistance of the corroded films and was confirmed earlier by the increased corroded film resistance by EIS measurement. Thus, the increased LDH content in the corroded film might acted as a quasi-passive film on the surface of the NCs. The presence of amorphous compounds was not detected in the XRD pattern. Therefore, the possibility of formation of such compounds was checked with FTIR and XPS. Figure 7.8(b) presents the FTIR spectra recorded from the corroded film from as-cast AXM520 and NCs. The intensity of the peaks associated with the different functional groups decreased with the higher content of SiC_{np} in the as-cast AXM520 alloy. The strong peak corresponding to 3694 cm^{-1} signifies the presence of the stretching vibration mode of Mg-OH [138]. The occurrence of the bond further confirms the formation of $Mg(OH)_2$. Next to the Mg-OH band, a broad band of OH^- was also observed. The bond extended in the wave range of 3653 cm^{-1} to 2968 cm^{-1}. The intensity of the peak decreased significantly as the dispersed SiC_{np} increased in the AXM520 alloy. The band at 1641 cm^{-1} resembles to the bending vibration mode of the absorbed water molecules [139]. The peak at 1420 cm^{-1} presents a C-O vibration band of carboxyl groups [140]. The band at 645 cm^{-1} agrees with the stretching vibration mode of the Mg-C bond, confirming the presence of $MgCO_3$-type compounds [141].

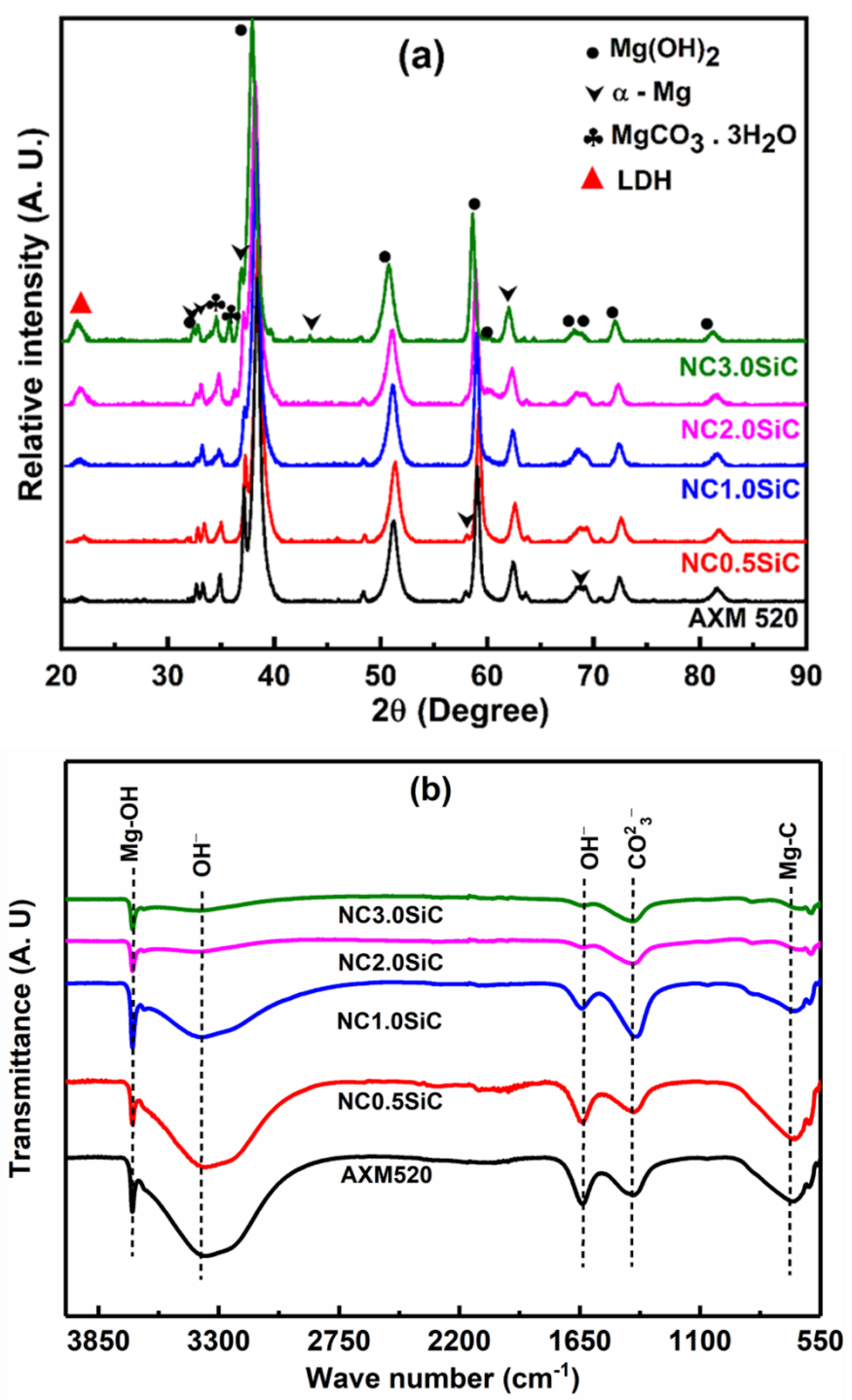

Figure 7.8 (a) XRD and (b) FTIR profiles recorded from the corroded films of all the materials tested.

7.6.3 XPS analysis

Figure 7.9(a to f) exhibits the XPS analysis acquired from the corrosion film of fabricated AXM520 and NC3.0SiC. The peaks corresponding to Mg 1s acquired from the AXM520 and NC3.0SiC are displayed in Figure 7.9(a and b), respectively. The analysis of the results shows the occurrence of $Mg(OH)_2$ and $MgCO_3$ in the corroded film. The details of the peaks are summarized in Table 7.3. The $Mg(OH)_2$ peak was observed at 1302.8 eV whereas, the peak of $MgCO_3$ was observed at 1303.7 eV. The analysis showed that the area fraction of $Mg(OH)_2$ was much higher in the corroded film of AXM520 than in the corroded layer on NC3.0SiC. Furthermore, the analysis of Al 2p peaks confirmed the presence of $Al(OH)_3$ and Al_2O_3 at 73.8 and 70.3 eV, respectively, in both the AXM520 alloy and NC3.0SiC, as displayed in Figure 7.9(c and d). The increased peak area of the $Al(OH)_3$ was might contributed by the Al-LDH layer formation, which significantly improved the corrosion resistance of the NCs. However, there is no significant change in the peaks corresponding to Ca 2p acquired from the corrosion films of AXM520 alloy and NC3.0SiC nanocomposite, as shown in Figure 7.9(e and f) [127].

Thus, the addition of SiC_{np} in the AXM520 alloy decreased the amount of corrosion products. The reduced amount of $Mg(OH)_2$ lowered the formation of $MgCl_2$. The $Al(OH)_3$ and Al-LDH layer is more stable than $Mg(OH)_2$. Thus, the stable corroded film containing more $Al(OH)_3$ and Al-LDH improved the corrosion resistance of the NCs by preventing Cl^- ions attack on the $Mg(OH)_2$ layer.

Table 7.3 Summary of the area percentage data evaluated from the XPS peaks of AXM520 and NC3.0SiC after deconvoluting.

Materials	**Mg 1s**		**Al 2p**		**Ca 2p**	
	$MgCO_3$ (1303.7 eV)	**$Mg(OH)_2$** (1302.8 eV)	**$Al(OH)_3$** (73.8 eV)	**Al_2O_3** (70.3 eV)	**CaO** (354.5 eV)	**$Ca(OH)_2$** (351.7 eV)
AXM520	25.0	70.9	26.6	73.4	5.2	94.8
NC3.0SiC	42.1	57.9	50.6	49.5	5.8	94.2

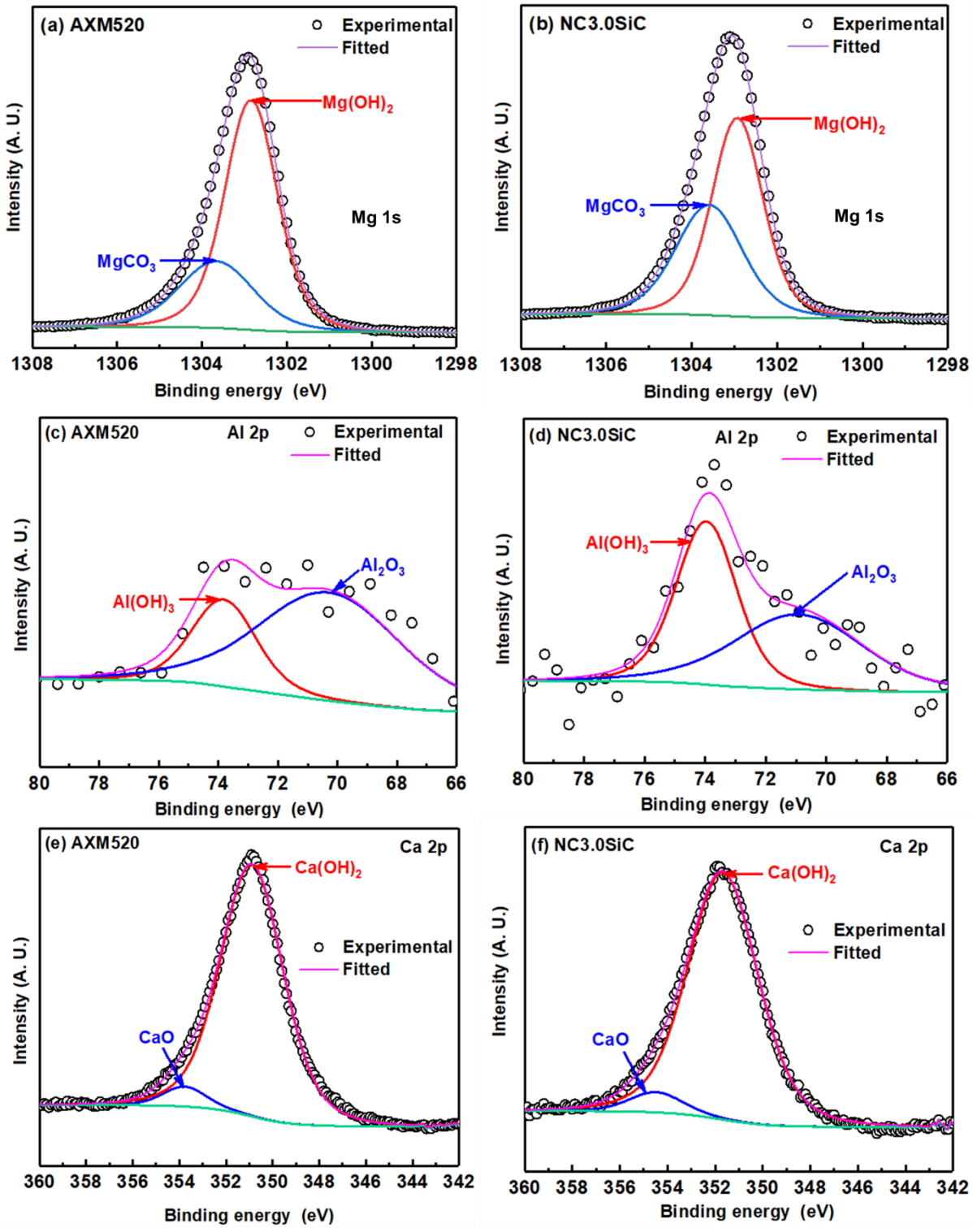

Figure 7.9 XPS spectra acquired from the corroded films of AXM520 (a, c, e) and NC3.0SiC (b, d, f).

7.7 Characterization of corroded surfaces

The corroded surfaces of as-cast AXM520 and NCs were analyzed after removing the corroded film with a standard chromate solution. Figure 7.10(a to e) shows the topological map of the corroded surfaces of AXM520 and NCs after the removal of accumulated corroded films. The results were subsequently analyzed using Gwyddion software to estimate the roughness of the corroded surfaces. The roughness values of all the compositions as a function of SiC_{np} are shown in Figure 7.10(f). The roughness values of the corroded surfaces inversely varied with respect to the SiC_{np} wt.% in AXM520 alloy. The AXM520 alloy showed the highest roughness value of 17.7 ± 2.7 μm among the compositions. The roughness value of the NC0.5SiC, i.e., 14.2 ± 4.9 μm, was the highest among the NCs. The lowest roughness value i.e., 3.1 ± 1.3 μm, was for NC3.0SiC. Therefore, adding 3.0 (wt.%) of SiC_{np} in as-cast AXM520 alloy reduced the corroded surface roughness of AXM520 alloy by 82.5%.

Figure 7.11(a) depicts the corroded surface of the as-cast AXM520 alloy observed under SEM. The elemental mapping related to Figure 7.11(a) is displayed in Figure 7.11(b). The image confirms that certain regions were deeply corroded, and these regions are surrounded by boundary walls. The deeply corroded regions corresponded to the primary α-Mg phase, and the boundary walls were the secondary C36 phase, as confirmed in the elemental mapping. This suggests that galvanic corrosion occurred between these phases. Thus, the α-Mg phase acted as an anode while the C36 phase at the interfaces of different grains acted as a cathode during the galvanic corrosion. The morphologies of the corroded surfaces in the NCs are shown in Figure 7.11(c to f). The depth of the corroded α-Mg phase reduced significantly with the higher content of SiC_{np} wt.% in as-cast AXM520 alloy. The relative potential between these two phases is reduced with the increased SiC_{np} wt.% in the NCs, which subsequently reduced the galvanic corrosion rate and improved the corrosion resistance of as-cast NCs. Figure 7.12(a and b) exhibits the cross-sectional views of the AXM520 alloy and NC3.0SiC after the removal of the corrosion products. The depth of the corroded layer in the AXM520 alloy (i.e., 164.6 μm) is 2.9 times higher than that (i.e., 57.4 μm) in the NC3.0SiC confirming the severe corrosion of the AXM520 alloy as compared to the NCs.

The schematics of the corrosion mechanism involved in the as-cast AXM520 and NC3.0SiC (representative for the NCs) are presented in Figure 7.13(a and b). In stage I, the $Mg(OH)_2$-rich corrosion film formed on the AXM520 alloy, as depicted in Figure 7.13(a). The $Mg(OH)_2$ film

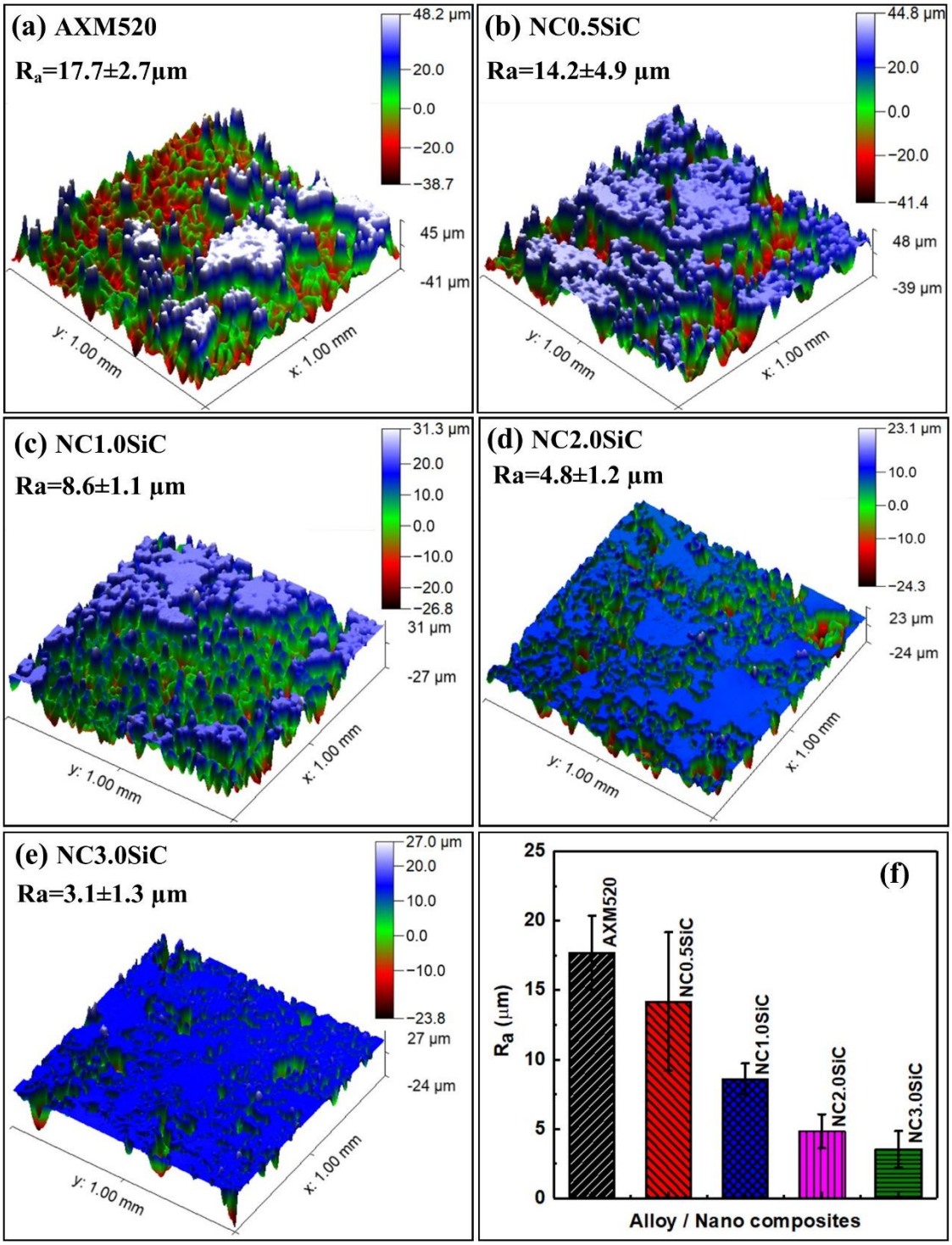

Figure 7.10 3D presentation of corrosion products free surface morphologies of AXM520 (a) and NCs (b to e); summary of surface roughness values (f).

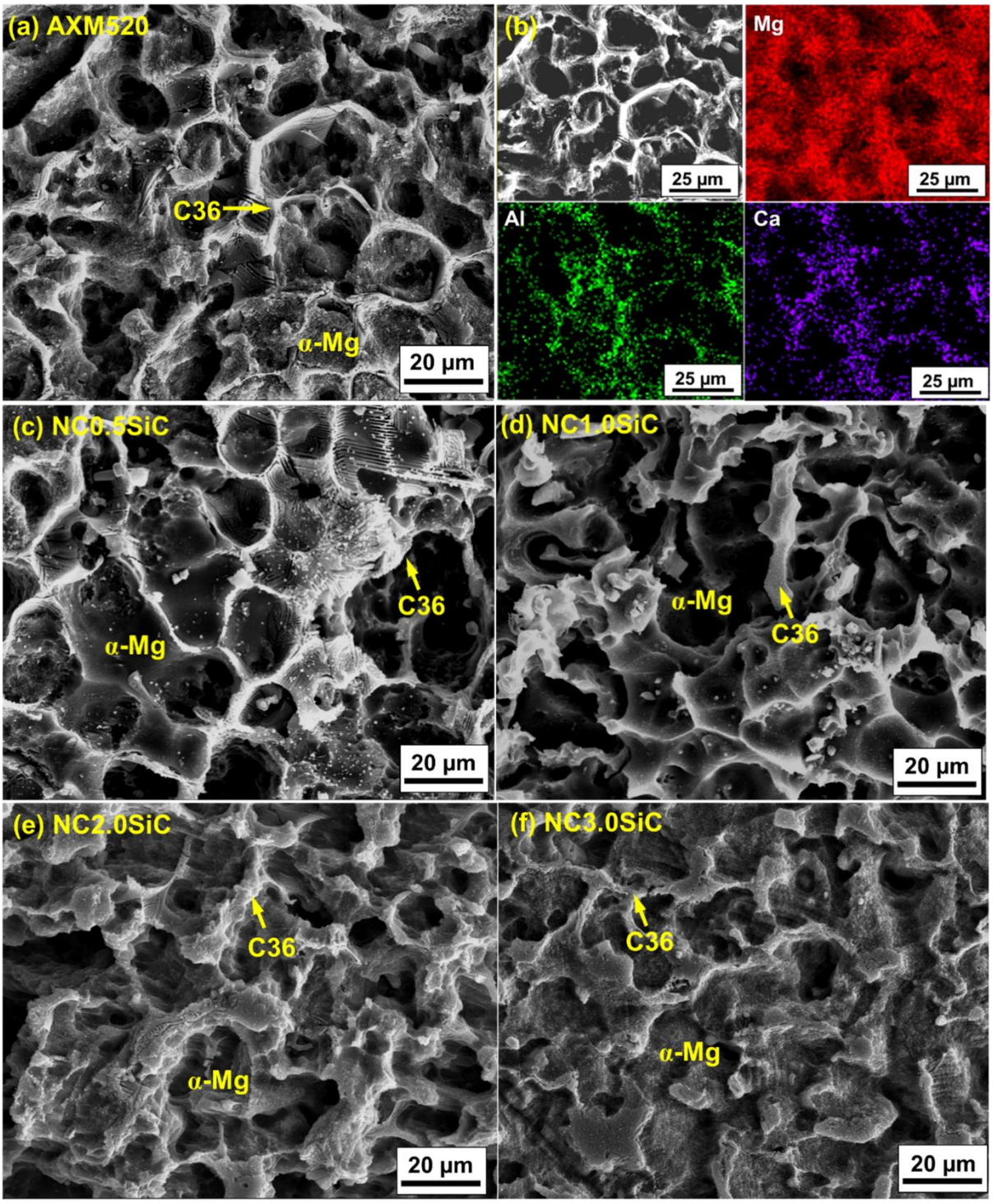

Figure 7.11 SEM micrographs of corrosion products free surfaces of AXM520 with elemental mapping (a and b), and NCs (c to f).

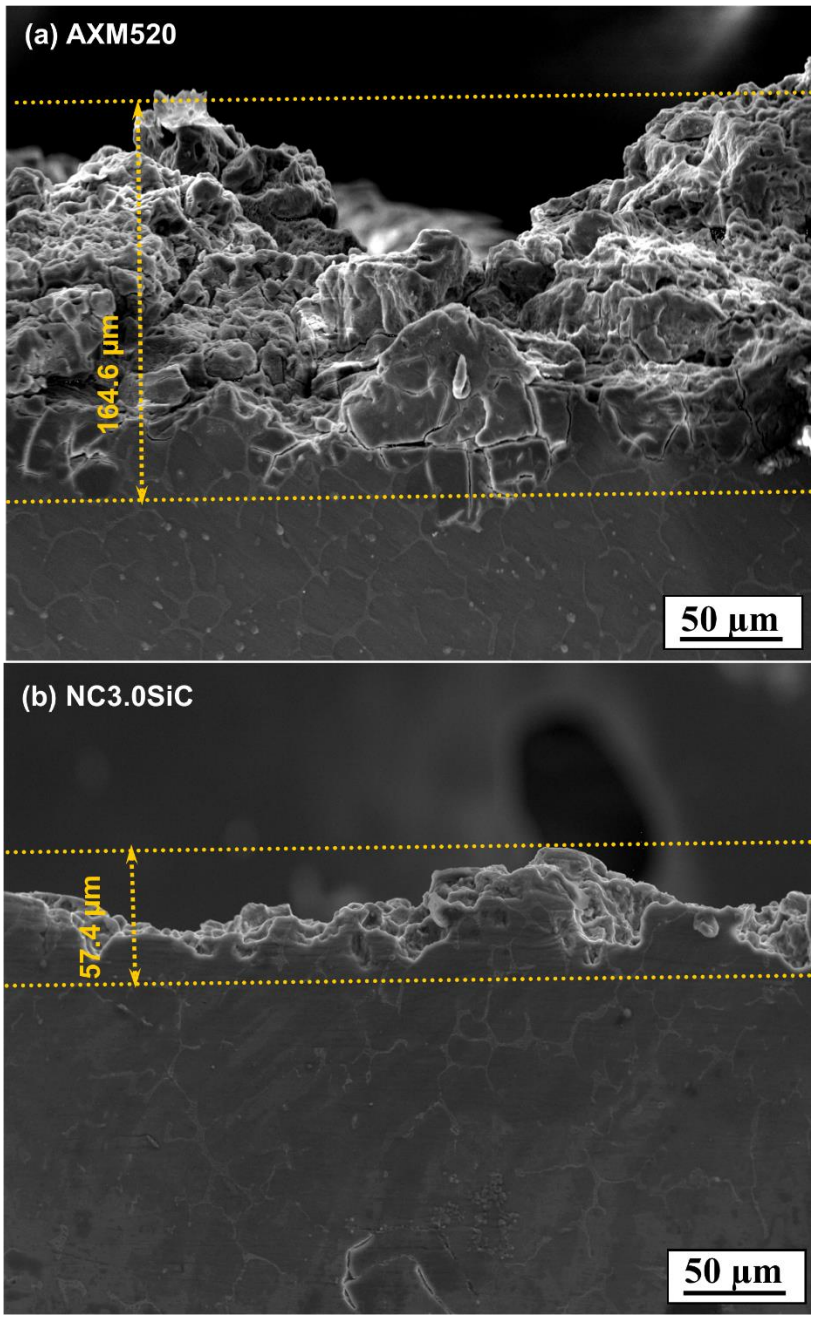

Figure 7.12 Cross-sectional micrographs of the corroded surfaces of the (a) AXM520 alloy and (b) NC3.0SiC depicting the extent of corrosion.

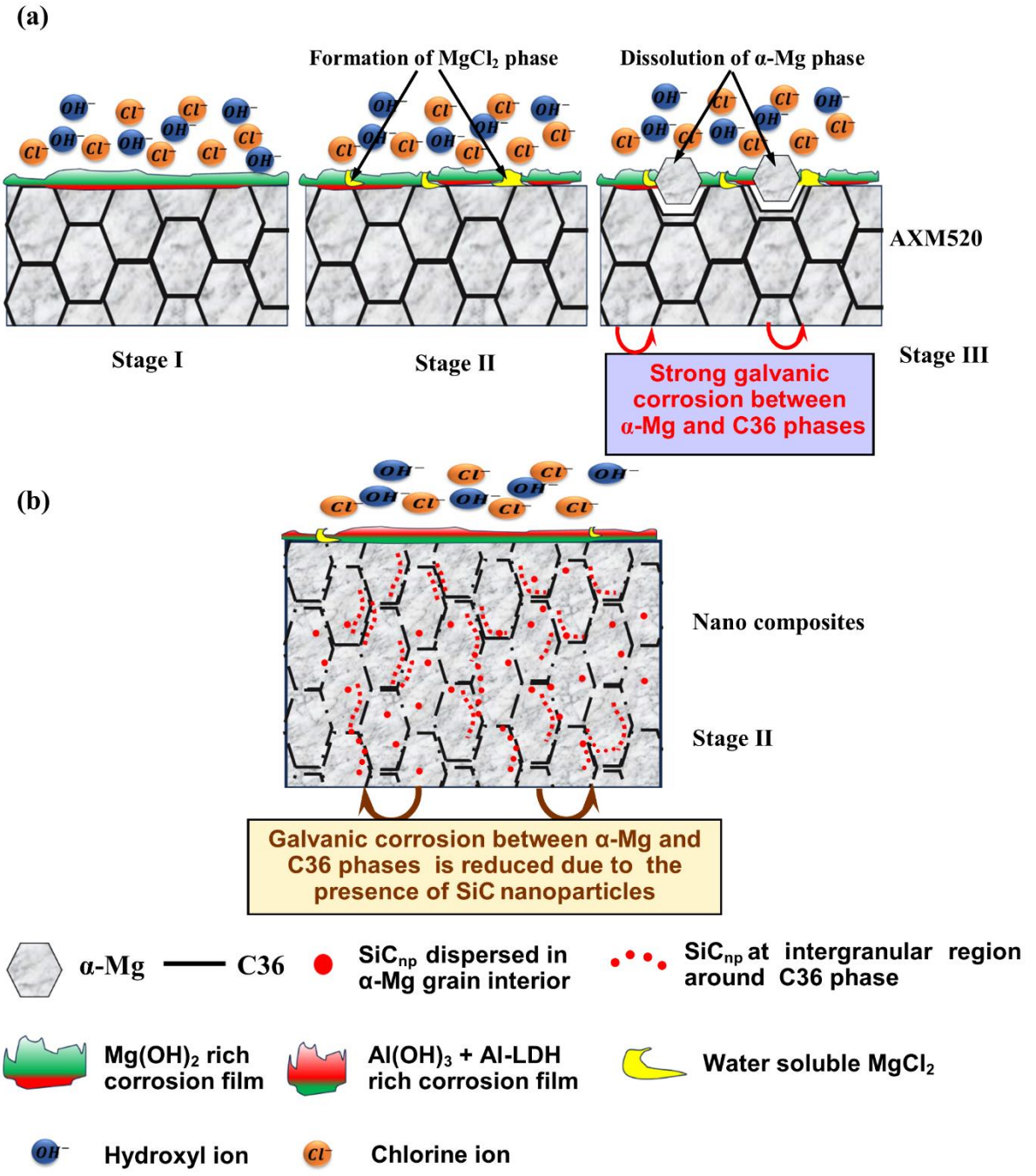

Figure 7.13 Schematic representation showing the different stages of corrosion mechanism took place in (a) AXM520, and (b) NC3.0SiC.

was attacked by Cl^- ion present in the NaCl solution and aqueous soluble $MgCl_2$ formed in stage II. Thus, the $Mg(OH)_2$ film became unstable. In stage III, the dissolution of the α-Mg phase took place due breaking of $Mg(OH)_2$ layer. However, the reduced volta potential difference between α-Mg and C36 phases minimized the extent of galvanic corrosion in NC3.0SiC. The reduced volta potential between α-Mg and C36 is attributed to the formation of non-conducting SiC_{np} layer around the C36 phase, that leads to decrease galvanic potential between α-Mg and C36 phase, as discussed earlier in section 7.5. For the NC3.0SiC, the amount of formation of $Mg(OH)_2$ is reduced, and accordingly the $Al(OH)_3$ and Al-LDH-rich corroded film is formed, as shown in Figure 7.13(b). The Al-LDH-rich film is more stable than the $Mg(OH)_2$-rich film contributing to better corrosion resistance of the NCs.

7.8 Summary of chapter 7

In this chapter, the corrosion behavior of squeeze-cast Mg-5.0Al-2.0Ca-0.3Mn (wt.%) (AXM520) alloy and nanocomposites are presented. The major findings from the current chapter are summarized below.

i. The corrosion resistance of the NCs measured in the hydrogen evolution test was superior to the AXM520 alloy, and the improvement was 91.1% in the NC3.0SiC.

ii. The OCP of all NCs shifted to more noble values with the increased quantity of SiC_{np} in AXM520. The polarization resistance determined from the EIS increased with the increase in the SiC_{np} content in the NCs.

iii. The potentiodynamic polarization scans further confirmed the superior corrosion resistance of the NCs to the AXM520 alloy. Among the fabricated NCs, NC3.0SiC exhibited the highest corrosion resistance, and it was 91.3% lower in comparison to the AXM520 alloy.

iv. The corrosion products predominantly consist of $Mg(OH)_2$. The addition of SiC_{np} reduced the formation of $Mg(OH)_2$ and increased the content of the $Al(OH)_3$ in the NCs leading to the higher stability of the corroded film formed on them.

v. The α-Mg phase was severely damaged owing to the galvanic corrosion between the α-Mg and C36 phases. However, the galvanic corrosion was reduced due to a decrease in the volta potential between α-Mg and C36 phases in the NCs, resulting in their superior corrosion resistance.

Chapter 8

Creep Behavior of Age-hardened AXM520 Alloy and NCs

The present chapter aims to explore the microstructural alteration and creep characteristic of the squeeze-cast age-hardened Mg-5.0Al-2.0Ca-0.3Mn (AXM520HT) alloy, as well as AXM520HT+1.0SiC (NC1.0SiCHT) and AXM520HT+2.0SiC (NC2.0SiCHT) (wt.%) nanocomposites (NCs). A correlation of the creep responses of age-hardened AXM520 alloy and its nanocomposites with their initial and creep-deformed microstructures has been established. For the first time, deformation mechanism maps for Mg-Al-Ca alloys and their nanocomposites are constructed. A summary of the microstructures and creep responses of AXM520HT, NC1.0SiCHT and NC2.0SiCHT, is presented at the end of this chapter.

8.1 Hardness response of aged AXM520 alloy and NCs

The AXM520HT alloy, as well as NC1.0SiCHT and NC2.0SiCHT nanocomposites, were subjected to aging at 523 K, and their age-hardening responses were examined by evaluating the microhardness values, as shown in Figure 8.1(a). As anticipated, the values of Vickers hardness of the AXM520HT alloy and its nanocomposites gradually increase with the aging time. The highest hardness responses of the alloy and nanocomposites were achieved following 2 hr of aging at 523 K. The microhardness values then decreased with a further increase in the aging time, confirming over aging of the specimens. At the peak aged condition, the AXM520HT alloy exhibited a hardness of 71.7±1.6 HV, and the values for the NC1.0SiCHT and NC2.0SiCHT were 75.8±2.4 HV and 79.9±1.3 HV, respectively. The hardness values of the alloy and NCs in as-cast conditions were 50.9±2.3, 53.4±1.2, and 56.8±2.2, respectively. Thus, the hardness values of the AXM520HT, NC1.0SiCHT, and NC2.0SiCHT are improved by 40.9, 41.9, and 40.7 %, respectively following aging. The significant improvement in hardness values confirms the beneficial effects of aging.

8.2 Microstructural characterization of aged AXM520 and NCs

The XRD patterns displayed in Figure 8.1(b) correspond to the aged AXM520HT alloy, and nanocomposite samples confirmed the presence of the primary α-Mg phase, i.e., the solid solution of Al, Ca, and Mn in Mg. The solubilities of Al and Ca in Mg at room temperature are limited, and therefore, different intermetallic phases inevitably formed in the AXM520HT alloy. The recorded XRD profile exhibited the characteristics peaks of the $(Mg,Al)_2Ca$ (C36), Al_2Ca (C15), and Al_8Mn_5 intermetallic phases, as shown in the enlarged view of the XRD patterns in Figure 8.1(c). A small peak associated with the SiC phase was observed in NC2.0SiCHT, which confirms the presence of the SiC nanoparticles in the NCs. The SEM micrograph of the AXM520HT alloy at peak-aged conditions in Figure 8.2(a) exhibits the primary α-Mg phase in a dark gray appearance. The C36 phase formed a lamellar morphology with α-Mg phase, i.e., a binary eutectic at the grain boundaries and triple junctions. Another white spherical phase was observed at the α-Mg grain interior. The magnified view of 'a' in Figure 8.2(b) depicts that the C36 phase is discontinuous. Liu et al., in their investigation, showed that the secondary phase became more discontinuous and fragmented in the AXM alloys with increased heat treatment time [142]. A similar morphological change in the secondary phase of the AXM alloys with solutionizing time was reported by Inoue et al. [143]. Figure 8.2(c) presents a magnified micrograph of the AXM520HT alloy, and the corresponding elemental mapping shown in Figure 8.2(d) confirms that the grain boundary phase was enriched with Al and Ca. In addition, the Al and Mn-rich spherical white particles were observed. The EDS analysis results shown in Figure 8.2(e), i.e., Mg-5.0Al-2.4Ca (at.%) taken from the dark gray region, confirm the matrix phase is constituted of α-Mg. The composition of the phase at the grain boundary shown in Figure 8.2(f) was Mg-30.7Al-14.6Ca (at.%), ensuring the formation of the C36 phase. Suzuki et al. [54] reported the morphological alteration of the C36 phase in the AXM-based alloys aged at 573 K for 3600 s. The EDS data obtained from the white spherical particles shown in Figure 8.2(g), i.e., Mg-46.3Al-43.3Mn (at.%), confirms the phase is Al_8Mn_5. Li et al. [56] and Han et al. [52] also confirmed the existence of the Al_8Mn_5 phase, with similar composition in the AXM4204 and AX52 alloys. The micrographs of the aged NC2.0SiCHT in Figure 8.2(h and i) exhibit the fragmented topology of the C36 phase present in it. The discontinuous lamellas of the C36 phase were attributed to a complex solidification process of the melt involved in the presence of solid SiC nanoparticles. In the presence of nanoparticles, the migration of solute atoms from the solid to liquid phase is strongly hindered [96,144]. Therefore, the heterogeneous nucleation site

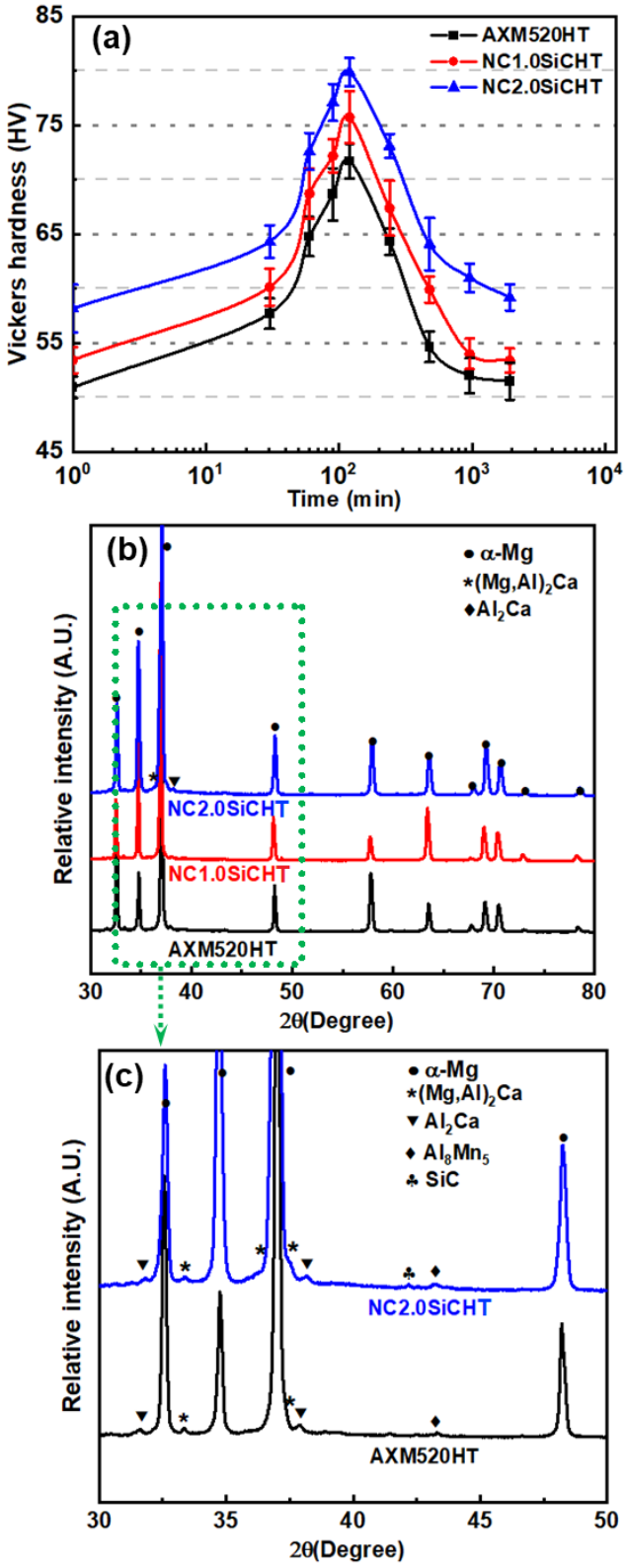

Figure 8.1 (a) Variation of hardness values with aging time for AXM520HT and NCs; (b) XRD pattern acquired from the peak-aged AXM520HT and NCs; (c) magnified view of the 2θ range from 30 to 50 ° for the XRD patterns shown in 'b' for AXM520HT and NC2.0SiCHT.

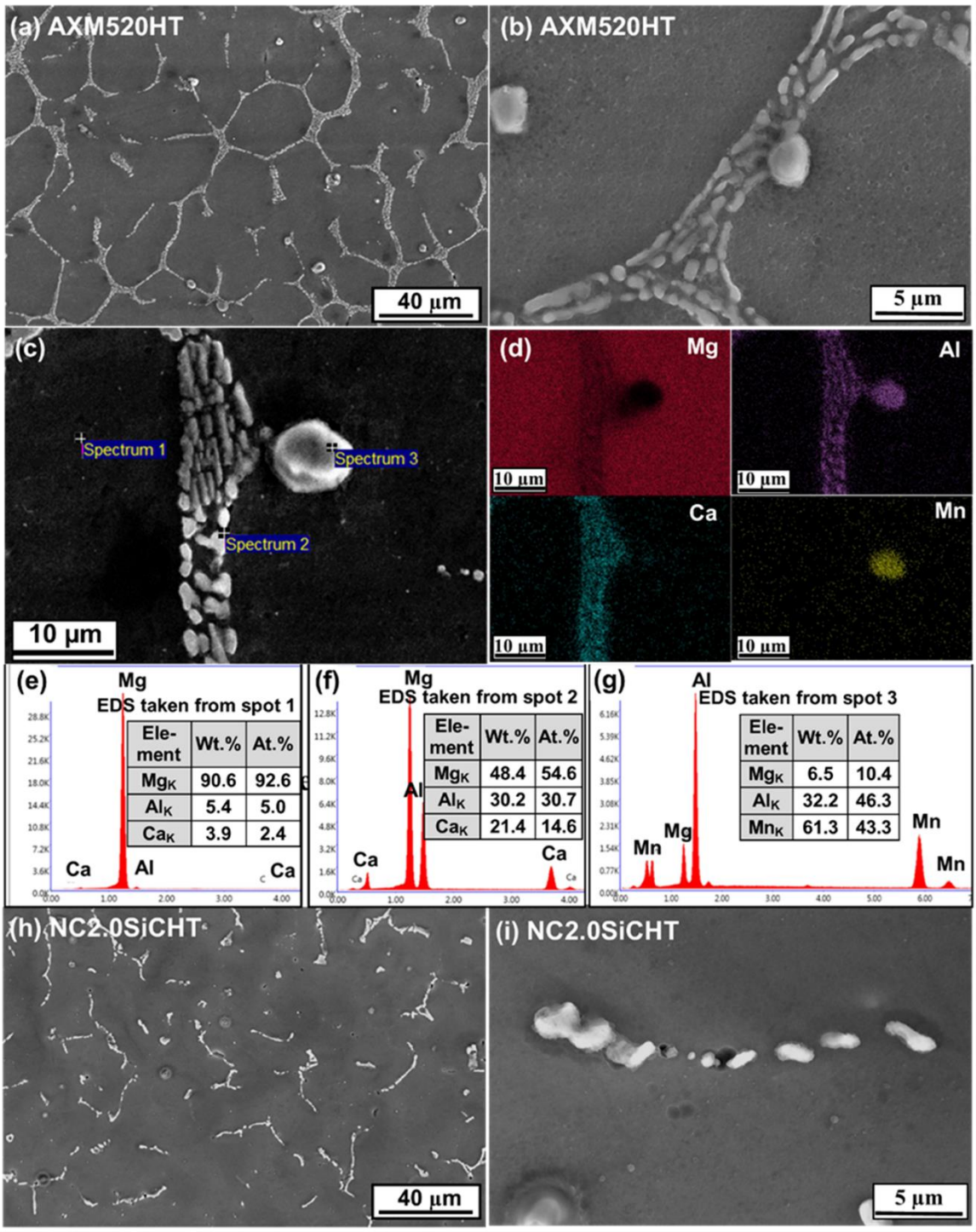

Figure 8.2 (a) SEM micrograph of the aged AXM520HT; enlarged view of 'a' showing the (b) morphologies of C36 and Al_8Mn_5 phases, and (c) regions of elemental mapping and EDS analyses; (d) elemental maps corresponding to 'c'; EDS results from (e) spectrum 1 corresponding to α-Mg, (f) spectrum 2 corresponding to C36, and (g) spectrum 3 corresponding to Al_8Mn_5; (h) SEM micrograph of the aged NC2.0SiCHT; (i) enlarged view of 'h' showing the morphology of C36 phase.

increased and modified the secondary phase's morphology during the casting of the nanocomposites. The TEM micrograph acquired from the α-Mg phase of aged AXM520HT alloy is shown in Figure 8.3(a). Two different precipitates with rod and planner-like morphologies were present in the α-Mg grain interior of the alloy, and the same is seen in the magnified micrograph provided in Figure 8.3(b). Figure 8.3(c) presents the SAED pattern obtained from the same region, displaying a dot pattern characteristic of the α-Mg phase acquired from the [0001] beam direction. Additionally, multiple ring patterns were also observed, and these are from the precipitates formed in the α-Mg grain interior. The 'd' spacing calculated from the smaller ring value was equal to 2.13 Å, confirming the {306} plane of the Al_8Mn_5 phase. The 'd' spacing of the bigger ring is 1.52 Å, confirming the {511} plane of the Al_2Ca (C15) phase. The rod-like precipitates have a length of 85.4±1.6 nm and a width of 10.7±1.3 nm, whereas the planner-type precipitate has a length of 65.3±2.1 nm. The probable precipitates that might form in the AXM alloys are Mg-Al, Mg-Ca, Mg-Mn, Al-Ca, Al-Mn, and Ca-Mn, and their enthalpies of mixing are -2, -6, 35, -20, -70, and 59, respectively. Therefore, the Al-Mn and Al-Ca precipitates formed due to their lower values of enthalpy of mixing [145]. Zuo et al. [62] reported that the rod-like precipitates were enriched with Al and Mn and identified as the Al_8Mn_5 phase. The planar precipitates were identified as the Al_2Ca phase. Nakata et al. [146] reported the formation of planner Al_2Ca precipitates after age-hardening of the AXM10304 alloy. Bian et al. [147] too mentioned the formation of planner Al_2Ca precipitates during age-hardening of AXM alloys and concluded that these semi-coherent precipitates were monolayered G.P. zones. Figure 8.3(d) exhibits the grain interior of NC2.0SiCHT. In the nanocomposites, the rod and planner-like precipitates were also observed. A phase with spherical morphology was also observed, as displayed in Figure 8.3(e). As mentioned earlier, the SAED pattern in Figure 8.3(f) acquired from the region of Figure 8.3(e) exhibits multiple ring patterns that correspond to the Al_8Mn_5 and Al_2Ca phases. Additionally, a ring pattern from the {111} plane of the SiC phase with the d spacing of 2.52 Å was also observed.

8.3 Creep behavior

8.3.1 Creep response and creep mechanism

Figure 8.4(a) compares the time dependency of the impression depth of the age-hardened alloy and nanocomposites at a stress of 435 MPa and temperature of 498 K. All the curves consist

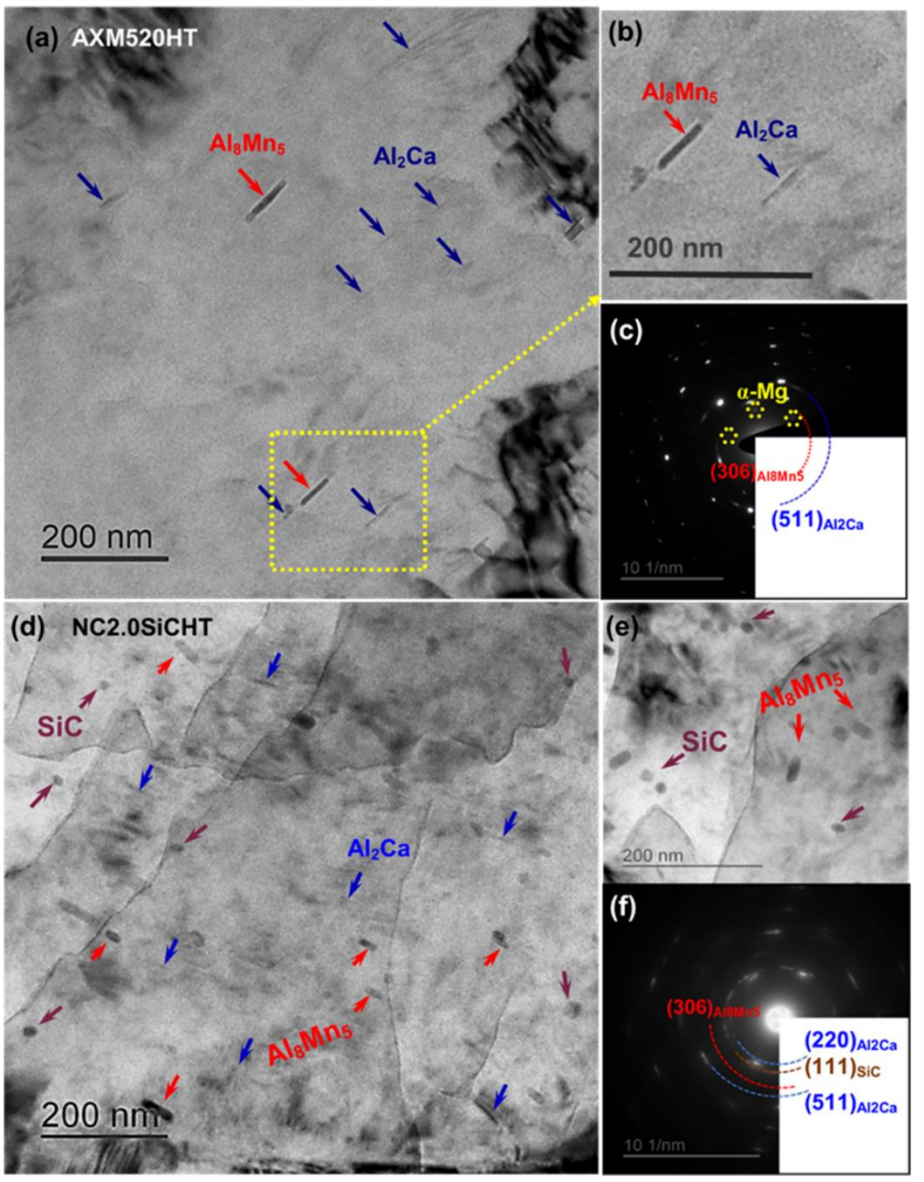

Figure 8.3 (a) TEM image (BF) revealing the precipitates formed in the α-Mg grain interior of AXM520HT; (b) enlarged view of 'a' showing two precipitates with rod and planner-like morphologies, (c) SAED pattern captured from 'a'; (d) TEM image (BF) exhibiting the presence of precipitates and SiC_{np} in the α-Mg grain interior of NC2.0SiCHT; (e) enlarged view of 'd' showing the morphologies of precipitates and dispersed SiC_{np} phase, (f) SAED pattern captured from 'c'

of only two stages of creep deformation (i.e., primary and secondary stages) after instantaneous deformation. The creep curve is divided into three distinct regions in conventional creep testing. However, impression creep curves do not exhibit the tertiary stage due to the test's compressive nature. The indentation depth over a fixed period was lower in the NCs than the alloy, implying that the SiC-dispersed nanocomposites were more creep-resistant than the AXM520HT alloy. The time dependency of the impression velocity of all the samples corresponding to Figure 8.4(a) is depicted in Figure 8.4(b). The impression velocity profile displayed a biphasic trend, wherein the primary stage was marked by a velocity reduction, followed by a stabilization stage in the secondary stage. The balance between strain hardening and recovery rate was the reason for constant steady-state impression velocity in the secondary stage. Figure 8.4(b) also depicts the steady-state impression velocity values with bar diagrams. The nanocomposites exhibited lower steady-state impression velocities than the AXM520HT alloy. The steady-state impression velocities of NC1.0SiCHT and NC2.0SiCHT decreased by 54% and 76%, respectively, compared to the AXM520HT. The measured creep rate in heat treated samples were improved closed to 30 % in all the compositions.

The creep mechanism that controlled the deformation of the alloy and NCs is evaluated by determining the stress exponent (n) and activation energy (Q) values. The well-established Mukherjee-Bird-Dorn equation related to the steady state creep rate ($\dot{\varepsilon}$) for conventional creep tests is given in Eq. 6.1 and reproduced as follows [65].

$$\dot{\varepsilon} = A\frac{Gb}{KT}\left(\frac{b}{d}\right)^{p}\left(\frac{\sigma}{G}\right)^{n} D_o e^{-\frac{Q}{RT}}$$

In this equation, A, G, b, d, D_0, and T are defined as a material constant, shear modulus, burgers vector, grain size, diffusion coefficient, and test temperature, respectively. In an impression creep test $\dot{\varepsilon} = \frac{V_{imp}}{Indentor\ diameter}$ (s^{-1}), and $\sigma = \frac{\sigma_{imp}}{3}(MPa)$, as mentioned in Eq. 6.2.

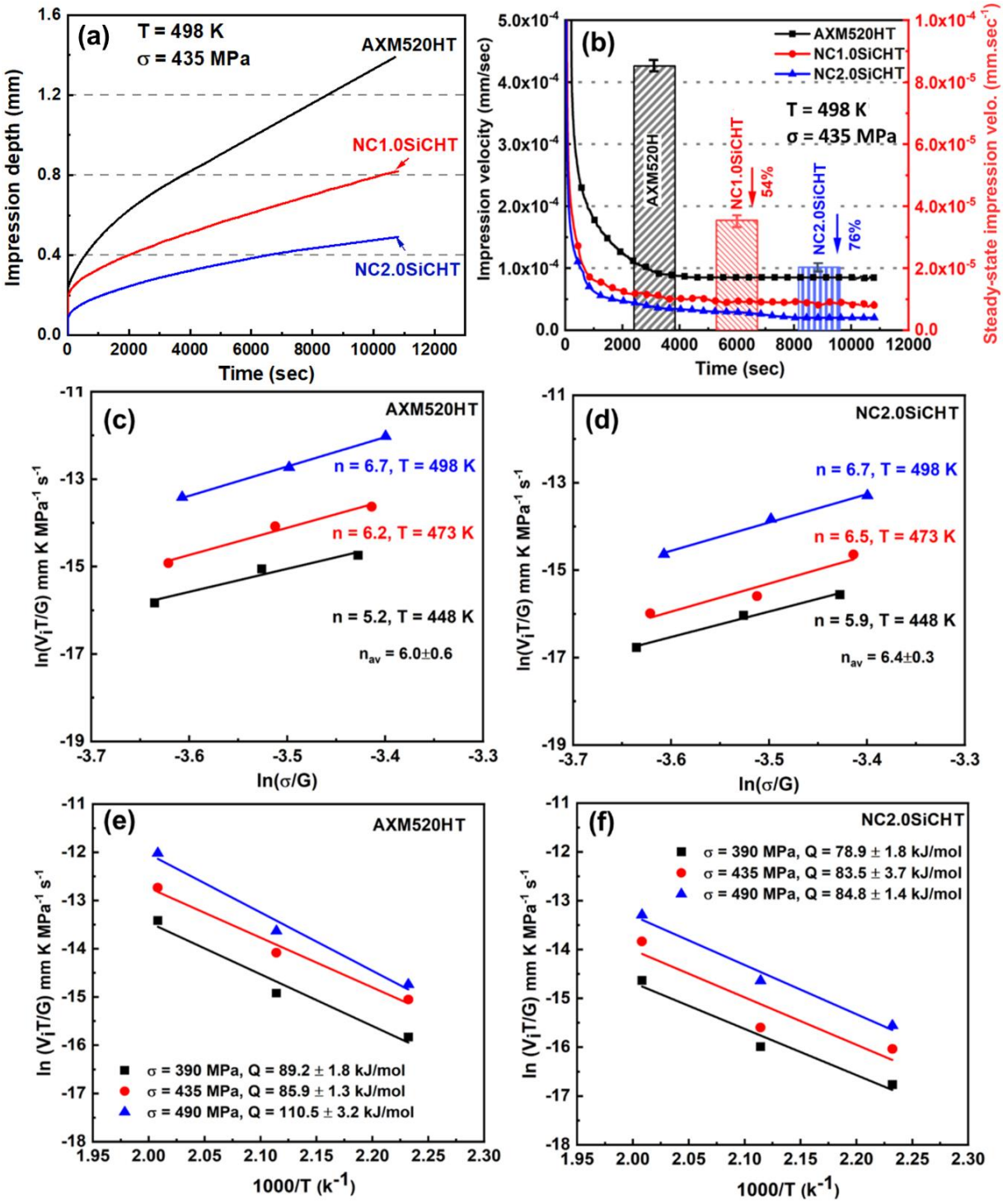

Figure 8.4 (a) Impression depth vs. time plots obtained at 435 MPa and 498 K for the aged AXM520HT and NCs; (b) steady-state impression velocity vs. time plot for AXM520HT and NCs corresponding to 'a'; representative plots showing (c and d) stress and (e and f) temperature dependence of steady-state impression velocities for AXM520HT and NC2.0SiCHT.

Thus, Eq. 6.1 for impression creep is modified as follows, as discussed earlier in Eq. 6.3 [30].

$$\frac{V_{imp}T}{G} = B\left(\frac{\sigma_{imp}}{G}\right)^n e^{\left(-\frac{Q}{RT}\right)}$$

For the heat-treated alloy and NCs, the values of n can be calculated from the slopes of $\ln\left(\frac{V_{imp}T}{G}\right)$ vs. $\ln\left(\frac{\sigma_{imp}}{G}\right)$ plots at a fixed temperature, and the values of Q can be evaluated by multiplying universal gas constant (R = 8.314 $JK^{-1}.mol^{-1}$) with the slope of $\ln\left(\frac{V_{imp}T}{G}\right)$ vs. 1000/T curves at a constant stress. Figure 8.4(c and d) displays the calculations of n values of the AXM520HT and NC2.0SiCHT, respectively, at all tested temperatures. The average n values of the AXM520HT and NC2.0SiCHT were 6.0 ± 0.6 and 6.4 ± 0.3, respectively. The creep deformation mechanism of the alloy and NCs was identified as a dislocation climb based on the calculated stress exponent (n) value. The Q values for the AXM520HT alloy, and NC2.0SiCHT were evaluated as displayed in Figure 8.4(e and f). The Q values for the AXM520HT and NC2.0SiCHT were in the range of 78.9 ± 1.8 to 110.5 ± 3.2 kJ/mol for NC2.0SiCHT. The Q values obtained in the current study are very close to the value responsible for the pipe diffusion of Mg, i.e., 92 kJ/mol. A summary of the n and Q values at different temperatures and stresses for all the samples is given in Table 8.1 and 8.2.

Table 8.1 Summary of the n values obtained from the creep tests at different temperature levels.

Temp. (K)	n		
	AXM520HT	NC1.0SiCHT	NC2.0SiCHT
448	5.2	5.8	5.9
473	6.2	6.4	6.5
498	6.7	6.8	6.7
n_{av}	6.0±0.6	6.3±0.4	6.4±0.3

Table 8.2 Summary of the Q values obtained from the creep tests at different stress levels.

Stress (MPa)	Q (kJ.mol^{-1})		
	AXM520HT	NC1.0SiCHT	NC2.0SiCHT
390	89.2±1.8	86.5±2.9	78.9±1.8
435	85.9±1.3	76.4±0.5	83.5±3.7
480	110.5±3.2	90.2±1.4	84.8±1.4
Q_{av}	95.2±10.9	84.4±5.8	82.4±2.5

8.3.2 Construction of creep mechanism map

The construction of a creep mechanism map is one of the essential aspects of creep study, which can be used in the future as a reference for the selection of stress and temperature range from the application point of view. In the present study, the Mg-Al-Ca (Ca/Al ~0.4) alloy's creep mechanism map was constructed. The construction of the map was achieved by following the equations given in Table 8.3. The material constant value (K_8) during dislocation climb assisted by lattice diffusion can be calculated from the intercept by fitting a straight line through the experimental data plotted in $ln\left(\frac{\dot{\varepsilon}b^2}{D_L}\right)$ vs. $ln\left(\frac{\sigma}{G}\right)$. Similarly, the K_9 value for dislocation climb assisted by pipe diffusion can be estimated from $ln\left(\frac{\dot{\varepsilon}b^2}{D_p}\right)$ vs. $ln\left(\frac{\sigma}{G}\right)$ plot. Figure 8.5(a) displayed the plot for both conditions. The lattice diffusion-controlled data of AX52 [148] alloy showed that the fitted straight line had a slope of 5, equal to the n value during lattice diffusion. The estimated K_8 value was 6.34×10^8. Additionally, the pipe-diffusion-controlled creep of AXM520 and AXM620 was plotted, and the n value was found to be ~7, indicating dislocation climb assisted by pipe diffusion [149]. The K_9 value for the AX alloys was found to be 1.25×10^8. Figure 8.5(b) shows the plot for grain boundary sliding (GBS) condition to estimate the value of K_4 and K_5. The K_4 and K_5 values were estimated using the linear fit method from the $ln\left(\frac{\dot{\varepsilon}d^3}{D_{gb}.b}\right)$ vs. $ln\left(\frac{\sigma}{G}\right)$ and $ln\left(\frac{\dot{\varepsilon}d^2}{D_p}\right)$ vs. $ln\left(\frac{\sigma}{G}\right)$ plots, respectively [18,150,151]. The slope of the linear fit was ~2 for GBS assisted by grain boundary diffusion and ~4 for pipe diffusion assisted GBS. The K_4 and K_5 were estimated as 1.25×10^5 and 1.58×10^5, respectively. Thereafter, the rest of the constant values were taken from the work by Somekawa et al. to construct the entire deformation mechanism map [117]. Figure 8.5(c) exhibits the creep deformation mechanism map in terms of $ln(d)$ vs. $ln\left(\frac{\sigma}{G}\right)$ for the AX alloys at 473 K. The

experimental values from previous literature and current investigations were plotted on the map [18,149-151]. Further, Figure 8.5(d) exhibits a creep deformation mechanism map as a function of $ln\left(\frac{\sigma}{G}\right)$ and (T/T_m) (homologous temperature). The map was constructed by considering grain size (d) as 33 μm, equal to the grain size of NC2.0SiCHT. The creep deformation maps constructed in the present investigation map correctly predict the creep deformation mechanism involved for the Mg-Al-Cal-based alloys and their NCs over a combination of stress, temperature, and grain size range. The maps exhibit that diffusion-based creep can occur only at high temperatures when the grain size is < 100 μm (10^{-4} m) and applied stress is low ($\sigma/G < 10^{-5}$). Therefore, for the targeted application regime (i.e., 473 to 498 K) for the AX-based alloys, the chances of diffusion-based creep are nil. In the present investigation, the creep tests were performed with the applied normalized stress (σ/G) > 10^{-5}, and homologous temperature ranges from 0.4 to 0.6. Based on this, the maps predict that the creep deformation is dominated by dislocation climb in the AXM520 alloy and its NCs, which is already concluded based on the values of n and Q. The grain boundary sliding added by diffusion will dominate when the grain size is below 10 μm [18,150]. However, the boundary between the pipe and lattice-based diffusion is not distinct, which is attributed to the lack of data availability in this regime. Therefore, these newly constructed maps could be used as a reference to predict the creep deformation mechanism for a particular stress, temperature, and grain size range for the AX alloys.

8.4 Microstructural analyses of creep-tested specimens

8.4.1 Observation of deformed region

The indentations produced on the creep-tested (435 MPa and 498 K) specimens of the AXM520HT and NC2.0SiCHT were bisected along the diameter, and the microstructural observations were carried out by taking the regions from the edges of the indenter. The SEM micrographs from the regions are provided in Figure 8.6(a and b). As expected, the three distinct regions are observed under the indenter, which is the characteristic of an indentation. The Hertzian stress distribution below the indentation is understood using Eq. 6.4, as discussed earlier [119].

$$\sigma_z = -\frac{1}{2}\frac{P_m}{(1-\frac{r^2}{a^2})^{1/2}}$$

The indentation test applies a mean pressure of P_m, generating a normal stress of σ_z beneath the indenter.σ_zThe radius of the flat indenter is ‘a’, and radial distance r is considered from the

Table 8.3 List of equations with constant values employed to construct the creep deformation mechanism maps of the Mg-Al-Ca-based alloys and their nanocomposites.

Creep mechanisms		Equations	Value of material constant (K) (s^{-1})
Diffusional flow	Nabarrow-Herring	$\dot{\varepsilon} = K_1\left(\frac{D_L}{d^2}\right)\left(\frac{Eb^3}{KT}\right)\left(\frac{\sigma}{G}\right)$	14 [117]
	Coble	$\dot{\varepsilon} = K_2\left(\frac{D_{gb}.b}{d^3}\right)\left(\frac{Eb^3}{KT}\right)\left(\frac{\sigma}{G}\right)$	50 [117]
Grain boundary (GB) sliding	Lattice diffusion	$\dot{\varepsilon} = K_3\left(\frac{D_L}{d^2}\right)\left(\frac{\sigma}{G}\right)^2$	1.8×10^{6} [117]
	GB diffusion	$\dot{\varepsilon} = K_4\left(\frac{D_{gb}.b}{d^3}\right)\left(\frac{\sigma}{G}\right)^2$	1.25×10^{5} *
	Pipe diffusion	$\dot{\varepsilon} = K_5\left(\frac{D_p}{d^2}\right)\left(\frac{\sigma}{G}\right)^4$	1.58×10^{5} *
Dislocation climb	Harper-Dorn	$\dot{\varepsilon} = K_6\left(\frac{D_L}{b^2}\right)\left(\frac{Eb^3}{KT}\right)\left(\frac{\sigma}{G}\right)$	7.0×10^{-11} [117]
	Solute drag	$\dot{\varepsilon} = K_7\left(\frac{D_s}{b^2}\right)\left(\frac{\sigma}{G}\right)^3$	3.0×10^{-2} [117]
	Lattice diffusion	$\dot{\varepsilon} = K_8\left(\frac{D_L}{b^2}\right)\left(\frac{\sigma}{G}\right)^5$	6.34×10^{8} *
	Pipe diffusion	$\dot{\varepsilon} = K_9\left(\frac{D_p}{b^2}\right)\left(\frac{\sigma}{G}\right)^7$	1.25×10^{8} *
Equations for diffusional coefficient and G value			
D_p	Pipe diffusion	$3.6\times10^{-5}e^{-92000/kT}$	
D_{gb}	GB Diffusion	$7.7\times10^{-3}e^{-92000/kT}$	
D_L	Lattice diffusion	$1.0\times10^{-4}e^{-135000/kT}$	
D_s	Solute-drag Diffusion	$1.2\times10^{-3}e^{-143000/kT}$	
G (MPa)	Shear modulus	18460 - 8.2×T (MPa)	
b	Burgers vector	3.21×10^{-10} (m)	

*Calculated in the present investigation for the Mg-Al-Ca-based alloys and their nanocomposites from Figure 8.5(a and b)

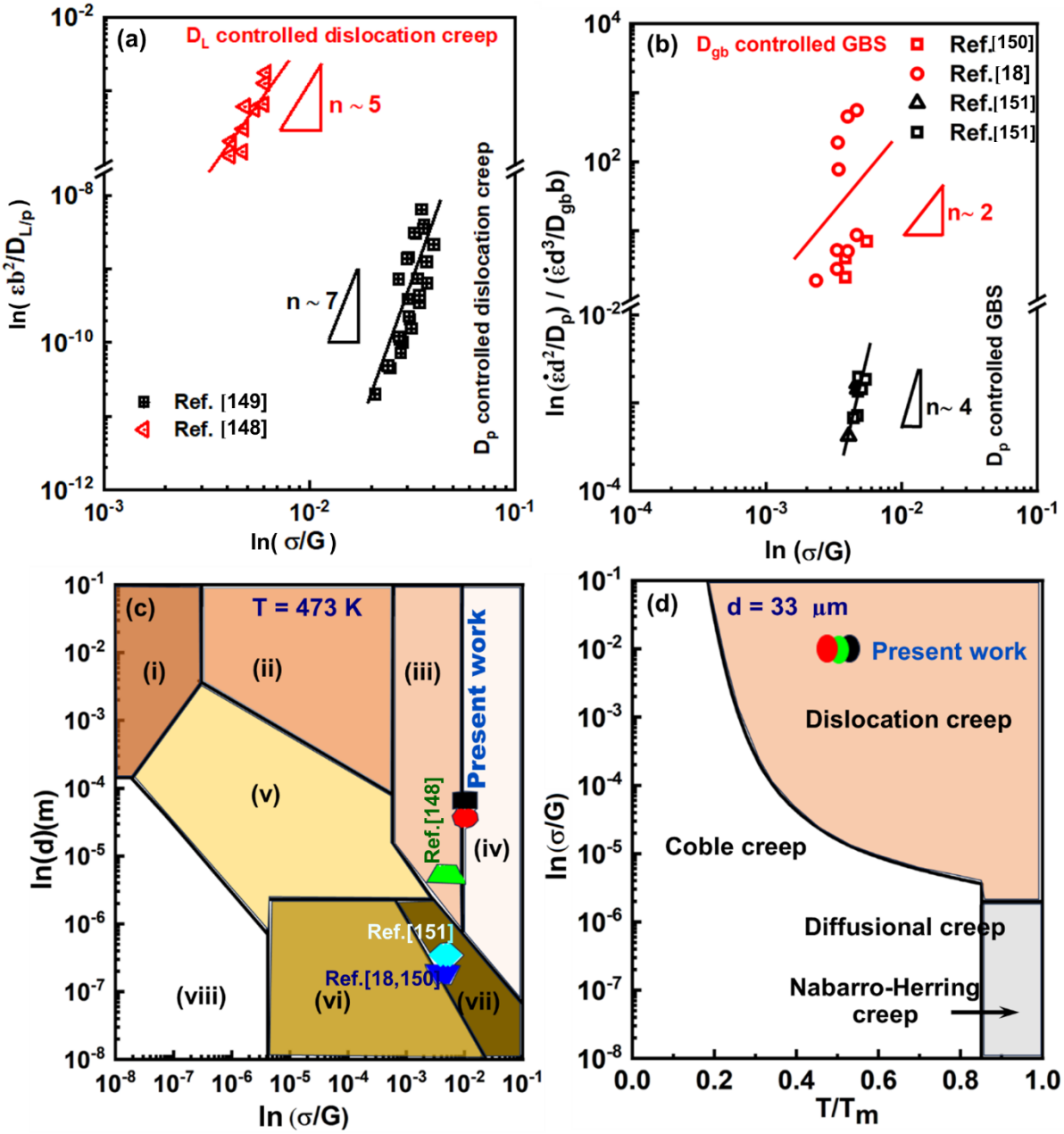

(i) Harper–Dorn creep (n = 1), (ii) Solute drag creep (n = 3), (iii) Climb-controlled creep (n=5) lattice diffusion , (iv) Climb-controlled creep (n = 7) pipe diffusion, (v) GBS lattice diffusion (n = 2), (vi) GBS grain boundary diffusion (n = 2), (vii) GBS pipe diffusion (n = 4), (viii) Diffusional flow (n = 2) coble creep. [117]

Figure 8.5 Diffusion coefficient normalized steady-state strain rate vs. shear modulus normalized applied stress plot exhibiting various deformation mechanisms in Mg-Al-Ca (AX) alloys (a) D_L- and D_p -controlled dislocation creep; (b) D_{gb}- and D_p -controlled grain boundary sliding creep; (c) grain size vs. shear-modulus normalized applied stress plot exhibiting dislocation mechanism map of Mg-Al-Ca (AX) alloys and their nanocomposites at 473 K, and (d) shear modulus normalized applied stress vs. homologous temperature plot for NC2.0SiCHT with grain size of 33 μm.

center of the flat indenter. Below the indenter, at the center point (i.e. r = 0,) σ_z = - 0.5 P_m. Thus, the R1 region, just underneath the indenter, undergoes a minimal deformation and forms a hemispherical hydrostatic stress zone (i.e., dead zone). As the value of 'r' reaches a (i.e., at the indenters' edge), the σ_z value increases drastically and reaches infinity at the indenters' edge. Therefore, the region marked as R2 experiences localized shear force and undergoes shear deformation. The spread of region R2 exhibits the deformation resistance offered by the material during the creep test at a particular stress and temperature. The region R2 is wider in AXM520HT than NC2.0SiC, implying the inferior creep response of the former. The region away from the indention, i.e., region R3, shows an undeformed zone similar to that of the untested region. This region experienced negligible stress, and accordingly, the microstructural alteration was negligible. The magnified view of R2 of AXM520HT shows that the secondary phase was utterly broken, whereas the same remains intact within the α-Mg matrix in the case of NC2.0SiCHT. This implies that the presence of SiC_{np} in NC2.0SiCHT gave additional strengthening in the NC2.0SiCHT matrix compared to the AXM520HT.

The EBSD data were acquired from the highly deformed regions, i.e., the regions at the edges of the indenter, as shown in Figure 8.6(a and b) of the creep tested (498 K and 435 MPa) AXM520HT and NC2.0SiCHT. The grain boundary map corresponding to the region is shown in Figure 8.7(a and b). The grain boundary misorientation value lower than 15 º is defined as the low-angle grain boundaries (LAGBs), and the misorientation above 15 º is considered as the high-angle grain boundaries (HAGBs). The results show that in both the alloy and NCs, the highly deformed regions are populated with HAGBs. In addition, the twin boundaries inside grain interiors of all the samples were observed. The formation of twins during deformation of Mg alloy and composites is well known owing to their limited slip systems [152]. Figure 8.7(c and d) exhibits the misorientation map corresponding to Figure 8.7(a and b). The results show the frequency of HAGBs was high in all the cases. In addition, the contribution of different twins in HAGBs is also shown. The formation of double twin (38º, $\{10\bar{1}1\}$-$\{10\bar{1}2\}$), compression twin (56º, $\{10\bar{1}1\}$), and extension twin (86º, $\{10\bar{1}2\}$) is observed in the alloy and NCs [152-154]. The formation of $\{10\bar{1}1\}$ and $\{10\bar{1}2\}$ twins took place by rotating the twinned lattice around the $<1\bar{2}10>$ direction by 56º and 86º, respectively. Similarly, the double twin was formed by rotating the c-axis around $<1\bar{2}10>$ direction for both the primary and secondary twins. Their existence in creep-tested AXM520HT and NC2.0SiCHT can be further confirmed by the inverse pole figure maps shown in Figure 8.7(e). In all the cases, the inverse pole figure

maps confirm the presence of <1$\bar{2}$10> oriented boundaries. The inverse pole figure maps in the range of 84-88º indicate that many HGBs are oriented along <1$\bar{2}$10>. This result indicates that the deformed samples are populated with extension twins. The comparison of the twin-frequency percentage of the AXM520HT and NC2.0SiCHT is displayed in Figure 8.7(f). In all the twin modes, it has been observed that the percentage of twins in the creep-tested specimen of NC2.0SiCHT was lower than that of the AXM520HT alloy. This indicates the presence of nanoparticles successfully hindered the growth of the twins in NCs, contributing to the lower deformation of the NCs compared to the AXM520HT. Therefore, in the creep tests, the SiC_{np} dispersed AXM520HT composites showed a better creep response than the AXM520HT. Shi et al. [155] concluded that nano-sized precipitates hindered the twin growth in Mg alloys. Antony et al. [156] also confirmed that the particles present in the grain boundaries of Mg alloys also hindered twin growth. Leu et al. [157] concluded that the precipitates provided back stress, which significantly restricted the development of twins in the AZ91 alloy.

8.4.2 Characterization of twinning and dislocations

The twined formed during creep deformation (T = 498 K and σ = 435 MPa) of the NC2.0SiCHT specimen is shown in Figure 8.8(a to d). Figure 8.8(a) exhibits a lamellar-type twin in the deformed sample of NC2.0SiCHT. The twin was bound by two twin boundaries (TB) separated from the matrix of the NC. Numerous dislocations, nano-precipitates of Al_8Mn_5 and Al_2Ca phases, and dispersed SiC_{np} phase were observed near the TB. The presence of nano-precipitates and SiC_{np} at TB suggests that they hindered the twin growth in the α-Mg matrix. Several other researchers also reported that the precipitates and dispersed phases hindered twin growth in Mg alloys [158,159]. This also supports the claim that the lower creep deformation of NC2.0SiCHT was owing to twin growth restriction provided by the dispersed SiC_{np} phase.

Figure 8.8(b) exhibits the SAED pattern captured from TB region displayed in Figure 8.8(a). SAED pattern analysis reveals that the twinned lattice rotated around 86 º along <1$\bar{2}$10> to produce {10$\bar{1}$2} twin. The twin system was classified as an extension twin of {10$\bar{1}$2}<10$\bar{1}$1>. Therefore, the twinning plane was identified as {10$\bar{1}$2} and the <10$\bar{1}$1> was the direction of the twin. The brightfield (BF) image in Figure 8.8(c) exhibits another twin variant produced during the creep deformation. The corresponding SAED pattern is provided in Figure 8.8(d). SAED pattern analysis reveals that the matrix and twin lattice were oriented by 37.4 º. Further, indexing confirms that the twin was {10$\bar{1}$1}-{10$\bar{1}$2} double twin. The double twin formed due

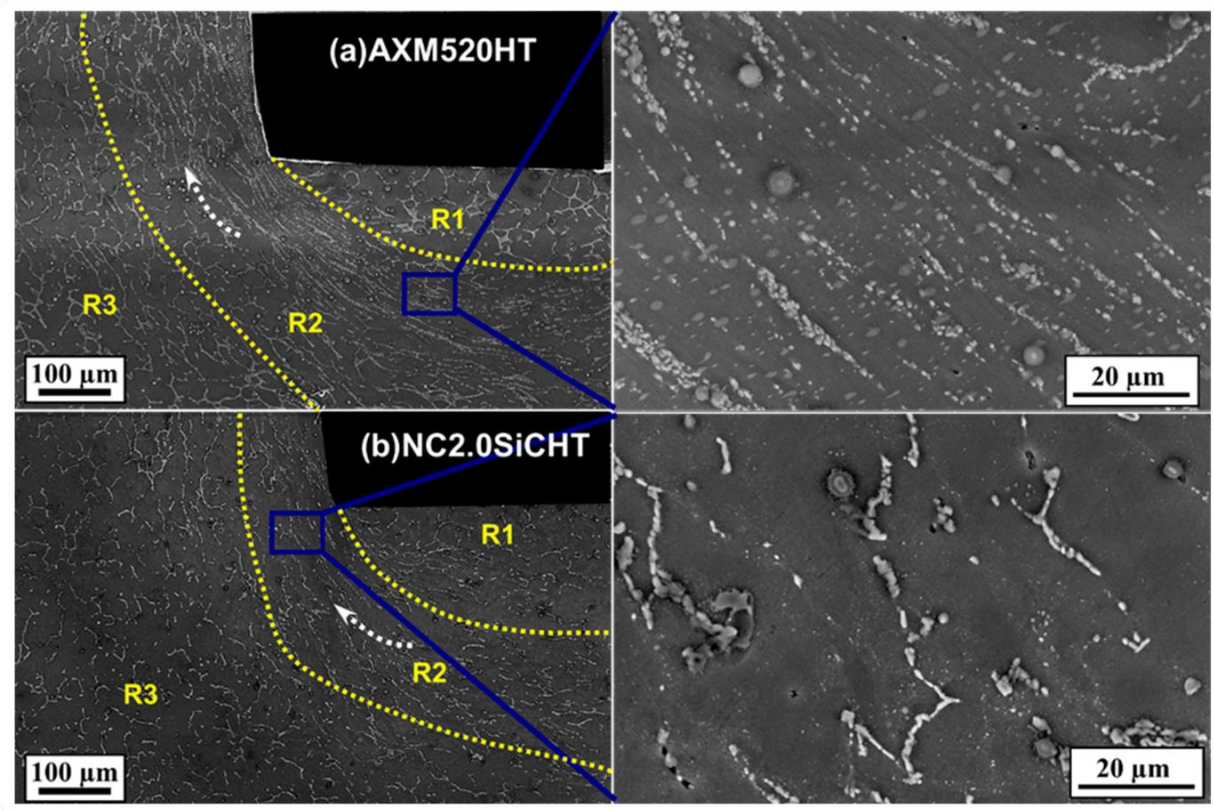

Figure 8.6 SEM micrographs exhibiting the deformation flow pattern in different regions under impressions on the creep-tested (T = 498 K, σ = 435 MPa) specimens of (a) AXM520HT, as well as (b) NC2.0SiCHT.

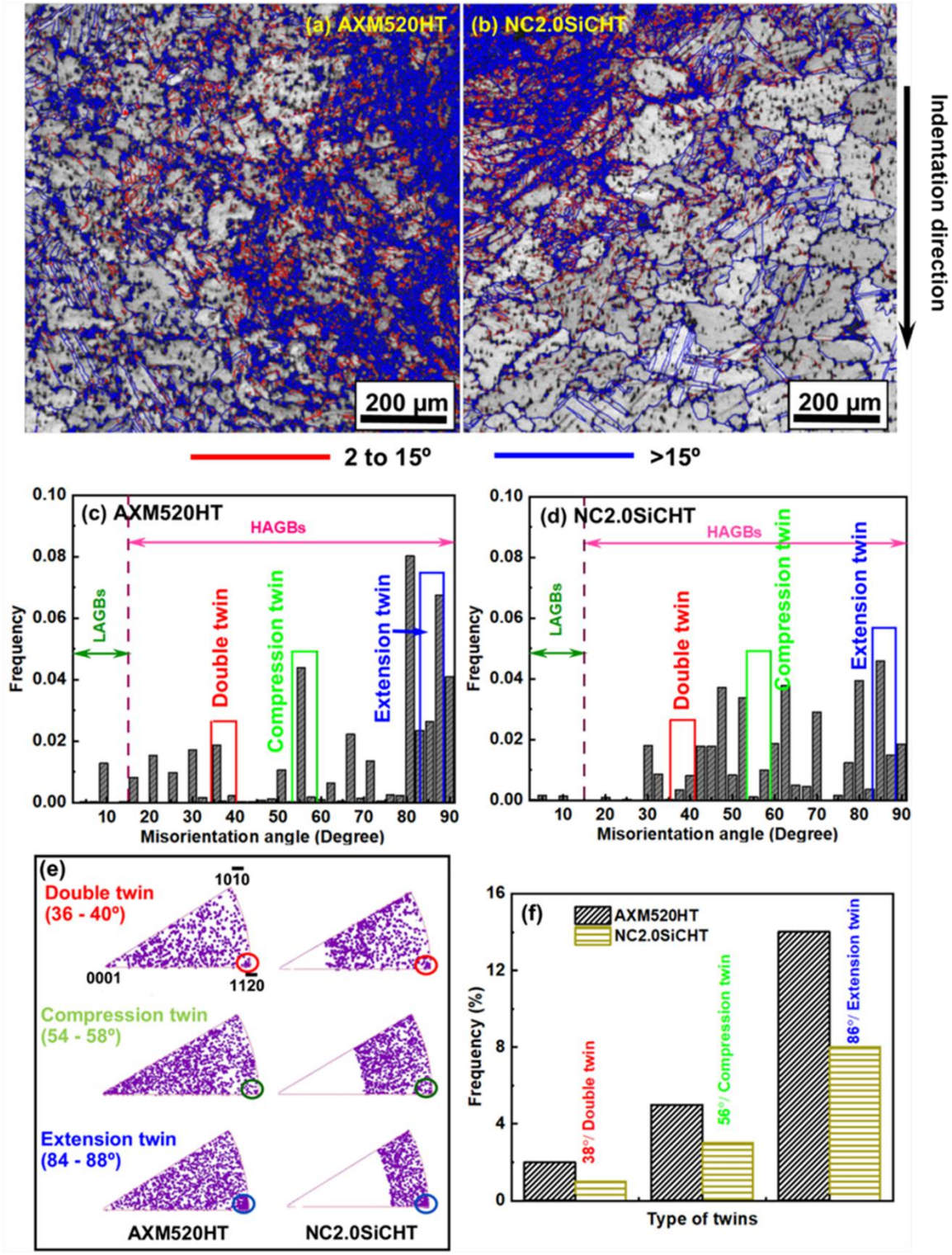

Figure 8.7 EBSD GB maps captured from the highly deformed corner regions of (a) AXM520HT and (b) NC2.0SiCHT; (c) and (d) misorientation map corresponding to 'a' and 'b', respectively; (e) IPF maps for the twins observed in AXM520HT and NC2.0SiCHT; and (f) comparison of twin fractions in creep-tested (T = 498 K, σ = 435 MPa) AXM520HT and NC2.0SiCHT.

to c-axis rotation along <1$\bar{2}$10> direction in both cases. Further, the SAED pattern indicates a massive sub-grain formation or dislocation accumulation around the TB during formation of this double twin. The occurrence of the dislocation pile-ups around the TB is depicted by the strain contrast in Figure 8.8(c).

The analyses of the dislocations present in the creep-tested specimen of the NC2.0SiCHT were carried out using two-beam condition **g.b**=0. The **'g'** corresponds to the diffraction vector, and b is known to be the burgers vector. In this condition, while a crystal is diffracted along **g**=0002, the dislocations with **b**=<0001> are visible in both BF and DF images by satisfying the criteria **g.b≠0**. These dislocations are known as <c> type dislocations. In the same region, the <a> type dislocations with **b**=<11$\bar{2}$0> were not visible with **g**=0002 when **g.b**=0 is satisfied. However, if the same area is seen along the **g**=10$\bar{1}$0 direction, the <a> type dislocations will be visible in both BF and DF images. On the other hand, the dislocations with **b**=<11$\bar{2}$3> will appear with both the **g** vectors (i.e., **g**= 0002 and **g**= 10$\bar{1}$0) as **g.b**≠0. These types of dislocations are known as <c+a> dislocations. The BF and DF images taken from the NC2.0SiCHT in Figure 8.9(a and c) displayed the <a> and <c+a> dislocation when exited along **g**=10$\bar{1}$0. The same region was also observed by exciting **g**=0002, as shown in Figure 8.9(b and d). The <c> and <c+a> dislocations were observed in both the BF and DF images. Interestingly, the <c+a> dislocations were observed in all the images at the same position under all the conditions, confirming their existence. A careful observation of Figure 8.9(a and b) reveals that the density of the <c> type dislocations was much higher than that of the <a> type dislocations. It is reported that the <a> type dislocations are associated with the low critical resolved shear stress (CRSS), which allowed them to glide easily during deformation [160]. In the process, the dislocation annihilation took place that resulted in the reduced dislocation density of <a> type. On the contrary, the higher value of CRSS of the <c> type dislocation made them sessile. A schematic of the <c+a> dislocation's dissociation into glissile <a> and sessile <c> dislocations is portrayed in Figure 8.9(e). After dissociation of the <c+a> dislocations at the intersection of the non-basal and basal planes, the <a> component easily glide in the closed packed basal plane, whereas the <c> type dislocation remained in the pyramidal or prismatic plane (i.e., non-basal plane), contributing to the strain hardening. The BF and DF images in Figure 8.9(f and g) exhibited that the dislocation bowed due to the presence of SiC_{np}. The dislocations in NCs had to overcome the additional stress field associated with the SiC_{np} phase. Thus, the creep resistance of the NCs was higher compared to the AXM520HT.

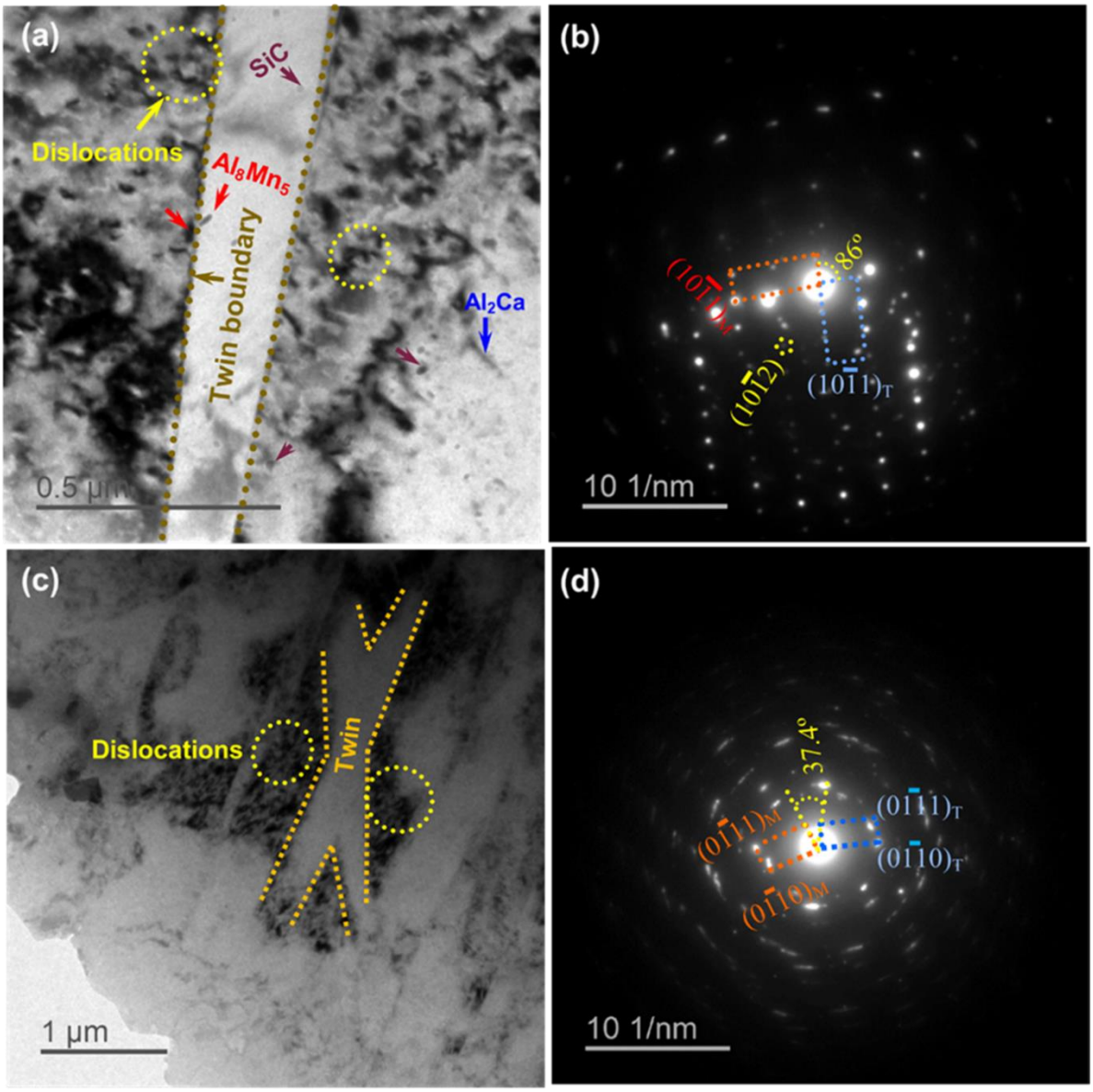

Figure 8.8 (a) BF image exhibiting an extension twin of type $\{10\bar{1}2\}<10\bar{1}1>$ taken from creep-tested NC2.0SiCHT; (b) SAED pattern corresponds to 'a'; (c) BF image exhibiting a double twin of type $\{10\bar{1}1\}$-$\{10\bar{1}2\}$ taken from creep-tested AXM520HT; (d) SAED pattern corresponds to 'c'.

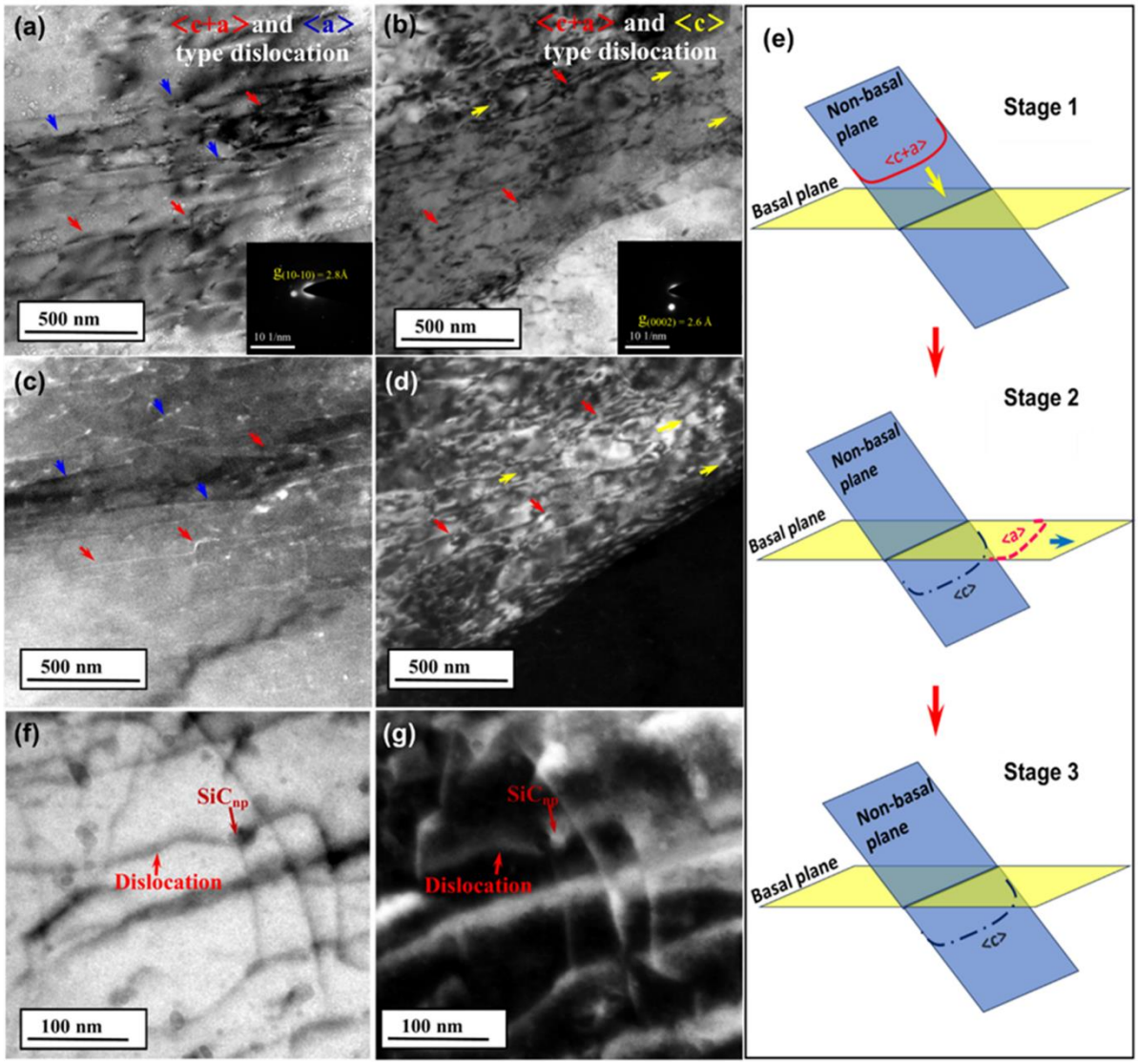

Figure 8.9 (a) and (c) BF and DF images of the <c+a> and <a> type dislocations while **g** = $10\bar{1}0$; (b) and (d) BF and DF images of the <c+a> and <a> type dislocations while **g** = 0002 in the same location taken from creep-tested NC2.0SiCHT; (e) schematic exhibiting <c+a> dislocation's dissociation into <a> and <c> type dislocations; (f) and (g) BF and DF image of the dislocation interaction with SiC_{np} in NC2.0SiCHT creep teste at 435 MPa and 473 K.

8.5 Summary of chapter 8

In the present chapter, the microstructural alteration and creep characteristic of the squeeze-cast age-hardened Mg-5.0Al-2.0Ca-0.3Mn (AXM520HT) alloy, as well as AXM520HT+1.0SiC (NC1.0SiCHT) and AXM520HT+2.0SiC (NC2.0SiCHT) (wt.%) nanocomposites (NCs) has been presented. The major findings from the current chapter are summarized below.

i. The age-hardened AXM520HT, NC1.0SiCHT, and NC2.0SiCHT contain the primary α-Mg grains, the discontinuous $(Mg, Al)_2Ca$ (C36) phase at the grain boundaries, and randomly present spherical-shaped Al_8Mn_5 phase. All the NCs additionally contain SiC phase.

ii. The NCs revealed superior creep resistance compared to AXM520HT, and it was the best in the NC2.0SiCHT. The improvement was 76% in NC2.0SiCHT compared to AXM520HT.

iii. The creep deformation was dominated by Dislocation climb facilitated by pipe diffusion at the chosen test temperature and stress ranges. The newly constructed maps could be used as a reference to predict the creep deformation mechanism for a particular stress, temperature, and grain size range for the Mg-Al-Ca-based alloys and NCs.

iv. The C36 phase was utterly broken in the AXM520HT, whereas the same remains intact in the NC2.0SiCHT. The percentage of twins in the creep-tested specimen of NC2.0SiCHT was lower than in the AXM520HT alloy. The density of the <c> type dislocations was much higher than that of the <a> type dislocations in the NCs.

v. The significant improvement in creep resistance of all the NCs over the AXM520HT alloy was attributed to the age-hardening as well as dispersion strengthening from the nanoparticles.

Chapter 9

Conclusions and Scope for Future Research

9.1 Conclusions

In the present thesis, microstructural characterization, tensile and compression, creep and corrosion behavior of the squeeze-cast Mg-5.0Al-2.0Ca-0.3Mn (AXM520) alloy and nanocomposites with 0.5, 1.0, 2.0 and 3.0 (wt.%) of SiC_{np} is investigated. The nanocomposites (NCs) were abbreviated as NC0.5SiC, NC1.0SiC, NC2.0SiC and NC3.0SiC. Further, the microstructural evolution and creep characteristics of the squeeze-cast age-hardened Mg-5.0Al-2.0Ca-0.3Mn (AXM520HT) alloy, as well as AXM520HT+1.0SiC (NC1.0SiCHT) and AXM520HT+2.0SiC (NC2.0SiCHT) (wt.%) nanocomposites have been investigated. The major conclusions drawn from the present thesis are as follows.

Conclusions on microstructures, tensile, compression, creep, and corrosion behavior of the squeeze-cast AXM520 alloy and NCs

i. The microstructures of AXM520 alloy and NCs consist of a primary solid solution (α-Mg), a eutectic of α-Mg and $(Mg,Al)_2Ca$ (C36) phases, and an Al_8Mn_5 phase. Additionally, the SiC phase was also present in the NCs.

ii. The grain size of the NCs reduced as the concentration of the SiC_{np} increased in the AXM520 alloy, and the same decreased by 36.8% in the NC3.0SiC.

iii. The C36 phase formed a continuous network in the AXM520 alloy. However, the same in the NCs was fragmented and became discontinuous with the increase in the fraction of the SiC_{np}. Thus, the C36 phase was the most fragmented in the NC3.0SiC.

iv. The α-Mg and C36 phase present in the AXM520 alloy exhibited an orientation relationship of $(0001)_{\alpha\text{-Mg}} \,||\, (0001)_{C36}$, $[10\bar{1}0]_{\alpha\text{-Mg}} \,||\, [11\bar{2}0]_{C36}$. The lattice parameter values for the α-Mg and C36 phases were found to be a = 3.19 Å, c = 5.23 Å, and a = 5.92 Å, c = 9.87 Å, respectively

v. All the NCs exhibited superior tensile properties than the AXM520 alloy. The NC2.0SiC with 37.2 and 69.8% enhancement in YS and UTS exhibited the most superior tensile properties. The %El of the AXM520 alloy and NC2.0SiC were 1.03±0.03 and 3.1±0.02%, and it decreased to 1.29±0.02% in the NC3.0SiC. The UTS

and %El of the NCs declined with more than 2.0 (wt.%) SiC_{np} to the AXM520 alloy because of the nanoparticle agglomeration.

vi. The superior compressive properties were exhibited by the AXM520 alloy with the SiC_{np} additions. The presence of thicker shear bands in the fractograph of the NC3.0SiC indicated its higher energy absorption capability during failure than the AXM520 alloy.

vii. The strengthening from CTE mismatch contributed the most to the overall strengthening of all the NCs, and the same was 146.0% greater in the NC3.0SiC than the NC0.5SiC. The contribution from Orowan strengthening also increased by 121.2%. However, the Hall-Petch strengthening increased only by 18.1%with the increase in nanoparticle content from 0.5 to 3.0 (wt.%) in the NCs.

viii. The NCs revealed improved creep performance compared to the AXM520 alloy under the experimental parameters utilized. The creep resistance of the NCs increases with the increase in the SiC_{np} content. The NC2.0SiC exhibited an increase in creep resistance by 73.2% compared to the alloy. However, the creep resistance deteriorated with a further increase in the fraction of the SiC_{np} in the NC3.0SiC, due to the agglomeration.

ix. The stress exponents varied from 5.0 to 6.7, and activation energies varied from 89.8 to 101.8 kJ/mol, implying the deformation at elevated temperature in the AXM520 alloy and NCs was dominated by the climb of dislocation assisted by the pipe diffusion.

x. The pile-ups of dislocations took place around the C36 phase and near the SiC_{np}. The additional strengthening owing to the presence of the SiC_{np} in the NCs was responsible for their improved creep performance compared to the AXM520 alloy.

xi. The corrosion resistance of the NCs measured in the hydrogen evolution test was superior to the AXM520 alloy, and the improvement was 91.1% in the NC3.0SiC.

xii. The OCP of all NCs shifted to more noble values with the increased quantity of SiC_{np} in AXM520. The polarization resistance determined from the EIS increased with the increase in the SiC_{np} content in the NCs.

xiii. The potentiodynamic polarization scans further confirmed the superior corrosion resistance of the NCs to the AXM520 alloy. Among the fabricated NCs, NC3.0SiC exhibited the highest corrosion resistance, and it was 91.3% lower in comparison to the AXM520 alloy.

xiv. The corrosion products predominantly consist of $Mg(OH)_2$. The addition of SiC_{np} reduced the formation of $Mg(OH)_2$ and increased the content of the $Al(OH)_3$ in the NCs leading to the higher stability of the corroded film formed on them.

xv. The α-Mg phase was severely damaged owing to the galvanic corrosion between the α-Mg and C36 phases. However, the same was reduced due to a decrease in the volta potential between α-Mg and C36 phases in the NCs, resulting in their superior corrosion resistance.

Conclusions on microstructures and creep behavior of the squeeze-cast age-hardened AXM520 alloy and NCs

i. The age-hardened AXM520HT, NC1.0SiCHT, and NC2.0SiCHT contain the primary α-Mg grains, the discontinuous $(Mg, Al)_2Ca$ (C36) phase at the grain boundaries, and randomly present spherical-shaped Al_8Mn_5 phase. All the NCs additionally contain the SiC phase.
ii. The NCs revealed superior creep resistance compared to AXM520HT, and it was the best in the NC2.0SiCHT. The improvement was 76% in NC2.0SiCHT compared to AXM520HT.
iii. The creep deformation was dominated by dislocation climb facilitated by pipe diffusion at the chosen test temperature and stress ranges. The newly constructed maps could be used as a reference to predict the creep deformation mechanism for a particular stress, temperature, and grain size range for the Mg-Al-Ca-based alloys and NCs.
iv. The C36 phase was utterly broken in the AXM520HT, whereas the same remains intact in the NC2.0SiCHT. The percentage of twins in the creep-tested specimen of NC2.0SiCHT was lower than in the AXM520HT alloy. The density of the <c> type dislocations was much higher than that of the <a> type dislocations in the NCs.
v. The significant improvement in creep resistance of all the NCs over the AXM520HT alloy was attributed to the age-hardening as well as dispersion strengthening from the nanoparticles.

To conclude, the tensile, compression, creep, and corrosion behavior of the NC0.5SiC, NC1.0SiC, NC2.0SiC, and NC3.0SiC are superior to that of the AXM520 alloy. Thus, the use of NCs is beneficial over the AXM520 alloy. Among the fabricated NCs, NC2.0SiC is the best, considering the mechanical properties and corrosion behavior.

9.2 Scope for future research

The following research works on the squeeze-cast Mg-5.0Al-2.0Ca-0.3Mn (AXM520) alloy, and nanocomposites might be carried out in the future.

1. The tensile and compressive properties were evaluated at ambient temperature. It would be interesting to evaluate both of these properties at elevated temperatures.
2. The tensile, compressive, and corrosion properties were evaluated in as-cast condition. It would be interesting to evaluate these properties after aging.
3. The wear behavior of the AXM520 alloy and NCs in both as-cast and aged conditions may be evaluated.
4. The fatigue and creep-fatigue interaction of the AXM520 alloy and NCs in both as-cast and aged conditions may be evaluated.
5. The dislocation twin interaction revealed in the present study can be expanded further in future work, which may help to improve the understanding of the strengthening mechanisms in detail.
6. The creep mechanism map developed in the present study for AX alloys and composites needs to be addressed with more experimental data, which may help improve the map and make precise load and temperature range prediction possible.
7. Ultrasonic vibration may be employed for dispersing a higher volume fraction of SiC_{np}, and the tensile, creep, and corrosion behaviour may be evaluated with a higher content of SiC_{np}.

References

[1] M.O. Pekguleryuz, A.A. Kaya, Creep resistant magnesium alloys for powertrain applications, Adv. Eng. Mater. 5 (2003) 866-878.

[2] B.L. Mordike, Creep-resistant magnesium alloys, Mater. Sci. Eng. A 324 (2002) 103-112.

[3] S. Zhu, M.A. Easton, T.B. Abbott, J.F. Nie, M.S. Dargusch, N. Hort, M.A. Gibson, Evaluation of magnesium die-casting alloys for elevated temperature applications: Microstructure, tensile properties, and creep resistance, Metal. Mater. Trans. A 46 (2015) 3543-3554.

[4] N. Mo, Q. Tan, M. Bermingham, Y. Huang, H. Dieringa, N. Hort, M.X. Zhang, Current development of creep-resistant magnesium cast alloys: A review, Mater. Des. 155 (2018) 422-442.

[5] H. Yang, B. Jiang, G. Huang, Y. Huang, Y. Jin, S. Gavras, H. Dieringa, Revealing the role of Al in the microstructural evolution and creep properties of Mg-2.85Nd-0.92Gd-0.41Zr-0.29Zn alloy, Mater. Sci. Eng. A 832 (2022) 142358.

[6] Y. Bai, X. Yu, L. Wang, N. Zhang, B. Ye, W. Cheng, X. Kong, New HPDC Mg-RE based alloy with exceptional strength and creep resistance at elevated temperature, Mater. Sci. Eng. A 840 (2022) 142921.

[7] J. Yang, W. Wang, M. Zhang, J. Liu, S. Qin, The effects of continuous and discontinuous β-$Mg_{17}Al_{12}$ on compression creep properties of Mg-8.0Al-1.0Nd-1.0Gd alloys, Mater. Sci. Eng. A 858 (2022) 144191.

[8] D. Zhang, B. Li, J. Zhang, T. Niu, C. Li, P. Cheng, L. Yang, Influence of minor RE addition on microstructures, tensile properties, and creep resistance in a die-cast Mg-Al-Ca-Mn alloy, J. Mater. Res. Tech. 26 (2023) 3136-3145.

[9] B.H. Choi, B.S. You, W.W. Park, V.B. Huang, I.M. Park, Effect of Ca addition on the oxidation resistance of AZ91 magnesium alloys at elevated temperatures, Met. Mater. Int. 9 (2003) 395-398.

[10] A.K.S. Bankoti, A.K. Mondal, H. Dieringa, B.C. Ray, S. Kumar, Impression creep behaviour of squeeze-cast Ca and Sb added AZ91 magnesium alloy, Mater. Sci. Eng. A 673 (2016) 332-345.

[11] T. Chen, Q. Huo, S. Hu, C. Wang, Y. Zhang, Z. Zhang, S. Li, X. Yang, Tracing the effects of calcium, stannum, and zinc additions on the creep resistance of Mg-Al-based alloys, Metal. Mater. Trans. A 54 (2023) 2730-2743.

[12] S.S. Li, B. Tang, D.B. Zeng, Effects and mechanism of Ca on refinement of AZ91D alloy, J. Alloys Compd. 437 (2007) 317-321.

[13] S.W. Xu, K.O. Ishi, S. Kamado, F. Uchida, T. Homma, K. Hono, High-strength extruded Mg-Al-Ca-Mn alloy, Scr. Mater. 65 (2011) 269-272.

[14] M. Zubair, S. Sandlöbes, M.A. Wollenweber, C.F. Kusche, W. Hildebrandt, C. Broeckmann, S.K. Kerzel, On the role of Laves phases on the mechanical properties of Mg-Al-Ca alloys, Mater. Sci. Eng. A 756 (2019) 272-283.

[15] R. Ninomiya, T. Ojiro, K. Kubota, Improved heat resistance of Mg-Al alloys by the Ca addition, Acta Metal. Mater. 43 (1995) 669-674.

[16] A. Suzuki, N.D. Saddock, J.W. Jones, T.M. Pollock, Solidification paths and eutectic intermetallic phases in Mg-Al-Ca ternary alloys, Acta Mater. 53 (2005) 2823-2834.

[17] L. Zhang, K.K. Deng, K. Nie, F.J. Xu, K. Su, W. Liang, Microstructures and mechanical properties of Mg-Al-Ca alloys affected by Ca/Al ratio, Mater. Sci. Eng. A 636 (2015) 279-288.

[18] Y. Nakaura, A. Watanabe, K. Ohori, Effects of Ca, Sr additions on properties of Mg-Al based alloys, Mater. Trans. 47 (2006) 1031-1039.

[19] J. Bai, Y. Sun, F. Xue, S. Xue, J. Qiang, T. Zhu, Effect of Al contents on microstructures, tensile and creep properties of Mg-Al-Sr-Ca alloy, J. Alloys Compd. 437 (2007) 247-253.

[20] D. Itoh, Y. Terada, T. Sato, Effect of calcium additions on creep properties of a die-cast AM50 magnesium alloy, Mater. Trans. 49 (2008) 1957-1962.

[21] Y. Terada, D. Itoh, T. Sato, Creep rupture properties of die-cast Mg-Al-Ca alloys, Mater. Chem. Phys. 113 (2009) 503-506.

[22] T. Homma, S. Nakawaki, K.O. Ishi, K. Hono, S. Kamado, Unexpected influence of Mn addition on the creep properties of a cast Mg-2Al-2Ca (mass%) alloy, Acta Mater. 59 (2011) 7662-7672.

[23] G. Samimi, S. Mirdamadi, H. Razavi, M.A. Boutorabi, Improvement in impression creep property of as-cast AC515 Mg alloy by Mn addition, Mater. Sci. Eng. A 587 (2013) 213-220.

[24] S.M. Zhu, T.B. Abbott, M.A. Gibson, J.F. Nie, M.A. Easton, The influence of minor Mn additions on creep resistance of die-cast Mg-Al-RE alloys, Mater. Sci. Eng. A 682 (2017) 535-541.

[25] S. Lamm, D. Matschkal, M. Göken, P. Felfer, Impact of Mn on the precipitate structure and creep resistance of Ca containing magnesium alloys, Mater. Sci. Eng. A 761 (2019) 137964.

[26] M. Celikin, A.A. Kaya, M. Pekguleryuz, Effect of manganese on the creep behavior of magnesium and the role of α-Mn precipitation during creep, Mater. Sci. Eng. A 534 (2012) 129-141.

[27] H. Ferkel, B.L. Mordike, Magnesium strengthened by SiC nanoparticles, Mater. Sci. Eng. A 298 (2001) 193-199.

[28] H. Kumar, G.P. Chaudhari, Creep behavior of AS41 alloy matrix nanocomposites, Mater. Sci. Eng. A 607 (2014) 435-444,

[29] L. Katsarou, M. Mounib, W. Lefebvre, S. Vorozhtsov, M. Pavese, C. Badini, J.M. Molina-Aldareguia, C.C. Jimenez, M.T.P. Prado, H. Dieringa, Microstructure, mechanical properties and creep of magnesium alloy Elektron21 reinforced with AlN nanoparticles by ultrasound-assisted stirring, Mater. Sci. Eng. A 659 (2016) 84-92.

[30] S. Ganguly, A.K. Mondal, Influence of SiC nanoparticles addition on microstructure and creep behavior of squeeze-cast AZ91-Ca-Sb magnesium alloy, Mater. Sci. Eng. A 718 (2018) 377-389.

[31] H. Yang, Y. Huang, B. Song, K.U. Kainer, H. Dieringa, Enhancing the creep resistance of AlN/Al nanoparticles reinforced Mg-2.85Nd-0.92Gd-0.41Zr-0.29Zn alloy by a high shear dispersion technique, Mater. Sci. Eng. A 755 (2019) 18-27.

[32] H. Yang, D. Zander, Y. Huang, K.U. Kainer, H. Dieringa, Individual/synergistic effects of Al and AlN on the microstructural evolution and creep resistance of Elektron21 alloy, Mater. Sci. Eng. A 777 (2020) 139072.

[33] P. Zhou, S. Zhang, M. Li, H. Wang, W. Cheng, L. Wang, H. Li, W. Liang, Y. Liu, The creep behavior of Mg-9Al-1Si-1SiC composite at elevated temperature, J. Magnes. Alloy. 8 (2020) 944-951.

[34] S. Ganguly, S.T. Reddy, J. Majhi, P. Nasker, A.K. Mondal, Enhancing mechanical properties of squeeze-cast AZ91 magnesium alloy by combined additions of Sb and SiC nanoparticles, Mater. Sci. Eng. A 799 (2021) 140341.

[35] S. Sanyal, M. Paliwal, T.K. Bandyopadhyay, S. Mandal, Evolution of microstructure, phases and mechanical properties in lean as-cast Mg-Al-Ca-Mn alloys under the influence of a wide range of Ca/Al ratio, Mater. Sci. Eng. A 800 (2021) 140322.

[36] H. Dieringa, Properties of magnesium alloys reinforced with nanoparticles and carbon nanotubes: A review, J. Mater. Sci. 46 (2010) 289-306.

[37] Y. Li, T. Zhang, F. Wang, Unveiling the effect of Al-Mn intermetallic on the micro-galvanic corrosion of AM50 Mg alloy in NaCl solution, J. Mat. Res. Tech. 26 (2023) 753-763.
[38] E. Ghali, W. Dietzel, K.U. Kainer, General and localized corrosion of magnesium alloys: A critical review, J. Mat. Eng. Perf. 13 (2004) 7-23.
[39] M.E. Turan, Y. Sun, F. Aydin, H. Zengin, Y. Turen, H. Ahlatci, Effects of carbonaceous reinforcements on microstructure and corrosion properties of magnesium matrix composites, Mat. Chem. Phy. 218 (2018) 182-188.
[40] C. Zhang, T. Zhang, Y. Wang, F. Wei, Y. Shao, G. Meng, F. Wang, K. Wu, Effect of SiC particulates on the corrosion behavior of extruded AZ91/SiC_p composites during the early stage of exposure, J. Elec. Soc. 162 (2015) C754.
[41] A.K. Mondal, C. Blawert, S. Kumar, Corrosion behaviour of creep-resistant AE42 magnesium alloy-based hybrid composites developed for powertrain applications, Mater. Corros. 66 (2015) 1150-1158.
[42] M. Kukreja, R. Balasubramaniam, Q.B. Nguyen, M. Gupta, Enhancing corrosion resistance of Mg alloy AZ31B in NaCl solution using alumina reinforcement at nanolength scale, Corros. Eng. Sci. Technol. 44 (2009) 381-384.
[43] M. Shahin, K. Munir, C. Wen, Y. Li, Magnesium matrix nanocomposites for orthopedic applications: A review from mechanical, corrosion, and biological perspectives, Acta Biomater. 96 (2019) 1-19.
[44] S. Ganguly, A.K. Mondal, S. Sarkar, A. Basu, S. Kumar, C. Blawert, Improved corrosion response of squeeze-cast SiC nanoparticles reinforced AZ91-2.0Ca-0.3Sb alloy, Corros. Sci. 166 (2020) 108444.
[45] O. Esmaeilzadeh, A.R. Eivani, M. Mehdizade, S.M.A. Boutorabi, S.M. Masoudpanah, An investigation of microstructural background for improved corrosion resistance of WE43 magnesium-based composites with ZnO and Cu/ZnO additions, J. Alloys Compd. 908 (2022) 164437.
[46] K.H. Kim, N.D. Nam, J.G. Kim, K.S. Shin, H.C. Jung, Effect of calcium addition on the corrosion behavior of Mg–5Al alloy, Intermetallics 19 (2011) 1831-1838.
[47] B. Wang, M. Li, Y. Li, Y. Wang, Y. Gao, H. Wang, Effect of Al/Mn ratio on corrosion behavior of lean Mg-Zn-Ca-Al-Mn alloy processed by twin-roll casting, Corros. Sci. 212 (2023) 110938.
[48] M. Haghshenas, M. Gupta, Magnesium nanocomposites: An overview on time-dependent plastic (creep) deformation, Defence Technol. 15 (2019) 123-131.

[49] J.F. Nie, Precipitation and hardening in magnesium alloys, Metal. Mater. Trans. A 43 (2012) 3891-3939.

[50] M.M. Avedesian, H. Baker (Eds) ASM Specialty Handbook - Magnesium and Magnesium Alloys, Materials Park, OH: ASM International (1999).

[51] C.D. Yim, B.S. You, R.S. Jang, S.G. Lim, Effects of melt temperature and mold preheating temperature on the fluidity of Ca containing AZ31 alloys. J. Mater. Sci. 41 (2006) 347-2350.

[52] L. Han, H. Hu, D.O. Northwood, N. Li, Microstructure and nanoscale mechanical behavior of Mg-Al and Mg-Al-Ca alloys, Mater. Sci. Eng. A 473 (2008) 16-27.

[53] S.M. Liang, R.S. Chen, J.J. Blandin, M. Suery, E.H. Han, Thermal analysis and solidification pathways of Mg–Al–Ca system alloys, Mater. Sci. Eng. A 480 (2008) 365-372.

[54] A. Suzuki, N.D. Saddock, J.W. Jones, T.M. Pollock, Structure and transition of eutectic $(Mg,Al)_2Ca$ laves phase in a die-cast Mg-Al-Ca base alloy, Scr. Mater. 51 (2004) 1005-1010.

[55] J. You, C. Wang, S.L. Shang, Y. Gao, H. Ju, H. Ning, Y. Wang, H.Y. Wang, Z. Liu, Ordering in liquid and its heredity impact on phase transformation of Mg-Al-Ca alloys, J. Magnes. Alloy. 11 (2023) 2006-2017.

[56] Z.T. Li, X.D. Zhang, M.Y. Zheng, X.G. Qiao, K. Wu, C. Xu, S. Kamado, Effect of Ca/Al ratio on microstructure and mechanical properties of Mg-Al-Ca-Mn alloys, Mater. Sci. Eng. A 682 (2017) 423-432.

[57] M. Zubair, S.S. Haut, R. Pei, M.A. Wollenweber, L. Berners, C.F. Kusche, C. Liu, F. Roters, J.S.K.L. Gibson, S.K. Kerzel, Strengthening of Mg-Al-Ca alloys with C15 and C36 Laves phases. J. Mater. Res. 38 (2023) 3613-3627.

[58] M. Zubair, M. Felten, B. Hallstedt, M.V. Paredes, L. Abdellaoui, R.B. Villoro, M.L. Chwalek, N. Ayeb, H. Springer, J. Mayer, B. Berkels, D. Zander, S.K. Kerzel, C. Scheu, S. Zhang, Laves phases in Mg-Al-Ca alloys and their effect on mechanical properties, Mater. Des. 225 (2023) 111470.

[59] Z.T. Li, X. G. Qiao, C. Xu, S. Kamado, M.Y. Zheng, A.A. Luo, Ultrahigh strength Mg-Al-Ca-Mn extrusion alloys with various aluminum contents, J. Alloys Compd. 792 (2019) 130-141.

[60] A. Suzuki, N. Saddock, J. Terbush, B.R. Powell, J.W. Jones, T.M. Pollock, Precipitation strengthening of a Mg-Al-Ca-based AXJ530 die-cast alloy. Metal. Mater. Trans. A 39 (2008) 696-702.

[61] S. Kashiwase, M. Unekawa, H. Hisazawa, Y. Terada, Three-dimensional morphology of C15-Al_2Ca precipitates in a Mg–Al–Ca Alloy, Mater. Trans. 60 (2019) 2048-2052.

[62] J. Zuo, T. Nakata, C. Xu, Y.P. Xia, H.L. Shi, G.S. Wang, G.Z. Tang, G.H. Fan, S. Kamado, L. Geng, Effect of annealing on microstructure evolution and age-hardening behavior of dilute Mg-Al-Ca-Mn alloy, J. Mater. Res. Tech. 18 (2022) 1754-1762.

[63] R.E.R. Hill, R. Abbaschian, Physical Metallurgy Principles, 3rd Edition, PWS Publishing Company, Boston, 1994.

[64] G.E. Dieter, Mechanical Metallurgy. McGraw-Hill Companies, Inc., New York, 1986.

[65] A.K. Mukherjee, J.E. Bird, J.E. Dorn, Experimental correlations for high-temperature creep, Trans. ASM 62 (1965) 155-179.

[66] D.H. Sastry, Impression creep technique-An overview, Mater. Sci. Eng. A 409 (2005) 67-75.

[67] S. Ganguly, A.K. Chaubey, R. Sahoo, A. Kushwaha, A. Basu, J. Majhi, M. Gupta, Influence of ultrasonic shot peening on the microstructure and impression creep performance of squeeze-cast AZ91 alloy reinforced with graphene nanoplatelets, J. Alloys Compd. 938 (2023) 168640.

[68] S.F. Hassan, M. Gupta, Enhancing physical and mechanical properties of Mg using nanosized Al_2O_3 particulates as reinforcement, Metal. Mater. Trans. A 36 (2005) 2253-2258.

[69] S.F. Hassan, M. Gupta, Effect of different types of nanosize oxide participates on microstructural and mechanical properties of elemental Mg, J. Mater. Sci. 41 (2006) 2229-2236.

[70] S.F. Hassan, M. Gupta, Effect of particulate size of Al_2O_3 reinforcement on microstructure and mechanical behavior of solidification processed elemental Mg, J. Alloys Compd. 419 (2006) 84-90.

[71] C.S. Goh, J. Wei, L.C. Lee, M. Gupta, Properties and deformation behaviour of Mg-Y_2O_3 nanocomposites, Acta Mater. 55 (2007) 5115-5121.

[72] Q.B. Nguyen, M. Gupta, Enhancing compressive response of AZ31B magnesium alloy using alumina nanoparticulates, Compos. Sci. Technol. 68 (2008) 2185-2192.

[73] W.Z. Hui, W.X. Dong, Z.Y. Xin, D.U.W. Bo, SiC nanoparticles reinforced magnesium matrix composites fabricated by ultrasonic method, Trans. Nonferrous Met. Soc. China 20 (2010) s1029-s1032.

[74] M. Paramsothy, J. Chan, R. Kwok, M. Gupta, The synergistic ability of Al_2O_3 nanoparticles to enhance mechanical response of hybrid alloy AZ31/AZ91, J. Alloys Compd. 509 (2011) 7572-7578.

[75] S. Sankaranarayanan, S. Jayalakshmi, M. Gupta, Effect of individual and combined addition of micro/nano-sized metallic elements on the microstructure and mechanical properties of pure Mg, Mater. Des. 37 (2012) 274-284.

[76] S. Sankaranarayanan, U.P. Nayak, R.K. Sabat, S. Suwas, A. Almajid, M. Gupta, Nano-ZnO particle addition to monolithic magnesium for enhanced tensile and compressive response, J. Alloys Compd. 615 (2014) 211-219.

[77] H.K. Khosroshahi, F.F. Saniee, H.R. Abedi, Mechanical properties improvement of cast AZ80 Mg alloy/nano-particles composite via thermomechanical processing; Mater. Sci. Eng. A 595 (2014) 284-290.

[78] G.K. Meenashisundaram, M.H. Nai, A. Almajid, M. Gupta, Development of high performance Mg-TiO_2 nanocomposites targeting for biomedical/structural applications, Mater. Des. 65 (2015) 104-114.

[79] Y. Chen, S. Tekumalla, Y.B. Guo, R. Shabadi, V.P.W. Shim, M. Gupta, The dynamic compressive response of a high-strength magnesium alloy and its nanocomposite, Mater. Sci. Eng. A 702 (2017) 65-72.

[80] G. Parande, V. Manakari, S. Wakeel, M.S. Kujur, M. Gupta, Enhancing mechanical response of monolithic magnesium using nano-NiTi (Nitinol) particles, Met. 8 (2018) 1014.

[81] S. Ganguly, S. Sarkar, A.K. Mondal, Enhancement of tensile properties of AZ91-Ca-Sb Magnesium alloy with SiC nanoparticles additions, Met. Mater. Int. 27 (2021) 3796-3809.

[82] Y.H. Chen, X.Y. Gao, K.B. Nie, Y.N. Li, K.K. Deng, Different effects of SiC dimensions on the microstructure and mechanical properties of magnesium matrix composites, Mater. Sci. Eng. A 847 (2022) 143273.

[83] M.G. Fontana, Corrosion Engineering, 3rd Edition, 1987, McGrow-Hill Book Company, New York.

[84] G.L. Song, A. Atrens, Corrosion mechanisms of magnesium alloys, Adv. Eng. Mater. 1 (1999) 1.

[85] S. Tiwari, R. Balasubramaniam, M. Gupta, Corrosion behavior of SiC reinforced magnesium composites, Corros. Sci. 49 (2007) 711-725.

[86] K. Ozturk, Y. Zhong, Z.K. Liu, A.A. Luo, Creep resistant Mg-Al-Ca alloys: Computational thermodynamics and experimental investigation, JOM 55 (2003) 40-44.

[87] M.P. Liu, Q.D. Wang, X.Q. Zeng, G.Y. Yuan, Y.P. Zhu, W.J. Ding, Mechanical properties and creep behavior of Mg-Al-Ca alloys, Mater. Sci. Forum 488-489 (2005) 763-766.

[88] L. Han, D.O. Northwood, X. Nie, H. Hu, The effect of cooling rates on the refinement of microstructure and the nanoscale indentation creep behavior of Mg-Al-Ca alloy, Mater. Sci. Eng. A 512 (2009) 58-66.

[89] T. Homma, S. Nakawaki, S. Kamado, Improvement in creep property of a cast Mg-6Al-3Ca alloy by Mn addition, Scr. Mater. 63 (2010) 1173-1176.

[90] L.Y. Chen, J.Q. Xu, H. Choi, H. Konishi, S. Jin, X.C. Li, Rapid control of phase growth by nanoparticles, Nat. Comm. 5 (2014) 3879.

[91] K. Wang, H.Y. Jiang, Y.W. Jia, H. Zhou, Q.D. Wang, B. Ye, W.J. Ding, Nanoparticle-inhibited growth of primary aluminum in Al-10Si alloys, Acta Mater. 103 (2016) 252-263.

[92] J.C. Slater, Atomic radii in crystals, J. Chem. Phys. 41 (1964) 3199-3204.

[93] S.J. Huang, M. Subramani, C.C. Chiang, Effect of hybrid reinforcement on microstructure and mechanical properties of AZ61 magnesium alloy processed by stir casting method, Compos. Comm. 25 (2021) 100772.

[94] S.K. Moheimani, M. Dadkhah, M.H. Mosallanejad, A. Saboori, Fabrication and characterization of the modified EV31-based metal matrix nanocomposites, Met. 11 (2021) 125.

[95] J.Q. Xu, L.Y. Chen, H. Choi, X.C. Li, Theoretical study and pathways for nanoparticle capture during solidification of metal melt, J. Phys. Condens. Matter 24 (2012) 255304.

[96] E. Guo, S. Shuai, D. Kazantsev, S. Karagadde, A.B. Phillion, T. Jing, W. Li, P.D. Lee, The influence of nanoparticles on dendritic grain growth in Mg alloys, Acta Mater. 152 (2018) 127-137.

[97] A.A. Luo, M.P. Balogh, B.R. Powell, Tensile creep and microstructure of magnesium-aluminum-calcium based alloys for powertrain applications - Part 2 of 2, SAE Trans. 110 (2001) 414-422.

[98] J.H. Hollomon, Tensile deformation, Trans. AIME 162 (1945) 268-290.

[99] L.H. Dai, Z. Ling, Y.L. Bai, Size-dependent inelastic behavior of particle-reinforced metal-matrix composites, Compos. Sci. Technol. 61 (2001) 1057-1063.

[100] M.H. Korayem, R. Mahmudi, W.J. Poole, Enhanced properties of Mg-based nanocomposites reinforced with Al_2O_3 nanoparticles, Mater. Sci. Eng. A 519 (2009) 198-203.

[101] S.C. Tjong, Novel nanoparticle-reinforced metal matrix composites with enhanced mechanical properties, Adv. Eng. Mater. 9 (2007) 639-652.

[102] T.J. Lee, W.J. Kim, Microstructure and tensile properties of magnesium nanocomposites fabricated using magnesium chips and carbon black, J. Magnes. Alloy. 8 (2020) 860-872.

[103] M. Manoharan, S.C. Lim, M. Gupta, Application of a model for the work hardening behavior to Mg/SiC composites synthesized using a fluxless casting process, Mater. Sci. Eng. A 333 (2002) 243-249.

[104] M.H. Korayem, R. Mahmudi, W.J. Poole, Work hardening behavior of Mg-based nanocomposites strengthened by Al_2O_3 nanoparticles, Mater. Sci. Eng. A 567 (2013) 89-94.

[105] A.S. Zadeh, Comparison between current models for the strength of particulate-reinforced metal matrix nanocomposites with emphasis on consideration of Hall-Petch effect, Mater. Sci. Eng. A 531 (2012) 112-118.

[106] Z. Zhang, D.L. Chen, Consideration of Orowan strengthening effect in particulate-reinforced metal matrix nanocomposites: A model for predicting their yield strength, Scr. Mater. 54 (2006) 1321-1326.

[107] Z. Zhang, D.L. Chen, Contribution of Orowan strengthening effect in particulate-reinforced metal matrix nanocomposites, Mater. Sci. Eng. A 483-484 (2008) 148-152.

[108] C. Mallmann, F. Hannard, E. Ferrié, A. Simar, R. Daudin, P. Lhuissier, A. Pacureanu, M. Fivel, Unveiling the impact of the effective particles distribution on strengthening mechanisms: A multiscale characterization of $Mg+Y_2O_3$ nanocomposites, Mater. Sci. Eng. A 764 (2019) 138170.

[109] A. Khandelwal, K. Mani, N. Srivastava, R. Gupta, G.P. Chaudhari, Mechanical behavior of AZ31/Al_2O_3 magnesium alloy nanocomposites prepared using ultrasound assisted stir casting, Compos. Part B 123 (2017) 64-73.

[110] C.S. Goh, M. Gupta, J. Wei, L.C. Lee, Characterization of high performance Mg/MgO nanocomposites, J. Compos. Mater. 41 (2007) 2325-2335.

[111] R. Tandon, K.K. Mehta, R. Manna, R.K. Mandal, Effect of tensile straining on the precipitation and dislocation behavior of AA7075T7352 aluminum alloy, J. Alloys Compd. 904 (2022) 163942.

[112] R.M. Wang, A. Eliezer, E. Gutman, Microstructures and dislocations in the stressed AZ91D magnesium alloys, Mater. Sci. Eng. A 344 (2003) 279-287.

[113] R.M. Wang, A. Eliezer, E.M. Gutman, An investigation on the microstructure of an AM50 magnesium alloy, Mater. Sci. Eng. A 355 (2003) 201-207.

[114] M.R. Barnett, Twinning and the ductility of magnesium alloys. Part II. 'Contraction' twins, Mater. Sci. Eng. A 464 (2007) 8-16.

[115] J. Thornby, D. Verma, R. Cochrane, A. Westwood, V.B. Manakari, M. Gupta, M. Haghshenas, Indentation-based characterization of creep and hardness behavior of magnesium carbon nanotube nanocomposites at room temperature, SN Appl. Sci. 1 (2019) 695.

[116] S. Rashno, B. Nami, S.M. Miresmaeili, Impression creep behavior of a cast MRI153 magnesium alloy, Mater. Des. 60 (2014) 289-294.

[117] H. Somekawa, K. Hirai, H. Watanabe, Y. Takigawa, K. Higashi, Dislocation creep behavior in Mg-Al-Zn alloys, Mater. Sci. Eng. A 407 (2005) 53-61.

[118] S. Suwas, R.K. Ray, Crystallographic Texture of Materials, 1st Edition, Springer, London, 2014.

[119] A.C. Fischer-Cripps, Introduction to Contact Mechanics, 2nd Edition, Springer, New York, 2000.

[120] D. Sun, M. Ponga, K. Bhattacharya, M. Ortiz, Proliferation of twinning in hexagonal close-packed metals: Application to magnesium, J. Mechanics Phys. Solids 112 (2018) 368-384.

[121] J.W. Edington, Interpretation of Transmission Electron Micrographs, Red Globe Press London, N.V. Edition 1, 1975.

[122] Z. Wu, W. Curtin, The origins of high hardening and low ductility in magnesium, Nat. 526 (2015) 62-67.

[123] Y. Liu, J. Yan, D. Xie, Y. Shen, J. Wang, G. Zhu, Self-patterning screw <c> dislocations in pure Mg, Scr. Mater. 191 (2021) 86-89.

[124] F. Cao, Z. Shi, J. Hofstetter, P.J. Uggowitzer, G. Song, M. Liu, A. Atrens, Corrosion of ultra-high-purity Mg in 3.5% NaCl solution saturated with $Mg(OH)_2$, Corros. Sci. 75 (2013) 78-99.

[125] J. Majhi, S. Ganguly, A. Basu, A.K. Mondal, Improved corrosion response of squeeze-cast AZ91 magnesium alloy with calcium and bismuth additions, J. Alloys compd. 873 (2021) 159600.

[126] S. Ganguly, A.K. Chaubey, R. Gope, A. Kushwaha, A. Basu, M. Gupta, Enhanced corrosion performance of ultrasonically shot peened and graphene nanoparticles reinforced squeeze-cast AZ91 magnesium alloy, J. Alloys compd. 966 (2023) 171203.

[127] K. Zhang, C. Wang, S. Liu, K. Guan, M.X. Li, L.Y. Zhang, H.Y. Wang, New insights on corrosion behavior of aging precipitates in dilute Mg-Al-Ca alloy by experiments and first-principles calculations, Corros. Sci. 220 (2023) 111254.

[128] A.D. King, N. Birbilis, J.R. Scully, Accurate electrochemical measurement of magnesium corrosion rates, a combined impedance, mass-loss and hydrogen collection study, Elect. Acta. 121 (2014) 394–406.

[129] S. Yin, W. Duan, W. Liu, L. Wu, J. Bao, J. Yu, L. Li, Z. Zhao, J. Cui, Z. Zhang, Improving the corrosion resistance of MgZn1.2GdxZr0.18 (x = 0, 0.8, 1.4, 2.0) alloys via Gd additions, Corros. Sci. 177 (2020) 108962.

[130] J.S. Li, M.X. Li, Z.M. Hua, Y.T. Mo, K. Guan, M. Zha, Y. Gao, H.Y. Wang, A corrosion-resistant and age-hardenable Mg-Al-Mn-Ca-Ce dilute alloy with fine-grained structure processed by controlled rolling, J. Mater. Sci. Technol. 163 (2023) 223-236.

[131] K. Zhang, J. Lu, J. Li, D. Zhang, L. Gao, H. Zhou, An improved approach to prepare triazole protective film by click-assembly on copper surface, Corros. Sci. 164 (2020) 108352.

[132] X. Liu, J. Xue, S. Liu, Discharge and corrosion behaviors of the α-Mg and β-Li based Mg alloys for Mg-air batteries at different current densities, Mater. Des. 160 (2018) 138-146,

[133] V. Beura, D. Zhang, N. Overman, J. Darsell, D.R. Herling, K. Solanki, V.V. Joshi, Enhanced mechanical behavior and corrosion resistance of AZ31 magnesium alloy through a novel solid-phase processing, Corros. Sci. 197 (2022) 110074.

[134] P. Metalnikov, G.B. Hamu, K.S. Shin, A. Eliezer, Effect of Ca addition on corrosion behavior of wrought AM60 magnesium alloy in alkaline solutions, Met. 11 (2021) 1172.

[135] S.M Baek, H.J. Kim, H.Y. Jeong, S. Sohn, H. Shin, K. Choi, K. Lee, J.G. Lee, C.D. Yim, B.S. You, H. Ha, S.S. Park, Effect of alloyed Ca on the microstructure and corrosion properties of extruded AZ61 Mg alloy, Corros. Sci. 112 (2016) 44-53.

[136] Y.X. Zhu, G.L. Song, P.P. Wu, Self-repairing functionality and corrosion resistance of in-situ Mg-Al LDH film on Al-alloyed AZ31 surface, J. Magnes. Alloy. 11 (2023) 1567-1579.

[137] K. Hoshino, S. Furuya, R.G. Buchheit, Effect of solution pH on layered double hydroxide formation on electrogalvanized steel sheets. J. Mater. Eng. Perf. 28 (2019) 2237-2244.

[138] W. Wu, F. Zhang, Y. Li, L. Song, D. Jiang, R. Zeng, S.C. Tjong, D. Chen, Corrosion resistance of dodecanethiol-modified magnesium hydroxide coating on AZ31 magnesium alloy, Appl. Phys. A 126 (2020) 8.

[139] G. Zhang, L. Wu, A. Tang, X. Chen, Y. Ma, Y. Long, P. Peng, X. Ding, H. Pan, F. Pan, Growth behavior of Mg Al-layered double hydroxide films by conversion of anodic films on magnesium alloy AZ31 and their corrosion protection, Appl. Surf. Sci. 456 (2018) 419-429.

[140] Z. Feng, L. Ren, J. Zhang, P. Yang, M. An, Effect of additives on the corrosion mechanism of nanocrystalline zinc-nickel alloys in an alkaline bath, RSC Adv. 6 (2016) 88469.

[141] M.S. Navid, Y. Cao, J.E. Svensson, A. Allanore, N. Birbilis, L.G. Johansson, M. Esmaily, On the early stages of localised atmospheric corrosion of magnesium-aluminium alloys, Sci. Rep. 10 (2020) 20972.

[142] M.P. Liu, Q.D. Wang, X.Q. Zeng, Y.H. Wei, Y.P. Zhu, C. Lu, Development of microstructure in solution-heat-treated Mg-5Al-xCa alloys, Z. Metallkde. 94 (2003) 886-891.

[143] S. Inoue, K. Ishiage, Y. Kawamura, Optimization of heat treatment condition of nonflammable Mg-Al-Ca alloys with high thermal conductivity, J. Alloys Compd. 934 (2023) 168014.

[144] M.K. Surappa, Microstructure evolution during solidification of DRMMCs (discontinuously reinforced metal matrix composites): State of Art," J. Mater. Process. Technol. 63 (1997) 325–333.

[145] A. Takeuchi, A. Inoue, Classification of bulk metallic glasses by atomic size difference, heat of mixing and period of constituent elements and its application to characterization of the main alloying element, Mater. Trans. 46 (2005) 2817-2829.

[146] T. Nakata, C. Xu, R. Ajima, K. Shimizu, S. Hanaki, T.T. Sasaki, L. Ma, K. Hono, S. Kamado, Strong and ductile age-hardening Mg-Al-Ca-Mn alloy that can be extruded as fast as aluminum alloys, Acta Mater. 130 (2017) 261-270.

[147] M.Z. Bian, T.T. Sasaki, B.C. Suh, T. Nakata, S. Kamado, K. Hono, A heat-treatable Mg-Al-Ca-Mn-Zn sheet alloy with good room temperature formability, Scr. Mater. 138 (2017) 151-155.

[148] Y. Terada, N. Ishimatsu, T Sato, Creep Parameters in a Die-Cast Mg-Al-Ca Alloy, Mater. Trans. 48 (2007) 2329-2335.

[149] B. Kondori, R. Mahmudi, Effect of Ca additions on the microstructure and creep properties of a cast Mg-Al-Mn magnesium alloy, Mater. Sci. Eng. A 700 (2017) 438-447.

[150] A.A. Luo, B.R. Powell, M.P. Balogh, Creep and microstructure of magnesium-aluminum-calcium based alloys, Metal. Mater. Trans. A 33 (2002) 567-574.

[151] B. Jing, S. Yangshan, X. Shan, X. Feng, Z. Tianbai, Microstructure and tensile creep behavior of Mg-4Al based magnesium alloys with alkaline-earth elements Sr and Ca additions, Mat. Sci. Eng. A 419 (2006) 181-188.

[152] Z. Liu, R. Xin, X. Huang, Twin variant selection criteria in magnesium alloy: a review, J. Mater. Sci. 59 (2024)1 0058-10077.

[153] M. Lentz, M. Risse, N. Schaefer, W. Reimers, I.J. Beyerlein, Strength and ductility with {10T1}-{10T2} double twinning in a magnesium alloy, Nat. Comm. 7 (2016) 11068.

[154] X. Wang, P. Mao, Z. Liu, Z. Wang, F. Wang, L. Zhou, Z. Wei, Nucleation and growth analysis of {10T2} extension twins in AZ31 magnesium alloy during in-situ tension, J. Alloys Compd. 817 (2020) 152967.

[155] D.F. Shi, C.Y. Wang, C.M.C. Jiménez, M.T.P. Prado, Atomic scale interactions of basal dislocations and twin boundaries with ultrathin precipitates in magnesium alloys, Acta Mater. 221 (2021) 117442.
[156] B. Anthony, B. Leu, I.J. Beyerlein, V.M. Miller, Deformation twin interactions with grain boundary particles in multi-phase magnesium alloys, Acta Mater. 219 (2021) 117225.
[157] B. Leu, M.A. Kumar, K. Xie, I.J. Beyerlein, Investigation of twin growth mechanisms in precipitate hardened AZ91, Acta Mater. 242 (2023) 118471.
[158] F. Liu, H. Cui, C. Liu, X. Song, Z. Cui, R. Xin, Understanding the interaction of {10-12} twins and $Mg_{17}Al_{12}$ precipitates in magnesium alloys via high-resolution electron microscopy, J. Mater. Res. Technol. 27 (2023) 7129-7137.
[159] L.M. Wang, C.C. Chen, Twin growth and its interaction with precipitates, Mater. Lett. 67 (2012) 158-161.
[160] P. Yi, R.C. Cammarata, M.L. Falk, Atomistic simulation of solid solution hardening in Mg/Al alloys: Examination of composition scaling and thermo-mechanical relationships, Acta Mater. 105 (2016) 378-389.

Dissemination

Publications in the peer-reviewed international journals from the present thesis

1. **P. Nasker**, A.K. Mondal, SiC nanoparticles additions to squeeze-cast Mg-5.0 Al-2.0 Ca-0.3 Mn alloy: An evaluation of microstructure and mechanical properties, *Materials Characterization* 212 (2024) 113984.
2. **P. Nasker**, A.K. Mondal, Microstructure evolution and assessment of creep behaviour of SiC nanoparticles dispersed squeeze-cast Mg-5.0Al-2.0Ca-0.3Mn alloy, *Materials Science and Engineering A* 910 (2024) 146894.
3. **P. Nasker,** S. Kumar, and A.K. Mondal, On the correlation of microstructure and superior corrosion behaviour of squeeze-cast SiC nanoparticle-dispersed Mg-Al-Ca-Mn alloy, *Journal of Alloys and Compounds 1039 (2025) 183121.*
4. **P. Nasker**, A. K. Mondal, J. Basua, H. Dieringa, and S. Kumar, On the correlation of creep behavior and microstructures of age-hardened noble Mg-Al-Ca-Mn + SiC_{np} nanocomposites, *Composites Part A: Applied Science and Manufacturing, Under review*.

Conference attended based on the present work

1. **P. Nasker**, S. Katiyar, A. Gourav, S.S. Shukla, A.K. Mondal, Effect of heat treatment on microstructure and creep behaviour of Mg-Al-Ca-Sr alloy, Advance Materials Conference 2022, 23-24 February 2022, CSIR-NIST, Trivandrum, India.
2. **P. Nasker**, A.K. Mondal, Microstructure and creep behaviour of as-cast and heat-treated Mg-Al-Ca alloy, NMD-ATM 2023, 22-24 November 2023, KIT Bhubaneswar, India.
3. **P. Nasker,** J. Basu, and A.K. Mondal, Dislocation and Twin Characteristics in Creep Tested Heat-treated SiC Dispersed AXM520 nanocomposites, EMSI-2025, 12-14 July 2025, IISc Bangalore, India.